Design of Cost-Optimized Village-Scale Electrodialysis Systems for Brackish Water Desalination

by

Natasha C. Wright

B.S., University of St. Thomas (2012)
S.M., Massachusetts Institute of Technology (2014)

Submitted to the Department of Mechanical Engineering
in partial fulfillment of the requirements for the degree of

Doctor of Philosophy in Mechanical Engineering

at the

MASSACHUSETTS INSTITUTE OF TECHNOLOGY

June 2018

Author ..... Signature redacted
Department of Mechanical Engineering
May 18, 2018

Certified by ..... Signature redacted
Amos G. Winter, V
Associate Professor of Mechanical Engineering
Thesis Supervisor

Accepted by ..... Signature redacted
Rohan Abeyaratne
Professor of Mechanical Engineering
Graduate Officer

Design of Cost-Optimized Village-Scale Electrodialysis Systems for Brackish Water Desalination

by

Natasha C. Wright

Submitted to the Department of Mechanical Engineering
on May 18, 2018, in partial fulfillment of the
requirements for the degree of
Doctor of Philosophy in Mechanical Engineering

Abstract

This thesis proposes methods of reducing the cost of electrodialysis brackish water desalination systems, specifically for use in rural India, where 60% of the groundwater is too saline to drink. Convergence of socioeconomic and technical factors led to the insight that photovoltaic (PV) powered electrodialysis (ED) has the potential for impact in rural water treatment. In order to design a system that can meet the necessary production requirements, a robust parametric model was created to predict the desalination rate, limiting current density, and total energy use in an ED system. The model agrees with experimental measurements across two diverse ED stack designs, differing in total membrane area, membrane manufacturers, and flow channel spacers. A commercial-scale ED stack was additionally tested in Chelluru, India, building confidence that the model is predictive for real groundwater, and that ED systems are feasible to operate in the rural Indian context.

The ED model was used within an optimization routine to determine the lowest cost operating mode and stack design, assuming existing, flat-stack architectures. Common operating modes including constant-voltage batch and multi-stage continuous systems were considered alongside novel operation modes including voltage-regulated batch and hybrid batch-continuous systems. For the production and desalination rates required for a village-scale application, a voltage-regulated hybrid system that is fully optimized for membrane width, length, and channel thickness reduces the 10-year total cost and capital cost of the system by 37% and 47%, respectively, in comparison to a commercially available stack optimized under the same operation modes.

While matching of applied and limiting current densities can be achieved using a voltage-regulated batch operation (minimizing stack cost), this requires a potentially costly DC power supply and control system. The final part of the thesis proposes a spiral ED stack architecture that allows for matching through the geometry of the stack alone. Both a standard Archimedean spiral and an ideal irregular spiral shape are presented. The ideal spiral shape would reduce the 10-year total cost and capital cost by 21% and 39%, respectively, in comparison to the Archimedean spiral, and is cost-competitive with a hybrid voltage-regulated flat-stack design.

Thesis Supervisor: Amos G. Winter, V
Title: Associate Professor of Mechanical Engineering

Acknowledgments

I would like to thank the following people and organizations for their contributions to my work:

- My family, immediate and extended, for their continuous support and encouragement.
- Amos, for his guidance and feedback on my work and life in general, as well as his constant enthusiasm for research and design with impact in developing economies.
- My friends, especially Dan, for helping me to maintain balance in my life.
- My labmates in the Global Engineering and Research (GEAR) Lab, for their fun-loving spirit and for making our working and learning environment a positive one. Particularly to David Bian, Sterling Watson, Sahil Shah, Wei He, Anne-Claire Lenaff, and Dev Ramanujan who collectively make up Team Desal (and the best global travel buddies one could ask for). And to Susan Amrose, Marius Peters, Elizabeth Brownell, and Jeff Costello for the their guidance and assistance in moving this research forward.
- Georgia, Cathy, Fiona, Moti, Rosa, Hannah, Matt, and Sandra, my undergraduate research assistants, for their commitment to the project, inquisitive nature, creativity, and independent work ethic.
- Mr. Tenny Cherian, Mr. Anil Kumar, Mr. Sree Rama Murthy, and their team at Tata Projects, for their unsurpassed support during field work, vision for the potential impact of desalination in India, and hospitality during my field work in Hyderabad, India.
- Dr. Jarah Meador and everyone involved in the USAID Desal Prize, for forcing me to question my assumptions early and providing the opportunity to interact and brainstorm with experts in field, both on other teams and within the group of judges and organizers.
- Dr. Gregor von Medeazza (UNICEF, Jerusalem) and his partners for their support and vision for safe water access in Israel and Gaza.
- Mr. R.B. Jain, Mr. Abhijit Joshi and Mr. Abhishek Nirakhe, of Jain Irrigation Systems, Ltd., for the opportunity to work on this project and their hospitality during my field work in Jalgaon, India.

- Drs. Rob Stoner, Chintan Vaishnav, and Nevan Hanumara from the Tata Center at MIT, for their feedback on my work and efforts to bring valuable speakers to the Fellows at the Tata Center.

- Drs. Amy Bilton, Ronan McGovern, and Karim Chehayeb for their willingness to answer my questions and for demonstrating impactful PhD theses in the area of desalination.

- Jamie Vinsant of Suez Water Technologies, for providing invaluable guidance from the real-world of electrodialysis (ED), specifically on the design limitations and freedoms surrounding the manufacturing of ED stacks.

- And last but certainly not least, all of the people I have met during my field research in India and Israel. Thank you for taking the time to help me understand and for all the meals we shared together.

I am also grateful to the following sources who have provided financial support for this work:

Tata Projects
USAID and Securing Water for Food: A Grand Challenge for Development
UNICEF
Tata Center for Technology and Design at MIT
Jain Irrigation Systems, Ltd.
MIT Undergraduate Research Opportunities Program
National Science Foundation Graduate Research Fellowship Program

Contents

Chapter 1

Introduction

This thesis proposes methods of reducing the cost of small-scale electrodialysis (ED) brackish water desalination systems, specifically for use in rural India. The chapters move from the development of a robust analytical model of ED, to the implementation of an optimization routine to determine the most cost-effective scheme of implementing ED within the current flat-stack configuration, to the design of novel spiral architectures. The socioeconomic and technical analysis that drove the requirement for desalination in the rural Indian context and the reasons that ED was chosen as the desalination technology to investigate is summarized here.

1.1 The Need for Brackish Water Desalination in Rural India

India has nearly 600,000 villages that collectively house 800 million people [1]. This rural population accounts for approximately 75% of India's total population. In 2010 the WHO UNICEF Joint Programme for Water Supply and Sanitation (JMP)

reported that 15% of the rural population was without access to an improved water source [2]. The JMP defines an improved water source as a household connection, public standpipe, borehole, protected dug well, protected spring or rainwater, where as an unimproved source would include an unprotected spring, unprotected dug well, tanker-truck, surface water, or bottled water. Even if a source is listed as "improved" it may still be contaminated [2]. There are three primary categories of water contaminants: biological, chemical, and physical. Proper selection of a water purification technology depends on the contaminants present in the feed water source.

1.1.1 Most Existing Purification Technologies Target Biological Contaminants

Approximately 71% of the rural population in India does not treat their drinking water, and those that do typical strain the water through a piece of cloth (Fig. 1-1). While successful at removing large suspended particles and making the water appear more clean, the mesh size of this cloth is around 100-150 μm, too large to be an effective filter for most biological contaminants. Due to the cost of boiling and ineffectiveness of traditional cloth filtering, many household treatment devices have been developed with the goal of providing clean water in this context. Figure 1-2 shows four such technologies, all gravity fed filters that, when well maintained, are successful at purifying water of biological contaminants to a safe level.

A few organizations, including Tata Projects and Safe Water Network, have started to target other contaminants, including salinity. The following section will look at why this transition is important.

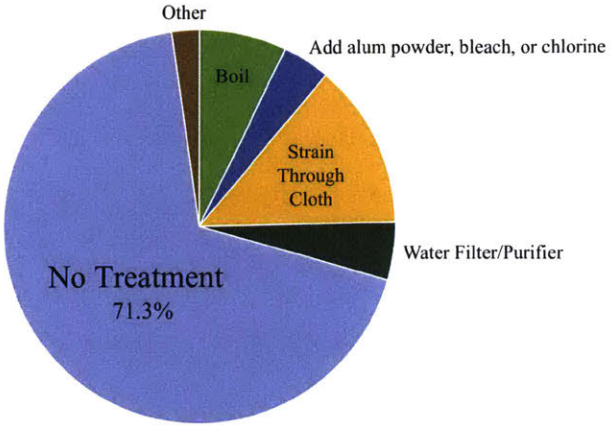

Figure 1-1: Percent distribution of rural households by method of water treatment.

Figure 1-2: Household filters that remove biological contaminants.

1.1.2 The Importance of Aesthetic Water Quality

In an attempt to better understand the issues surrounding water quality and treatment options, a series of nine interviews with residents in five different villages in Maharashtra State were completed in January 2013. While the goal of the interviews was exploratory in nature (users were asked about the source of their drinking water, water purification habits, and knowledge of household water purification devices sold in India), in seven of the nine interviews, interviewees mentioned the high salinity of their water, with statements such as the water source "tastes salty," the salinity

in the bore well made "coughing increase and it harder to digest," and that off-the-shelf household water treatment options were undesirable since they didn't remove the salty taste. The number of times that salinity was mentioned as an issue by these end users without prompt was surprising, and led to further investigation of the importance of desalination in water purification for rural villages in India.

The interview findings were substantiated through literature review. In a user study of water treatment and storage products completed in India by PATH Safe Water Project, the most common reason for selecting a water source was the source's perceived water quality, which is given by color, smell, taste, and temperature [3]. Echenique and Seshagiri [4] surveyed 400 households in Hyderabad, India, asking each to choose between five different options of water supply. Each option included a different mixture of features (quality of water, quantity of water, duration of supply, and flow rate) at different costs. The study found that users prioritize improvements in water quality over other features and thus are more willing to pay for such improvements.

TDS plays an important role in aesthetic (physical) quality. The taste quality of water in regards to salt content was first described by W.H. Bruvold in 1969 (Table 1.1) where water with TDS less than 200 mg/L is rated as excellent [5]. In addition to causing poor taste, a study by Singh et. al. [6] showed that users in India find saline water ineffective in quenching thirst and unsuitable for cooking. It is because of both the potential health effects and acceptability concerns that the Indian Standard for Drinking Water sets two limits in regards to salinity: the acceptable limit for total dissolved solids is 500 mg/L because palatability decreases and gastrointestinal irritation may occur in higher concentrations; the permissible limit if no other source is available is 2000 mg/L [7].

Potability	Excellent	Good	Fair	Poor	Unacceptable
TDS Value (mg/L)	< 200	201-600	601-1000	1001-1300	> 1300

Table 1.1: Taste quality as a function of TDS [5].

1.1.3 Brackish Groundwater as the Primary Drinking Water Source

The National Drinking Water Supply Programme and the Accelerated Rural Water Supply Programme (ARWSP) were launched in 1969 and 1971, respectively. Both programs led to rapid expansion of water supply in rural areas. Over the course of the next two decades, 1.2 million bore wells were dug and 17,000 piped water supply schemes were provided [8]. Groundwater wells were considered the least expensive and easiest to replicate method of providing rural water supplies, while avoiding the most important biological quality concerns. During the 1980s, India joined the International Drinking Water Supply and Sanitation Decade with the goal of providing safe drinking water to all villages [9].

According to the 2015-2016 National Family Health Survey [10], over 60% of the rural population in India uses some form of groundwater as their drinking water source (Fig. 1-3, right). The percentage could be as high as 94%, given that some portion of piped water also comes from a groundwater source, which is not tracked in the survey. While the rapid expansion of wells in Indian villages brought about safer drinking water sources in terms of biological quality, water quality testing received little attention until the 1990s when issues of chemical contamination including arsenic, fluoride, nitrates, and brackishness (salinity) started to appear around the country [9]. Analyzing maps created by the Central Groundwater Board of India (Fig. 1-3, left), we see that salinity levels above the taste threshold (>500 mg/L)

underlie 60% of the land in India [11]. Along with the health effects associated with high sodium intake, saline water is undesirable to users because of its poor taste, as discussed in Section 1.1.2.

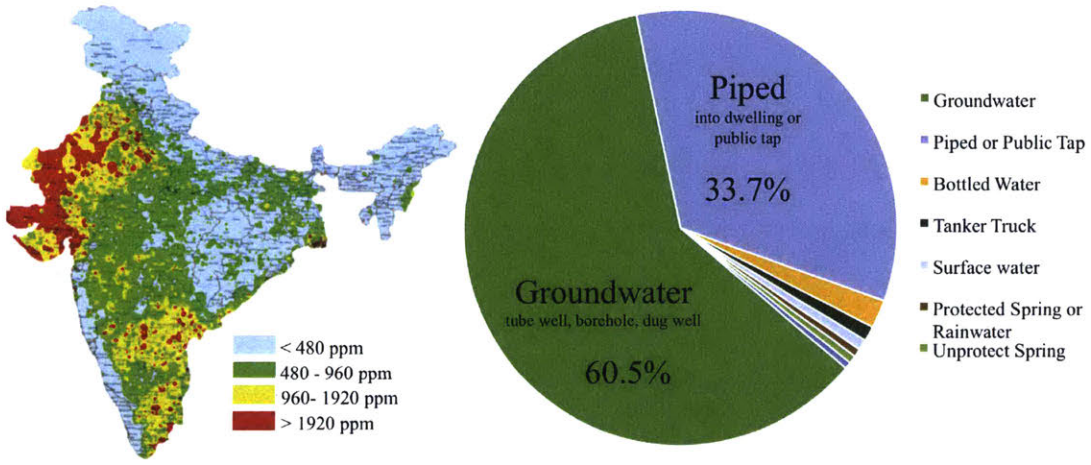

Figure 1-3: Percent distribution of rural households by primary source of drinking water.

1.2 Design Requirements for a Village-Scale Water-Treatment Plant

With the prevalence of groundwater salinity across India (>60% of the land area), number of people using groundwater as their primary drinking water sources (>60% of the rural population), and the effect that saline water appeared to have on consumers' use of water treatment devices, it was prudent to look at desalination, in additional to removal of biological contaminants.

The following system design requirements were elucidated though a combination of technical literature review and engagement with end users, NGOs, manufacturers,

government officials, and industry leaders working directly in the Indian market. Justification for each requirement is explored in greater depth in previous work [12].

1. Contaminant Removal: Biological and chemical contaminants reduced to levels recommended by the WHO. Total dissolved salts (TDS) reduced to less than 500 mg/L.[1]

2. Daily Water Output: 6-15 m^3/day. This range was based on an average water requirement for adults in developing countries of 3 liters per person per day [13, 14] and data from the Indian Census which revealed that the median villager lives in a vilage of 2,000-4,999 people [1].

3. Recovery Ratio: Maximized. The recovery ratio of a desalination system is defined as the ratio of product water volume to feed water volume. Having 15% of the world's population but only 6% of the world's water resources, India is designated as a water-stressed country [15]. In the regions of India that require desalination, groundwater supply is also limited, and a high recovery ratio means more efficient use of that limited water resource [12].

4. Energy Source: Grid and/or solar. During interviews with NGOs that have installed rural water purification plants, it was discovered that the capacity of the system has historically been sized from the number of hours of available power each day [16, 17]. For example, if a village needs a total of 6,000 liters per day and power is available for 6 hours, then a 1,000 liter per hour (LPH) plant is acceptable. However, if that same village only has access to power for 2 hours, then a 3,000 liter per hour system is needed, greatly increasing the capital cost-cost of installation. If grid power is not available, studies have shown that solar power is the most cost-effective alternative in a village-scale system [18, 19]. The average solar irradiance received in India is 4-6 kWh/m^2/day, where areas of high solar resource tend to correspond to areas of high groundwater salinity [12].

5. Maintenance: System able to be maintained in the field by a village operator with limited technical training.

[1] Feedback from recent field pilots has suggested that the desired product TDS could be as low as 100 mg/L in some communities, especially where RO product water is already available.

6. Capital Cost: Desalination skid less than Rs 355,000 ($\approx$ \$5,900). Reverse osmosis (RO) desalination plants designed and implemented by Tata Projects were studied due to their history of economic sustainability on-grid. The requirement given here is based on the cost of their 1,000 L/h on-grid RO plant [16, 12].

This thesis focuses primarily on the final requirement by determining the cost-optimal operating modes and stack architectures for electrodialysis, an existing desalination technology with the potential to be more effective than the existing village-scale RO plants installed by Tata Projects in rural India.

1.3 Merits of Electrodialysis (ED) Desalination

ED is a membrane-based desalination technology used to treat approximately 425,000 m^3 of brackish water (salinity <3,000 mg/L) daily [20]. While this accounts for only 6% of the total brackish water desalination capacity (86% is completed using reverse osmosis (RO)) [20], the growing demand for low cost, low energy consuming, high-recovery brackish water desalination solutions has created a renewed interest in ED [12, 21, 22, 23, 24, 25].

In the ED process, saline water is circulated through a stack (Fig.1-4) containing a series of alternating anion exchange membranes (AEM) and cation exchange membranes (CEM) between two electrodes. When an electric potential difference is applied across the stack, anions are drawn towards the anode, and cations towards the cathode. AEMs only pass anions, while the CEMs only pass cations, therefore generating alternating channels of diluate and concentrate.

Our previous work compared ED to other potential desalination technologies including reverse osmosis (RO) [12]. Reverse osmosis is a technology that uses an applied pressure greater than the osmotic pressure of the feed stream to move water

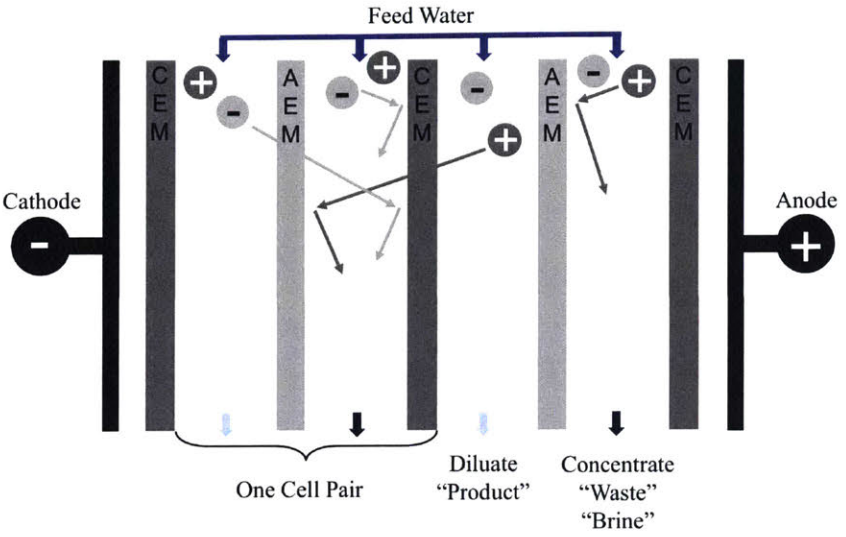

Figure 1-4: Electrodialysis (ED) is the process of drawing ions out of a feed solution by applying an electric potential across a series of alternating anion (AEM) and cation (CEM) exchange membranes.

through a semi-permeable membrane. The applied pressure forces water to move in the opposite direction of the natural flow that occurs in osmosis. Strathmann (1981) compared the process costs ($\$/m^3$) of installed large-scale ED and RO plants and found that ED is more cost effective than RO for feed water salinities less than 5,000 mg/L [26]. As changing component costs, operation modes, production rates, and installation locations (among other factors) all affect the specific process cost, it is difficult to pinpoint an exact cross-over salinity. Instead, we hypothesize that ED may have a lower specific cost for the village-scale (6-15 m^3/day) systems of interest here, considering the specific energy consumption, recovery, and maintenance, relative to the village-scale RO plants currently installed in India, and thus is worthy of further investigation.

An initial analysis showed that throughout the range of groundwater salinity

found in India, and at the 1000 L/h size scale, ED was expected to require anywhere from 25-70% less specific energy (kWh/m^3) than the RO systems currently operating in rural India [12]. For the village-scale RO plants we visited, the applied pressure was 5-13 bar above the osmotic pressure of the brine stream. Although the brine stream leaves the membrane at a pressure over the osmotic pressure, which could be recovered using an energy recovery device (ERD), the stream has a flow rate and pressure that are too small for the energy savings to make up for the capital investment of currently available ERDs [16]. This, in combination with the low efficiency ($0.20<\eta_{\text{pump}}<0.40$) of small pumps in general, and the local pumps in particular, increases the specific energy consumption of RO for small-scale brackish water desalination in comparison to larger-scale systems. While ED systems also require pumps to circulate the diluate and concentration streams (and thus are affected by the poor pump efficiency at this size scale), ED systems operate at lower pressures. Additionally, pumping is only part of the energy consumption in ED, as ion transfer is driven by the application of current.

In addition, the RO membrane modules are currently being replaced every 3-5 years, whereas ED membranes used for brackish water desalination typically last 10+ years in the field, resulting in fewer visits by highly trained technicians. Pretreatment costs are also typically lower for an ED system than an RO system, as ED can run successfully with higher levels of chlorine and turbidity in the feed water. Finally, ED systems typically operate at higher recoveries than that observed at the rural RO plants we visited (60-95% vs. 30-60%) with the exact value dependent on the composition of the feed water in both cases.[2] All of these considerations led to the hypothesis that ED has the potential to reduce the cost, energy, and water waste

[2]Note that a recovery of 30-60% is atypical for larger scale brackish water RO plants which frequently operate with a recovery between 70 and 90%.

as compared to the existing village-scale RO plants.

Finally, we note that a desalination system could include multiple technologies, for example ED could be used in combination with RO or nanofiltration (NF). As described in Section 1.2, the desired product water concentration of our system lies between 100 and 500 mg/L, depending on the local conditions and customer demands. In an ED system, as the product water concentration decreases, it becomes more expensive (both in terms of capital cost and energetic cost) to remove each additional mole of salt, a relationship discussed further in Section 2.2.2. As a result, it may be beneficial to design a hybrid ED-RO system in which the RO acts to bring the product water to its final concentration and ED acts to concentrate the brine, such as proposed by McGovern *et al.* [21, 27]. In this work we determine the cost-optimal design of a desalination system that utilizes ED technology alone and discuss the capital and operational cost ramifications of reducing the product water salinity beyond 500 mg/L, saving both the optimization of village-scale RO and hybridization of ED with RO or NF for future consideration.

1.4 Partner Organization: Tata Projects

In 2015, the Global Engineering and Research (GEAR) Lab at the Massachusetts Institute of Technology (MIT) and Tata Projects (Tata) initiated a collaboration to design village-scale, solar-powered desalination system for use in rural India. Tata's Utility Services arm already provides a range of reverse osmosis (RO) and ultrafiltration (UF) water treatment plants in the same production range of interest (typically 500-2000 L/h). As of May 2018, approximately 3000 plants had been installed across India. Their most common plant is the 1000 L/h RO plant shown in Fig. 1-5.

Due to their capabilities as a large scale manufacturer and experience in the mar-

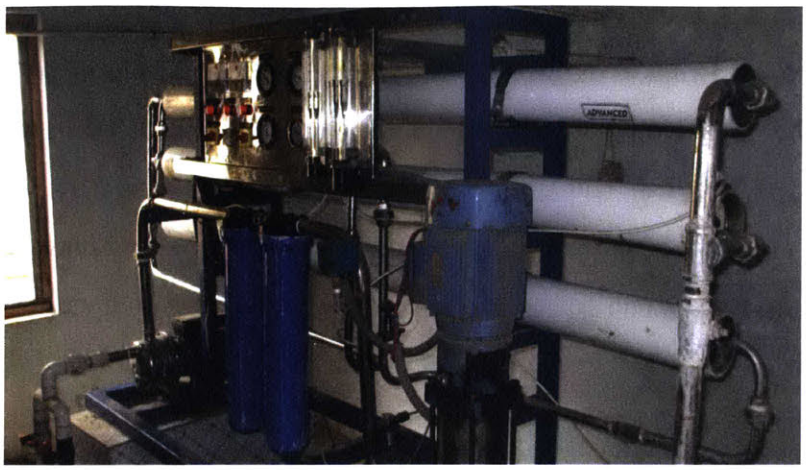

Figure 1-5: Tata Projects, based in Hyderabad India, has installed approximately 3000 reverse osmosis system (shown here) and ultrafiltration plants across India.

keting, financing, distributing, and servicing of rural desalination plants, Tata serves as a valuable partner for the further development of village-scale desalination systems in India. It is through conversation with Tata that the baseline cost and desalination targets (feed water of 2000 mg/L, product water of 200 mg/L) discussed throughout this thesis were implemented. Additionally, Tata engineers have maintained and operated the ED plant in Chelluru, India installed as part of this work.

1.5 Outline of thesis

Due to the prevalence of high salinity groundwater across the country, the proportion of people using groundwater as their primary drinking water source, and the affect that saline water has on consumers' use of water treatment devices, it was prudent to look at desalination, in additional to removal of biological contaminants for village-scale water treatment in India. ED was hypothesized to have a number of merits over the existing village-scale RO plants in terms of specific energy consumption,

total cost, water recovery, and maintenance and was thus chosen as the desalination strategy with which to move forward.

This thesis proposes methods of reducing the cost of electrodialysis brackish water desalination systems. An outline of the thesis is as follows:

- **Chapter 2: Robust Analytical Model of Electrodialysis with Experimental Validation**

  A model with prediction of the desalination rate, limiting current density, and total energy use including pumping energy is presented and validated against experimental data collected on ED stacks at two different size scales in a laboratory and in an Indian village.

- **Chapter 3: Cost-Optimal Design and Operation**

  The Pareto-optimal design of ED systems targeting a production rate of 1000 L/h, feed concentration of 2000 mg/L and product concentration of 200 mg/L are explored for five different operating modes.

- **Chapter 4: Design of Spiral-Wound Electrodialysis Modules**

  Learnings from the optimization study are used to develop a new stack architecture that would allow for local matching of the applied and limiting current densities in a continuous, constant voltage system.

- **Chapter 5: Conclusions**

  The results of the thesis are summarized and connected, and suggestions for future work are outlined.

Bibliography

[1] Datanet India Pvt. Ltd. Indiastat.com: Revealing India-Statistically: State-wise Distribution of Inhabited Villages According to Population of India (Accessed 11/10/13).

[2] United Nations. The Millenium Development Goals Report 2013. Technical report, 2013.

[3] User Testing of Household Water Treatment and Storage Products in Andhra Pradesh, India. Technical report, Program for Appropriate Technology in Health (PATH), 2011.

[4] Marcial Echenique and Raghavendra Seshagiri. Attribute-based willingness to pay for improved water services: a developing country application. *Environment and Planning B: Planning and Design*, 36(3):384–397, 2009.

[5] William H. Bruvold. Mineral taste and the potability of domestic water. *Water Research*, 4(5):331–340, May 1970.

[6] Nandita Singh, Prosun Bhattacharya, Gunnar Jacks, and Jan-Erik Gustafsson. Women and Modern Domestic Water Supply Systems: Need for a Holistic Perspective. *Water Resources Management*, 18(3):237–248, June 2004.

[7] Bureau of Indian Standards. Drinking Water - Specification (Second Revision : IS 10500). ISO 10500, 2012.

[8] Indira Khurana and Romit Sen. Drinking water quality in rural India : Issues and approaches. *WaterAid*, (288701), 2006.

[9] R. V. Rama Mohan. Rural Water Supply in India: Trends in Institutionalizing People's Participation. *Water International*, 28(4):442–453, December 2003.

[10] International Institute for Population Sciences (IIPS) and ICF. National Family Health Survey (NFHS-4), 2015-2016: *India*. Mumbai: IIPS. Technical report, 2017.

[11] Central Ground Water Board. Ground Water Quality in Shallow Aquifers of India. Technical report, Government of India, 2010.

[12] Natasha C. Wright and Amos G. Winter V. Justification for community-scale photovoltaic-powered electrodialysis desalination systems for inland rural villages in India. *Desalination*, 352:82–91, 2014.

[13] Peter H. Gleick. Basic Water Requirements for Human Activities: Meeting Basic Needs. *Water International*, 21(2):83–92, June 1996.

[14] Guy Howard and Jamie Bartram. Domestic Water Quantity, Service Level and Health. Technical report, World Health Organization, Geneva, 2003.

[15] Igor S. Zektser and Everett G. Lorne. Groundwater Resources Of The World and Their Use. Technical report, UNESCO, Paris, 2004.

[16] Anand Kumar. Personal Conversation with Mr. Anand Kumar, Tata Projects Water Purification Plant Development Center, Secunderabad, India. January 2014.

[17] Sumantra Mitra. Personal Conversation with Mr. Sumanta Mitra, Safe Water Network Head of Operations, Warangal, India. August 2013.

[18] Tinu Abraham and Amit Luthra. Socio-economic & Technical Assessment of Photovoltaic Powered Membrane Desalination Processes for India. *Desalination*, 268(1-3):238–248, 2011.

[19] Amy M. Bilton, Richard Wiesman, A.F.M. Arif, Syed M. Zubair, and Steven Dubowsky. On the feasibility of community-scale photovoltaic-powered reverse osmosis desalination systems for remote locations. *Renewable Energy*, 36(12):3246–3256, December 2011.

[20] Desaldata. Analysis, 2017.

[21] Ronan K. McGovern, Syed M. Zubair, and John H. Lienhard V. The cost effectiveness of electrodialysis for diverse salinity applications. *Desalination*, 348:57–65, 2014.

[22] Karim M. Chehayeb, Daniel M. Farhat, Kishor G. Nayar, and John H. Lienhard V. Optimal design and operation of electrodialysis for brackish-water desalination and for high-salinity brine concentration. *Desalination*, 420:167–182, 2017.

[23] Kishor G. Nayar, P. Sundararaman, J. D. Schacherl, C. L. O'Connor, Michael L. Heath, Mario O. Gabriel, Sahil R. Shah, Natasha C. Wright, and Amos G Winter V. Feasibility Study of an Electrodialysis System for In-Home Water Desalination in Urban India. *Development Engineering*, 2:38–46, 2016.

[24] REvivED Water Consortium. Low energy solutions for drinking water production by a revival of electrodialysis systems, 2016.

[25] H. Strathmann. Electrodialysis, a mature technology with a multitude of new applications. *Desalination*, 264(3):268–288, 2010.

[26] H. Strathmann. Membrane Separation Processes. *Journal of Membrane Science*, 9:121–189, 1981.

[27] Ronan K. McGovern, Syed M. Zubair, and John H. Lienhard V. The benefits of hybridising electrodialysis with reverse osmosis. *Journal of Membrane Science*, 469:326–335, 2014.

THIS PAGE INTENTIONALLY LEFT BLANK

Chapter 2

Robust Analytical Model of Electrodialysis with Experimental Validation

Contributors

This chapter was co-authored by Sahil R. Shah, Susan E. Amrose, and Amos G. Winter V.

Abstract

This chapter presents a robust analytical model for brackish water desalination using electrodialysis (ED), with prediction of the desalination rate, limiting current density, and total energy use including pumping energy. Several simplifying approximations make the model easier to implement for simulation and design optimization

purposes. The predicted desalination rate, limiting current density, and total energy usage agree with measurements across two diverse ED stack designs, differing in total membrane area (0.18 m^2, 37.1 m^2), membrane manufacturers (GE Water, PCA GmbH), and flow channel spacers, thus demonstrating the model's flexibility. The commercial-scale stack was additionally tested with real groundwater in Chelluru, India, demonstrating that brackish groundwater may be modeled as an equivalent concentration NaCl solution. Sensitivity to the membrane diffusion coefficient, area available for ion transport, level of discretization along the flow channel length, boundary layer and membrane resistances, and water transport are analyzed to guide empirical characterization when higher accuracy is required. No single existing model for pressure drop in the membrane spacers could accurately predict pumping power in both stacks. One model for each stack was found to reasonably approximate pressure drop, however experimental validation of specific spacer designs is recommended. The fully quantitative, parametric description of electrodialysis behavior presented here forms a useful tool to design, evaluate, and optimize ED systems, as required in Chapters 3 and 4.

2.1 Introduction: Limitation of Existing Models

There are several approaches to modeling ED systems that span from simple polynomial correlations [1] and analytic derivations [2, 3] to computational fluid dynamics (CFD) simulations [4, 5]. Simple correlations do not maintain fidelity over a broad range of system configurations while CFD solutions have a high computational cost. There is a need to predict desalination performance and pressure losses across the wide variety of ED systems used in water treatment using models that are less computationally intensive, in order to facilitate parametric design studies.

Several authors separately model the mass transfer [2, 6], limiting current density [7, 8, 9], and pressure losses throughout the ED membrane stack [10, 11, 12, 13, 14]. However, few authors have united all of these aspects into a single model. A combined model is critical to develop a complete understanding of the behavior of an ED system. For example, while increased linear flow velocity (obtained by increased flow rate, thinner channels, or lower spacer void fractions) increases mass transfer rates and raises the limiting current density, it also increases the pressure drop over the stack, thereby increasing total energy consumption. Including these types of coupled interactions improves the accuracy of the model as well as its usefulness as a tool to design and optimize ED systems for performance, cost, and energy consumption.

Of the few models that do consider combined effects [15, 6, 3, 16], all rely on empirically derived parameters that require experimental characterization of a specific ED system prior to use of the model. In this chapter, I present further experimental validation of their work, and simplifying approximations that predict, with good accuracy, the performance of stack configurations that deviate from those tested by other authors.

2.2 Model description

This section describes three interdependent models to predict the desalination rate and total energy consumption for the ED process described above. First, we use a circuit analogy to model the rate of ion transfer (in the form of current) as a function of the applied voltage and given diluate and concentrate concentrations, in Section 2.2.2. Next, Section 2.2.3 provides a mass transfer model to predict the concentration along the ED stack as a function of current and time. The current and concentration in the channels are interdependent, and therefore solved simultaneously. Lastly,

section 2.2.7 models the pressure drop over the ED stack as a function of geometric properties and the flow rate in the channels. While this third model can be solved independently, the desalination rate and maximum applied current depend on the flow rate through the system. In order to estimate the flow rate for a given stack-pump combination, or the pressure drop at a desired flow rate, and subsequently understand the resulting energetic and desalination rate repercussions, it is prudent to consider all three models simultaneously.

2.2.1 Variables and setup

We begin by considering the geometric and concentration variables for a single cell pair (Fig. 2-1). Molar concentration is denoted by C, where the superscript denotes the bulk, C^b, the AEM surface, C^{AEM}, or the CEM surface, C^{CEM}. The first subscript defines the concentration as being either in the diluate or concentrate channel (C_d and C_c, respectively), and the second subscript denotes the lengthwise segment of the channel, y. The segment of the channel provides discretization for modeling purposes only; ED stacks are not physically segmented in this manner.

C_d decreases in the direction of flow until the final segment, $y = Y$. The opposite is true for C_c. Within any given segment (for example, $y = 2$), the volume is considered small enough such that both the bulk and membrane surface concentrations are assumed to be length-wise constant. When a voltage is applied, a concentration boundary layer of thickness δ extends from the membrane surfaces, where the concentration is $C_{d/c}^{AEM/CEM}$, to the bulk, where the concentration is $C_{d/c}^{b}$ (Fig. 2-1).

This model assumes that the same flow conditions exist in the diluate and concentrate channels. This is standard practice in commercial ED stacks to ensure that the pressure difference across the membranes is negligible and does not contribute

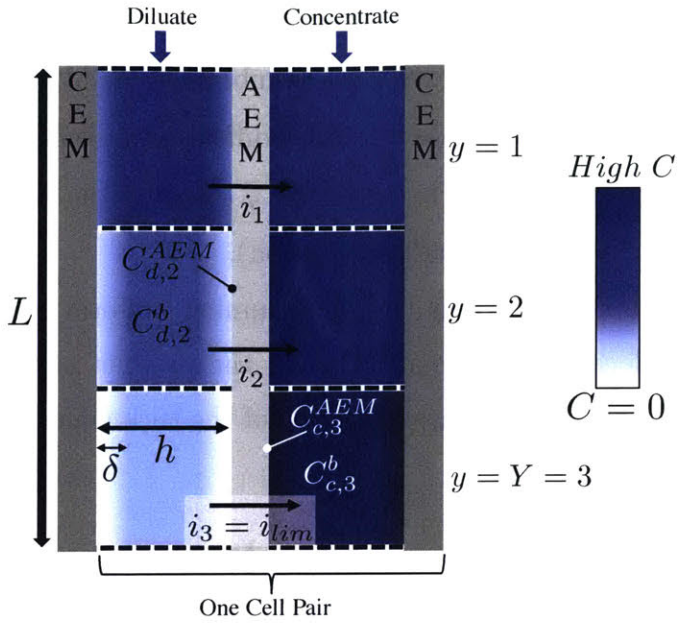

Figure 2-1: Description of key dimensions and notation.

to water transport. Both channels are the same dimensions and utilize the same turbulence-promoting spacer. This model assumes that the feed water contains a single 1:1 electrolyte. The extent to which it can be applied to solutions containing divalent ions is discussed in 2.5.7.

2.2.2 Circuit analogy and current calculation

The ED stack is modeled as an analogous DC circuit whereby the voltage applied at the electrodes (E_{total}), and the resulting current are related by

$$E_{\text{total}} = E_{\text{el}} + NE_y^{\text{mem}} + Ni_y(R^b_{d,y} + R^b_{c,y} + R^{BL}_y + R^{AEM} + R^{CEM}), \qquad (2.1)$$

where N is the number of cell pairs in the stack, and i_y is the per-segment current density (A/m^2). The area resistances $R^b_{d,y}$, $R^b_{c,y}$, R^{BL}_y, R^{AEM}, and R^{CEM} are asso-

ciated with the bulk diluate and concentrate streams, the concentration boundary layers lumped together, and the exchange membranes (AEM, CEM), respectively (Ω m^2). Finally, E_{el} is the electrode potential difference and E_y^{mem} is the potential across each membrane-pair (V). The subscript y refers to the segment of the stack in all cases (Section 2.5.3 discusses discretization).

The total instantaneous current (I_{total}), assuming uniform segmentation, is the sum of all current densities (i_y), multiplied by the product of the segment length (L/Y), width (W), and the open-area porosity of the turbulence-promoting channel spacer (ϕ_A) as given in Eq. 2.2.

$$I_{\text{total}} = \phi_A(\frac{WL}{Y})\sum_{y=1}^{Y} i_y \tag{2.2}$$

The area resistances in Eq. 3.16, and thus I_{total}, vary with concentration along the length of the stack, and may also vary with time for unsteady operation, as is the case for batch processes.

For desalination of pure sodium chloride, the reduction of hydrogen ions at the cathode and the oxidation of chloride ions at the anode maintain a standard cell potential of 1.4 V for the electrodes. The actual potential, which can be estimated using the Nernst equation, is dependent on temperature and ion concentration. For a standard ED stack, which typically contains more than 300 cell-pairs with each contributing ~1 V per cell pair, the electrode potential E_{el} is negligible. The remaining terms in Eq. 3.16 are evaluated in the following sections.

Area resistances

The area resistances of the bulk and boundary layers ($R_{d,y}^b$, $R_{c,y}^b$, R_y^{BL}) can be found by first calculating the equivalent conductance of the solution using an empirical

relationship for the specific aqueous solution. The Onsager/Falkenhagen equation for 1-1 electrolytes (Eq. 2.3) presents good agreement with experimental data over a temperature range of 5-65°C, and for solutions up to 30 g/L (Fig. 2-2) [17]. Since we are specifically interested in modeling brackish water desalination, use of the Onsager/Falkenhagen equation is justified for modeling the resistances of both the diluate and brine channel. The equivalent conductance at the concentration of interest is given by

$$\Lambda_C = \Lambda_0 - (B_1\Lambda_0 + B_2)\frac{\sqrt{C * 10^{-3}}}{1 + B_0 a\sqrt{C * 10^{-3}}}, \tag{2.3}$$

where C is the concentration of the solution (mol/m^3); a, B, B_1, and B_2 are unitless empirically-determined coefficients dependent on the temperature of the solution (Table 2.1), and Λ_0 is the equivalent conductance at infinite dilution (temperature and electrolyte dependent, Scm^2/mol). For models in which the diluate channel concentration is above 0.1 mol/L, we recommend the review of conductivity models and their range of application prepared by De Diego *et al.* [18]. The resistivity, ρ (Ω m), of the solution at a concentration C is then

$$\rho = \frac{1}{\Lambda_C C}. \tag{2.4}$$

The dominant resistance in brackish water desalination using ED is the resistance of the diluate channels because resistivity increases sharply at low concentrations (Fig. 2-3). Resistivity is also temperature dependent; the resistivity at 30°C is 20% less than at 20°C over the concentration range 0.5 - 50 mol/m^3. Therefore, groundwater temperature variation with location or time may produce non-negligible variation in resistivity.

Equations 2.3 and 2.4 are used to determine all diluate and concentrate stream

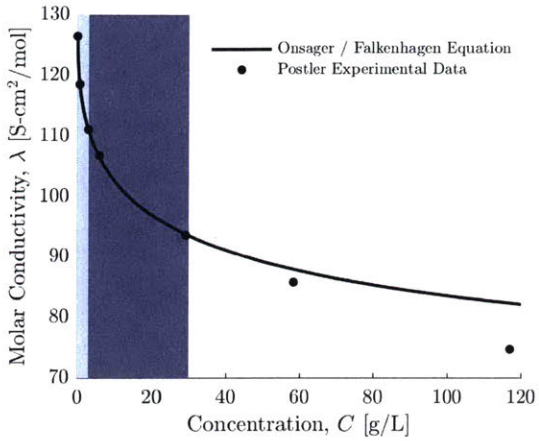

Figure 2-2: The Onsager/Falkenhagen equation for predicting the molar conductivity of aqueous NaCl at 25°C plotted with experimental measurements made by Postler [19]. Good agreement is achieved at concentrations below 30 g/L. Light and dark blue regions represent the typical concentration ranges seen in the diluate channel ($C_d < 3$ g/L) and concentrate channel ($3 < C_c < 30$ g/L), respectively.

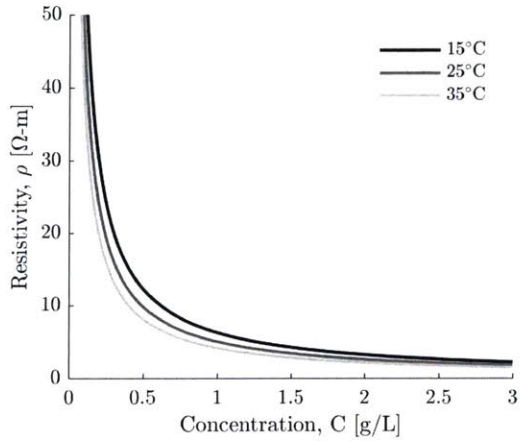

Figure 2-3: Resistivity of an aqueous NaCl solution at varying concentrations and temperatures. The resistivity of a fluid at 35°C is approximately 20% less than that of a solution at the same concentration but at 25°C. Because groundwater temperature varies significantly based on well location and depth to water table, it may be necessary to account for site-specific temperature.

Table 2.1: Constants of the Onsager/Falkenhagen equation (Eq. 2.3) for the equivalent conductance of electrolytes in water at various temperatures [17]. Λ_0 and a are for NaCl specifically, while all other parameters are valid for all 1-1 electrolytes.

	20°C	**25°C**	**30°C**	**40°C**
B_0	0.3276	0.3286	0.3297	0.3318
B_1	0.2269	0.2289	0.2311	0.2357
B_2	53.48	60.32	67.54	82.97
Λ_0	113.76	126.45	140.11	168.2
a(Å)	4	4	4	4

resistances in

$$R^b_{d,y} = \rho^b_{d,y}(h - 2\delta), \tag{2.5}$$

$$R^b_{c,y} = \rho^b_{c,y}(h - 2\delta), \tag{2.6}$$

$$R^{BL}_y = R^{AEM}_{d,y} + R^{CEM}_{d,y} + R^{AEM}_{c,y} + R^{CEM}_{c,y}, \text{and} \tag{2.7}$$

$$R^{AEM}_{d,y} = \frac{(\rho^b_{d,y} + \rho^{AEM}_{d,y})}{2}\delta. \tag{2.8}$$

All four boundary layer resistances in Eq. 2.7 are evaluated as shown in Eq. 2.8, which is specified for the diluate-AEM interface. The resistances are calculated using a mean concentration, and approximate resistivity as varying linearly over small concentration changes. Although the boundary layer resistance could be resolved more accurately, a linear approximation is sufficient because the contributions of the boundary layer resistances to the total resistance are small since δ is small with respect to the flow channel height (see Section 2.5.5).

Membrane resistances (R^{AEM}, R^{CEM}) are often provided by the manufacturer. However, these values are typically given at a single concentration while the effective membrane resistance is known to change with concentration of the solution contacting either side of the membrane [20]. The membrane resistance can be experimentally

determined as a function of concentration. Here, we make the simplification that it is constant, provided that the diluate and concentrate concentrations being tested are near the concentration at which the membrane was characterized.

Membrane potential

The potential associated with the concentration difference across the exchange membranes (E_y^{mem}) is the sum of contributions from the AEM (E_y^{AEM}) and the CEM (E_y^{CEM}), given by

$$E_y^{AEM} = \frac{(2t^{AEM} - 1)RT}{F} \log(\frac{\gamma_c C_{c,y}^{AEM}}{\gamma_d C_{d,y}^{AEM}}), \text{ and} \tag{2.9}$$

$$E_y^{CEM} = \frac{(2t^{CEM} - 1)RT}{F} \log(\frac{\gamma_c C_{c,y}^{CEM}}{\gamma_d C_{d,y}^{CEM}}), \tag{2.10}$$

where R is the gas constant (J/mol-K), T is temperature (K), F is Faraday's constant (C/mol), and γ is the activity coefficient of the solution. t^{AEM} and t^{CEM} are the apparent transport numbers of the counterions (the anions in the AEM and cations in the CEM, respectively). These numbers account for the fraction of total current carried by the counterion across each respective membrane by migration. Measurements performed by McGovern *et. al.* [21] for a cell-pair, $t^{AEM,CEM} = 0.96 \pm 0.04$ for concentrations below 10,000 mg/L. At ~7500 mg/L diluate, membrane manufacturers have reported transport numbers ranging from 0.90 (Membranes International) to >0.96 (PCA GmbH). Therefore, at the low brackish water concentrations that are the focus of the present study (< 10,000 mg/L), it is reasonable to approximate both membranes as perfectly ion-selective, and assign counter-ion transport numbers of 1.

The activity coefficient γ depends on the solution's ionic strength and temperature. Data tables and theoretical expressions for a variety of electrolytes and concen-

tration ranges can be found in Robinson and Stokes [22]. Extending the Debye-Hückel formula to fit measured activity coefficients (± 0.003) for NaCl over $1 \leq C \leq 2000$ mol/m^3 gives:

$$-\log\gamma = \frac{0.5065\sqrt{C * 10^{-3}}}{1 + 1.298\sqrt{C * 10^{-3}}} - 0.039(C * 10^{-3}). \tag{2.11}$$

While Eq. 2.11 will show that γ varies between 0.6 and 1.0 for most brackish water and seawater desalination processes, γ is set to 1.0 for the results shown in this paper due to its very small affect on the net applied voltage. Consider, for example, a batch process desalinating 3,000 mg/L NaCl (γ=0.819) to 150 mg/L (γ=0.946) at 95% recovery using 1 V per cell-pair, and producing 57,150 mg/L brine (γ=0.659). Setting γ=1.0 in this example decreases the predicted membrane potential by less than 10%, resulting in a total stack voltage under-prediction of <1.1% over the entire duration of the batch. Given this low sensitivity, we make the simplification that γ=1.

2.2.3 Mass transfer model

A mass balance is used to determine the concentration at any given time in the ED system. Fig. 2-4 shows a representative ED system arranged for batch desalination comprised of 4 cell pairs, showing 3 discretization units ($Y = 3$). The system contains the ED stack and two tanks through which the diluate and concentrate solutions are each continuously recirculated (the diluate through the diluate tank and the concentrate through the concentrate tank).

The rate of change of the concentration in the diluate and concentrate tanks is fully defined by the advective transport of ions (Eqs. 2.12 and 2.13). Drawing a control volume (dashed lines in Fig. 2-4) about the tanks, we obtain that the mass

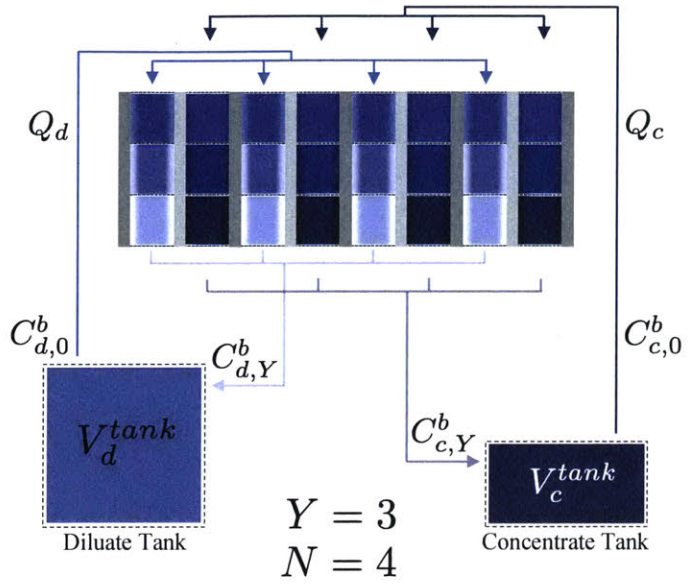

Figure 2-4: Diagram of an ED system set up for batch desalination. Dashed black lines illustrate control boundaries used in mass balance Eqns. 2.12-2.15. The ED stack shown here has N=4 cell pairs; each channel has been discretized into Y=3 segments.

balance for diluate tank is

$$\frac{dC^b_{d,0}}{dt} = \frac{1}{V_d^{\text{tank}}}[Q_d C^b_{d,Y} - Q_d C^b_{d,0}], \tag{2.12}$$

and the mass balance for concentrate tank is

$$\frac{dC^b_{c,0}}{dt} = \frac{1}{V_c^{\text{tank}}}[Q_c C^b_{c,Y} - Q_c C^b_{c,0}], \tag{2.13}$$

where $C^b_{d,0}$, $C^b_{c,0}$, $C^b_{d,Y}$, $C^b_{c,Y}$, are the concentrations of the diluate and concentrate streams at the inlet and outlet of the ED stack, Q_d, Q_c are the flow rates of the diluate and concentrate streams, and V_d^{tank}, V_c^{tank} are the volumes of water in the dilute and concentration tanks, respectively. In a continuous system, where the water is not recirculated, this tank mass-balance is not required. Instead, the feed concentration

at the inlet to the stack is typically constant.

To determine the mass balance within the ED stack, Eqs. 2.14 and 2.15 are derived from the fundamental continuity equation and the Nernst-Planck equation which describes the motion of ions under the influence of advection, an ionic concentration gradient (resulting in diffusion) and an electric field (resulting in migration). For interested readers, the derivation from fundamental equations is provided by Lee [6]. For an individual segment within a channel, we obtain the mass balance for diluate cells as

$$\frac{dC_{d,y}^{b}}{dt} = \frac{1}{NV_{y}^{\text{cell}}}[Q_{d}(C_{d,y-1}^{b} - C_{d,y}^{b}) - \frac{N\phi I_{y}}{zF} + \frac{NA_{y}D^{AEM}(C_{c,y}^{AEM} - C_{d,y}^{AEM})}{l^{AEM}} + \frac{NA_{y}D^{CEM}(C_{c,y}^{CEM} - C_{d,y}^{CEM})}{l^{CEM}}], \tag{2.14}$$

and the mass balance for concentrate cells as

$$\frac{dC_{c,y}^{b}}{dt} = \frac{1}{NV_{y}^{\text{cell}}}[Q_{c}(C_{c,y-1}^{b} - C_{c,y}^{b}) + \frac{N\phi I_{y}}{zF} - \frac{NA_{y}D^{AEM}(C_{c,y}^{AEM} - C_{d,y}^{AEM})}{l^{AEM}} - \frac{NA_{y}D^{CEM}(C_{c,y}^{CEM} - C_{d,y}^{CEM})}{l^{CEM}}], \tag{2.15}$$

where N is the number of cell pairs, ϕ is the current leakage factor, I_y is the current in the discretized segment, z is the ion charge number, F is Faraday's constant, l^{AEM} and l^{CEM} are the thicknesses of the anion and cation exchange membranes, D^{AEM} and D^{CEM} are the diffusion coefficients of the solute in the AEMs and CEMs, and $C_{c,y}^{AEM}$, $C_{d,y}^{AEM}$, $C_{c,y}^{CEM}$, and $C_{c,y}^{CEM}$ are the concentrations of the diluate and concentrate streams at the interface with adjacent AEMs or CEMs in segment y. The current leakage factor ϕ accounts for the loss of current that occurs when an electrical path parallel to the active channel area exists for the current to flow through. Current leakage is a function of the stack construction and can be assumed negligible for a well-designed stack.

Within Eqs. 2.14 and 2.15, the first term represents advective transport of ions entering

and exiting a segment, and the second term represents the migration of ions from diluate to concentrate compartment due to the electrical potential gradient, where the current I_y is found by solving Eqs. 3.16-2.10. The final two terms represent the back-diffusion of ions due to concentration differences that develop across each membrane. For batch operation, the concentration in the stack is changing with time through the desalination process; hence, the transient terms on the left of Eqs. 2.14 and 2.15 are non-zero. Conversely for a continuous system, steady-state operation can be modelled by setting these terms to zero.

Concentration at the membrane surfaces

Eqs. 2.7, 2.14 and 2.15 require the concentrations at the surfaces of the AEM and CEM exchange membranes in the diluate and concentrate channels. The surface concentration is obtained by balancing diffusion into the boundary layer with migration across the bounding membrane. For the four surface concentrations in the diluate and concentrate channels within a cell pair, this results in

$$C_{d,y}^{AEM} = C_{d,y}^{b} - \frac{\phi i_y (t^{AEM} - t_-)}{zFk}, \tag{2.16}$$

$$C_{d,y}^{CEM} = C_{d,y}^{b} - \frac{\phi i_y (t^{CEM} - t_+)}{zFk}, \tag{2.17}$$

$$C_{c,y}^{AEM} = C_{c,y}^{b} + \frac{\phi i_y (t^{AEM} - t_-)}{zFk}, \text{and} \tag{2.18}$$

$$C_{c,y}^{CEM} = C_{c,y}^{b} + \frac{\phi i_y (t^{CEM} - t_+)}{zFk}, \tag{2.19}$$

where t_- and t_+ are transport numbers of the anions and cations in solution, respectively. For NaCl the transport number of the cations is t_+ =0.39, while for the anions it is t_- =0.61 (variation <3% over a temperature range of 15-45 C and a concentration range of 0.0-0.1

mol/L) [23].

2.2.4 Water transport

Water transport through the membranes can occur due to osmosis and electro-osmosis (migration) such that the volume of the diluate tank in Eq. 2.12 decreases and the volume of the concentrate tank in Eq. 2.13 increases. We follow the work of Fidaleo and Moresi [3] to obtain the rate of change of volume (Eq. 2.20), using values of L_w and t_w measured by McGovern [21]. Transport due to osmosis is given by

$$\frac{dV_c^{\text{tank}}}{dt} = N(\frac{LW}{Y})M_{H_2O}\sum_{y=1}^{Y} L_w(\pi_{c,y} - \pi_{d,y}),$$
$$\text{where } L_w = (1.6 \times 10^{-3})(C_{c,y}^b)^{-0.416}. \tag{2.20}$$

Transport due to electro-osmosis is given by

$$\frac{dV_c^{\text{tank}}}{dt} = N(\frac{LW}{Y})M_{H_2O}\sum_{y=1}^{Y} \frac{t_w i_y}{F},$$
$$\text{where } t_w = (-1.37 \times 10^{-7})(C_{c,y}^b)^2 - (1.099 \times 10^{-3})C_{c,y}^b + 11.194. \tag{2.21}$$

In Eqs. 2.20 and 2.21, M_{H_2O} is the molar mass of water (kg/mol), L_w is the cell pair membrane water permeability (mol/bar-m^2-s), t_w is the dimensionless cell pair water transport number and $\pi_{c,y}$ and $\pi_{d,y}$ are the osmotic pressure of the concentrate and diluate, respectively (bar).

In brackish water desalination, recoveries are typically high such that larger volumes of diluate are produced compared to concentrate, and trans-membrane concentration differences are lower than in seawater desalination. As such, we do not expect water transport to have a significant effect on the modeled performance. We neglect water transport initially, and then discuss the effect of this assumption on model accuracy in Section 2.5.6.

2.2.5 Limiting current density

Due to the concentration boundary layer described in Section 2.2.1, there exists a maximum rate of ion transport that is bounded by the current density that results in a zero ion concentration at the membrane surface in the diluate channel. This phenomenon first occurs at the end of the flow path where the diluate concentration is the lowest ($y = Y$ in Fig. 2-1). The limiting current density i_{lim} (A/m^2) is estimated by setting the concentration at the AEM or CEM surface in Eqs. 2.16 and 2.17 to zero, resulting in

$$i_{lim}^{+,-} = \frac{C_d^b z F k}{t^{AEM,CEM} - t_{+,-}}, \tag{2.22}$$

where z is the valence of the ion, k (m/s) is the boundary-layer mass transfer coefficient, $t^{AEM,CEM}$ is the transport number of the counterion in the AEM or CEM membrane, and $t^{+,-}$ is the transport number of the cations or anions in the bulk solution, respectively, where its concentration is C_d^b. $t^{AEM,CEM}$ is assumed to be 1 in all cases per the discussion in Section 2.2.2. In the bulk solution, for a single 1-1 electrolyte, the limiting current is set by the lower of the two solution transport numbers. Because $t^+ < t^-$ (Section 2.2.3), $i_{lim} = i_{lim}^+$ throughout this investigation.

The boundary layer mass transfer coefficient k (m/s) depends on hydrodynamic factors, coupling the mass transfer and flow properties such that the design and operating parameters of an ED stack affect the pressure drop and subsequently, the final pump selection.

2.2.6 Coupling mass transfer to flow

By definition, the Sherwood number Sh, which is the ratio of advective to diffusive mass transport, is related to k by

$$k = \frac{ShD_{aq}}{d_h}, \tag{2.23}$$

where D_{aq} is the diffusion coefficient of the aqueous solution. For NaCl at 25°C, D_{aq}

varies from 1.61×10^{-9} m^2/s at infinite dilution to 1.47×10^{-9} m^2/s at 0.5 mol/L [24]. Approximating D_{aq} as constant at 1.6×10^{-9} m^2/s (since brackish water desalination is being considered) produces less than 6% error in the boundary layer mass transfer coefficient k over the same concentration range. The hydraulic diameter d_h as defined by Pawlowski et al. [10] is

$$d_h = \frac{4\epsilon}{2/h + (1-\epsilon)(8/h)}, \tag{2.24}$$

where ϵ is the void fraction, defined later in Eq. 2.31. Mass transfer is then correlated to the flow properties via

$$Sh = 0.29 Re_d^{0.5} Sc^{0.33} [25], \tag{2.25}$$

where the Schmidt number Sc is a material-dependent non-dimensional quantity relating the momentum and mass diffusivities, and the Reynolds number Re_d characterizes the flow. They are defined as

$$Sc = \frac{\mu}{\rho_{aq} D_{aq}}, \tag{2.26}$$

and

$$Re_d = \frac{\rho_{aq} u_{ch} d_h}{\mu}, \tag{2.27}$$

where ρ_{aq} is the density of the aqueous solution, μ is the viscosity of the solution, and the velocity in the spacer-filled channels is u_{ch} (Eq. 2.32). From Eqs. 2.23-2.27, it is evident that a high linear flow velocity in the channels will produce an increase in the mass transfer coefficient and a corresponding increase in the limiting current density. In order to increase the desalination rate, a higher linear flow velocity is advantageous, however it will also increase pressure losses through the stack.

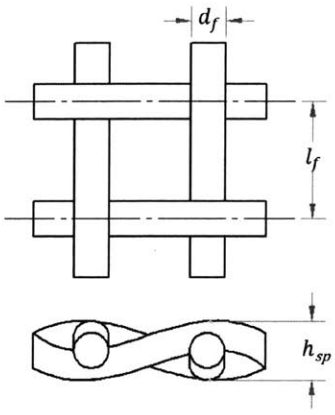

Figure 2-5: A mesh spacer is often used as a turbulence promoter in the flow channels. The filaments in this spacer are woven rather than overlapped. The spacer thickness h_{sp} is equal to the channel gap h such that that spacer touches an AEM and CEM on either side.

2.2.7 Pressure drop

This section reviews and compares four models for the pressure loss in the diluate and concentrate channels. We assume that channel losses are the dominant source of pressure loss, and test this assumption in Section 2.4.3.

Pressure drop model setup

Consider a flow channel with a mesh spacer, which is typically used in ED stacks to promote mass transfer. The variables defining the geometry of the spacer are given in Fig. 2-5. The spacer may be woven, as shown in the figure, or overlapped, where filaments running in one direction are always above filaments running in the other direction.

In all the following cases, the pressure drop model presented by the original authors (Ponzio *et al.*, Pawlowski *et al.*, Gurreri *et al.*, and Kurdo *et al.*) will be translated to the Darcy-Weisbach equation for flow between two parallel flat plates, allowing straightforward comparison of friction factor predictions:

$$\Delta P = \frac{\rho_{aq} f L u_v^2}{4h}. \tag{2.28}$$

Here f is the Darcy friction coefficient, L is the length of the channel's active area (m), and h is the channel gap, assumed equal to the spacer thickness h_{sp} (m), unless otherwise noted. The void channel velocity u_v (m/s) (velocity with no spacer present) is related to the volumetric flow in each circuit Q by

$$u_v = \frac{Q}{WhN}, \tag{2.29}$$

where W is the width of the active area (m) and N is the number of cell-pairs. The standard definition of the Reynolds number Re for flow between two parallel flat plates is used, giving

$$Re = \frac{2\rho_{aq} u_v h}{\mu}. \tag{2.30}$$

The void fraction ϵ is the ratio of open volume to total volume in the spacer filled channel (Eq. 2.31). It determines the actual flow velocity (Eq. 2.32) in the channel and is important for both mass transfer and pressure drop calculations.

$$\epsilon = 1 - \frac{\pi d_f^2}{2 l_f h} \tag{2.31}$$

$$u_{ch} = \frac{Q}{\epsilon WhN} \tag{2.32}$$

The pressure drop (and associated friction factor f) is approximated by several authors through a series of CFD and/or experimental results. We present these models and compare their predictions against our experiments in Section 2.4.3.

Ponzio pressure drop model

Ponzio *et al.* investigated the relationship between friction factor and Re (Eq. 2.33) for woven spacers in various orientations for Re of 2–2,000 [12]. The transition out of creeping flow was modeled using CFD and observed experimentally. Using the data provided, and their observation that the friction factor scales with Re^{-1} for low Re and with $Re^{-0.37}$ for high Re, we derived the following relationship.

$$\begin{aligned} f &= \frac{1400}{Re} \quad for \quad Re < 61 \\ f &= \frac{104.5}{Re^{0.37}} \quad for \quad Re \geq 61 \end{aligned} \tag{2.33}$$

These results are limited to woven spacers where $l_f/h_{sp} = 2$ and $l_f/d_f = 4$. As the void fraction is a function of these two ratios alone (Eq. 2.31), maintaining them as constant dictates that our predictions for pressure drop using Ponzio *et al.*'s model could only be calculated for a single void fraction of $\epsilon = 0.8$.

Pawlowski pressure drop model

The channel model implemented by Pawlowski *et al.* [10] is a modified version of the Darcy Weisbach equation for flow between two infinite parallel flat plates. It utilizes a modified channel hydraulic diameter that accounts for the void fraction (Eq. 2.24) and the actual flow velocity u_{ch} rather than the void channel velocity u_v.

$$\Delta P = \frac{48 \mu L u_{ch}}{d_h^2} \tag{2.34}$$

The hydraulic diameter used here, and presented in Eq. 2.24, is a simplification of the relationship provided by Da Costa [26]. Pawlowski *et al.* assume that the thickness of the spacer h_{sp} is equal to the height of the channel h, and that the thickness of the spacer is exactly two times the diameter of the filament ($h_{sp} = 2d_f$). In reality, the filaments are

slightly compacted against each other such that $h_{sp} < 2d_f$.

The following expression is Pawlowski *et al.*'s formulation translated into a friction factor that can be substituted into Eq. 2.28 for comparison to the correlations proposed by other authors:

$$f = \frac{24(2 + 8(1 - \epsilon))^2}{\epsilon^3 Re}. \tag{2.35}$$

Pawlowski *et al.* do not provide a range of Re or conditions over which this equation is expected to be valid.

Gurreri pressure drop model

Gurreri *et al.* [13] used CFD to investigate the pressure drop in the flow channel for both woven and overlapped spacers, with Reynolds numbers ranging from 1 to 64. The thickness of the spacer was assumed to be 1.8 times the diameter of the filament to account for the compaction that occurs where the filament strands cross. The geometries covered had l_f/h ratios of 2 ($\epsilon = 0.76$), 3 ($\epsilon = 0.84$), and 4 ($\epsilon = 0.88$). Translating Gurerri *et al.*'s results into a friction factor that can be substituted into Eq. 2.28 for comparison gives

$$f = 4\frac{40.37}{\epsilon^{5.35} Re} \tag{2.36}$$

for overlapped spacers, and

$$f = 4\frac{50.60}{\epsilon^{7.06} Re} \tag{2.37}$$

for woven spacers. Both friction factors are multiplied by 4 to convert from the Fanning friction factor used in Gurreri *et al.*'s paper to the Darcy friction factor used here. Note that we have applied a power law correlation on the void fraction to fit the data presented in Gurreri *et al.*'s work ($R^2 = 0.998$). However, their dataset contained only three data points and a linear fit ($R^2 = 0.990$) would have been equally appropriate. It is thus recommended

that this correlation only be used within the range of void fractions investigated by Gurreri *et al.*

Kuroda pressure drop model

Finally, we consider a pressure drop correlation developed by Kuroda *et al.* [14]. Their experimental analysis considers four different mesh spacers. Unlike the models produced by Ponzio *et al.*, Pawlowski *et al.*, and Gurreri *et al.*, where the spacer thickness h_{sp} is assumed to be equal to the channel thickness h, here the mesh thickness fills between 50 and 71% of the channel thickness. The experimentally determined correlation for the 0.5 mm thick spacer in a 1.0 mm channel has been used in recent ED models [16, 27] and is given by

$$f = 4\frac{9.6}{\epsilon Re^{0.5}}. \tag{2.38}$$

Kuroda *et al.* also provide a correlation to connect all four tested spacers. In that correlation, $f = f(h^{0.5}, \epsilon^{-0.5}, l_f^{-0.57}, g^{-1})$, where g is the gap between the mesh spacer and the membrane (the channel wall) such that $g = h - h_{sp}$. Since this gap height is in the denominator of the fitting function, the correlation cannot be used directly for most ED stacks where g=0. Using the same data set, we reformulated the correlation using the spacer thickness instead of the gap height, such that $f = f(h^{0.5}, \epsilon^{-0.5}, l_f^{-0.119}, h_{sp}^{-1})$. The resulting correlation for all four spacers is

$$f = 4\frac{0.0557\sqrt{2h\epsilon}}{\epsilon Re^{0.5} l_f^{0.119} h_{sp}}, \tag{2.39}$$

where spacer dimensions must be given in meters [m]. Equation 2.39 produces a maximum of 11% error compared to experiments by Kuroda *et al.* over $Re = 50-700$.

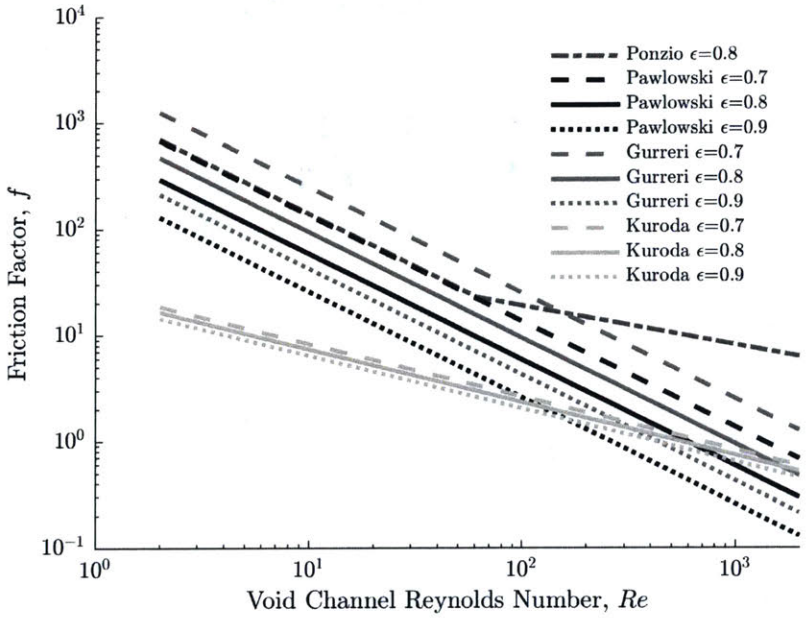

Figure 2-6: Calculated friction factors from models by four different authors, used to predict the pressure drop in a spacer filled channel at void fractions of 0.7, 0.8, and 0.9. Kuroda *et al.* shows less dependence on void fraction than the other models.

Comparison of model friction factors

Figure 2-6 shows the relationship between the four friction factor correlations. Each correlation is shown at 3 different void fractions (ϵ=0.7, 0.8, and 0.9) except for Ponzio *et al.*, which was only available for a single void fraction. All friction factors can be used directly in Eq. 2.28 to calculate pressure drop.

For the models proposed by Ponzio *et al.*, Gurreri *et al.*, and Pawlowski *et al.*, the friction factor depends only on the void fraction and Re. The results vary by a factor of three for Re <100 and the difference increases with increasing Re. This indicates that the pressure drop prediction could vary by a factor of three or more depending on the model used.

The friction factor developed from Kuroda *et al.*'s work (Eq. 2.39) depends on the void fraction, Re, and spacer geometry. The result shown in Fig. 2-6 assumes h=h_{sp}=$2d_f$=1

mm. The filament pitch l_f can be calculated from these values and the void fraction (Eq. 2.31). While the result shown in Fig. 2-6 is an order of magnitude lower than the other models at low Re, the correlation was developed using experimental results for $Re = 50-700$. At these higher Re, the result is on the same order as the other three models and matches the trend predicted by Ponzio *et al.*. In Section 2.4.3, we evaluate all four models against experimental results.

2.2.8 Energy consumption

The total specific energy consumption, Γ_{total} (J/m^3) related to the ED process is the sum of the energy consumed for desalination and pumping,

$$\Gamma_{\text{total}} = \Gamma_{\text{desal}} + \Gamma_{\text{pump}}. \tag{2.40}$$

The specific energy associated with pumping a solution through each circuit of the ED stack is

$$\Gamma_{\text{pump}} = 2\frac{Q\Delta P}{\eta_{\text{pump}} Q_p}, \tag{2.41}$$

where η_{pump} is the efficiency of the pump, ΔP is the total pressure drop through the circuit, assumed equal for the diluate and concentrate sides if $Q = Q_d = Q_c$, and Q_p is the volumetric rate at which desalinated water is produced. Similarly, the energy consumed for desalination is

$$\Gamma_{\text{desal}} = \frac{E_{\text{total}} I_{\text{total}}}{Q_p}, \tag{2.42}$$

where recall that E_{total} is the total voltage applied to the stack. Since the current I_{total} in a batch system varies with time, Eq. 2.42 changes to

$$\Gamma_{\text{desal}} = \frac{1}{V_d^{\text{tank}}} \int_0^{t_{\text{batch}}} E_{\text{total}} I_{\text{total}} \text{dt}, \tag{2.43}$$

where t_{batch} is the batch duration for a diluate volume of V_d^{tank}.

2.3 Experimental setup and procedures

Model predictions for desalination rate, limiting current density, and pressure drop were evaluated using a bench-scale stack (0.18 m^2 total membrane area) and a commercial-scale test stack (37.1 m^2 total membrane area). The objective was to assess the accuracy of the model over a diverse range of geometries and common membrane and spacer types without explicitly deriving new empirical parameters or conducting prior system characterization. In this section, we describe the apparatus and procedures implemented for the validation exercise.

2.3.1 Bench-scale system

The bench scale system comprised a PCA GmbH 64-002, 14 cell pair ED stack of 8 cm x 8 cm active area ion exchange membranes sandwiched between two platinum coated titanium electrodes. Woven polypropylene spacers (thickness 0.35 mm) were placed between each membrane forming sheet-flow channels. Appropriate volumes of feed solution (± 0.025 L) were split between diluate and concentrate streams and recirculated through their respective channels and into separate magnetically stirred 1 L glass beakers using two KNF Flodos NF300 KPDC diaphragm pumps. The flow rates through the diluate and concentrate channels were controlled with two King Instrument 7430 Series glass tube flowmeters with valves (± 6%) over flow rates ranging between 0 and 1.7 L/min. A rinse solution was circulated at 2.5 ± 0.1 L/min through the electrode channel between the electrodes and the first CEM membrane on either side of the stack using a separate beaker and an Iwaki

MD-20RZ centrifugal pump.

For desalination and limiting current tests, a Dr. Meter PS-305DM power supply was used to apply a constant voltage of (± 0.1 V) across the electrodes and record current (± 0.01 A). A Hach MP-4 meter was used to monitor diluate and concentrate conductivity (± 2%) at 1 minute intervals. Batch desalination tests were terminated when the target conductivity, related to the target concentration in mg/L using Eq. 2.3, was achieved. Pressure drop through the concentrate and diluate circuits was measured using two Ashcroft 595-04 pressure gauges (±3 kPa).

2.3.2 Commercial-scale system

The commercial-scale ED test stack comprised 56 cell pairs of 168 cm x 19.7 cm active area GE Water ion exchange membranes sandwiched between two platinum coated titanium electrodes. MkIV-2 type spacers (thickness 0.71 mm) were placed between each membrane, forming U-shaped channels. Appropriate volumes of feed solution (± 10 L) were split between diluate and concentrate streams and recirculated through their respective channels and into separate water tanks using two Flotec FP5172 pumps. Water leaving the diluate tank was divided between the diluate channels and the electrode rinse stream. A vertical pipe was inserted into both the diluate and concentrate tanks such that the solution leaving the stack would re-enter the tank in the middle of the volume to facilitate mixing and minimize concentration gradients within the tank. A Keysight N8760A DC power supply was used to apply a constant voltage across the electrodes and measure current (± 0.1%).

Two Omega FP1406 flow meters and four Omega PX309 pressure gauges were used to monitor the flow rate (± 0.2 L/min) and pressure drop (± 2%) in the diluate and concentrate channels at the entry (flow and pressure) and exit (pressure) of the stack. Conductivity Instruments CDCE-90 in-line conductivity probes interfacing with CDCN-91 conductivity controllers were used to monitor conductivity (± 2%) immediately before entering and exiting the stack. Probes measuring the diluate conductivity ($C^b_{d,0}$ and $C^b_{d,Y}$) had cell constants

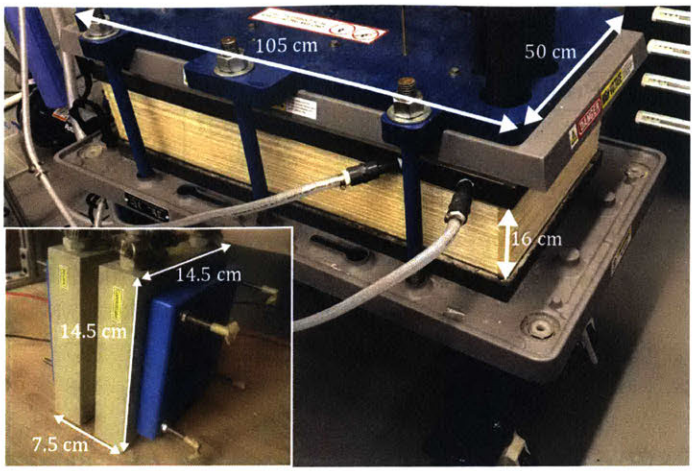

Figure 2-7: Photos of the commercial-scale and bench-scale (lower left) ED stacks used in tests A-F (Table 2.4) with overall stack dimensions for sense of scale.

of K=1/cm and K=0.1/cm, respectively. Probes measuring the concentrate conductivity ($C^b_{c,0}$ and $C^b_{c,Y}$) had cell constants of K=10/cm. All sensors interfaced with National Instruments NI9203 or NI9205 data acquisition modules. The flow rate over each electrode was held at 5.7 $\pm$ 0.2 L/min, while the flow in the diluate channels varied with each experiment.

Batch desalination tests were terminated when the target conductivity, related to the target concentration in mg/L using Eq. 2.3, was achieved. All measured values were sampled at 1 Hz, and Q_d and Q_c were maintained at the same flow rate. For the pressure drop experiments, the flow rate was varied between 0 and 40 L/min using a butterfly valve upstream of the flow and pressure sensors.

2.3.3 Membrane and spacer properties

Values for all stack and global parameters used as model inputs are given in Tables 2.2 and 2.3, respectively. All membrane properties were taken from manufacturer data sheets [28, 29, 30], with the exception of the diffusion coefficients, and the membrane resistances for the bench-scale stack since the solution concentration at which the membranes were

Table 2.2: Stack Parameters

Stack Properties	**Lab**	**Commercial**
Supplier	PCA GmbH	GE Water
Model	64-002	MkIV-2
Number of Cell Pairs	14	56
Membrane Properties		
AEM Model	PC-SA	AR204SZRA
CEM Model	PC-SK	CR67HMR
Flow Path Width (cm)	8	19.7
Flow Path Length (cm)	8	168
AEM Resistance (Ω cm^2)	29	7
CEM Resistance (Ω cm^2)	24	10
Spacer Properties		
Void Fraction	0.60 $\pm$ 0.04	0.83 $\pm$ 0.03
Area Porosity	0.62 $\pm$ 0.04	0.70 $\pm$ 0.02
Spacer Thickness (mm)	0.35 $\pm$ 0.01	0.71 $\pm$ 0.01

tested was not provided. Therefore, we used resistance values which were experimentally determined at brackish water concentrations by Ortiz *et al.* [2], for different ion exchange membranes (Neosepta, Tokuyama), which were however of similar thickness and polymeric form to those used in this study. Likewise, membrane diffusion coefficients, were taken from the experimental work of Amang *et al.*, which were also derived for Neosepta membranes. Spacer thicknesses were measured using a caliper ($\pm$0.01 mm) and area porosity was measured using a scaled photograph of the spacer mesh weave. The volume of the mesh was found by displacing water in a graduated cylinder ($\pm$0.05 mL), from which the void fraction could be calculated. Photos of both experimental stacks are shown in Fig. 2-7.

The number of channel segments Y was selected by running simulations with an increasing number of segments until the value of the predicted current changed by less than 2% with the addition of another segment. Model predictions for the commercial-scale stack utilized a 10-segment discretization, a result further explored in Section 2.5.3.

Table 2.3: Global Modeling Parameters

Parameter	Value	Ref
F (C/mol)	96485	
D^{AEM} (m^2/s)	3.28×10^{-11}	[31]
D^{CEM} (m^2/s)	3.28×10^{-11}	[31]
D_{aq} (m^2/s)	1.6×10^{-9}	[24]
t_+	0.39	[23]
t_-	0.61	[23]
z	1	
ϕ	1	

2.3.4 Feed and rinse solutions

Feed and rinse solutions for the bench-scale stack were prepared using deionized water and the appropriate amount of reagent grade NaCl or Na_2SO_4 (0.2 M $\pm$ 3%). Feed solutions for the commercial-scale stack (also used for rinse streams) were prepared by adding reagent grade NaCl to Cambridge city tap water (Massachusetts, USA) in place of deionized water due to the large volume needed. In the year prior to testing (January-December 2016) Cambridge city tap water contained a maximum TDS level of 370 mg/L, approximately 86% of which was comprised of Na^+ and Cl^- ions. We thus approximate the prepared solution as pure NaCl. The total feed volume was prepared at once, recirculating for 30 minutes at a flow rate of 30 L/min to ensure mixing. The solution was then separated into the diluate and concentrate tanks at the start of each test.

2.3.5 Limiting current density experiments

The limiting current was measured following a common procedure outlined by other authors [7, 8, 9]. The current was measured for 0–100 V in increments of 4 V (for the bench-scale stack) or 2 V (for the commercial-scale stack) while circulating a solution of constant concentration through both the diluate and concentrate channels at three different flow

rates. The resulting current vs. voltage plot can be divided into two regions which are differentiated by slope: a region under-limiting current and a region over-limiting current. The two slopes intersect at the measured limiting current. The limiting current I_{lim} is related to the limiting current density i_{lim} via Eq. 2.2. This method is demonstrated in Section 2.4.1.

2.3.6 Desalination rate experiments

To validate the mass-transfer (Section 2.2.3) and electrical (Section 2.2.2) models, both the bench-scale and commercial-scale systems were operated in constant voltage, batch recirculation mode over the conditions shown in Table 2.4. Bench-scale stack tests were replicated and both test results are shown. Commercial-scale stack tests were performed once due to the extended setup time required to prepare large batches of NaCl solution.

2.3.7 Entrance pressure drop experiments

Along with measuring the total pressure drop across the full commercial stack, we also conducted an experiment to isolate the pressure drop contribution associated with the entrance flow into its channels. The results were compared to the pressure drop predicted by the channel models presented in Section 2.2.7, and used to estimate the relative contribution of entrance effects to the total pressure drop.

For this experiment, the entrance sections from several MkIV-2 U-shaped flow-spacers (Fig. 2-8(i)) were trimmed to isolate the feed port and initial expansion into the channel (Fig. 2-8(ii)). A set of trimmed spacers were sandwiched between two 1 cm thick aluminum end plates, with membranes spaced between them. An adapter, machined from Delrin, was added at the inlet of this assembly to receive flow from a horizontal 5.1 cm ID (2 inch) PVC pipe (Fig. 2-8(iii)). Pressure drop was measured using either 5 spacers or 20 spacers, with all membranes and spacers rinsed between tests using Cambridge city tap water.

Table 2.4: Batch desalination test parameters and results for specific energy and desalination rate. Each bench-scale test (A-C) was run twice. Reported feed and product concentrations were converted from measured conductivity using Eq. 2.3. Note that the batch duration can be calculated from the diluate volumes and desalination rates provided.

	Bench-Scale			Commercial-Scale		
	Test A	**Test B**	**Test C**	**Test D**	**Test E**	**Test F**
Applied voltage [V]	8.0	10.0	11.0	40.0	35.0	25.0
Stack flow rate [L/h]	40	80	70	1860	1260	1260
Feed Concentration [mg/L]	3040 3216	2955 2987	2958 3063	3451	3201	3526
Product Concentration [mg/L]	182 178	99 136	176 195	480	507	395
Concentrate Volume[L]	1	1	0.25	204	204	204
Diluate Volume [L]	1	1	1	757	757	757
Resultant Recovery Ratio	0.5	0.5	0.8	0.8	0.8	0.8
Modeled Desal Specific Energy [kWh/m^3]	0.88 0.97	1.12 1.11	1.26 1.30	1.03	0.83	0.71
Experiment Desal Specific Energy [kWh/m^3]	0.92 ± 0.03 0.82 ± 0.03	0.96 ± 0.04 1.19 ± 0.05	1.13 ± 0.04 1.04 ± 0.05	1.13 ± 0.02	0.87 ± 0.01	0.73 ± 0.01
Modeled Desalination Rate [L/h]	1.88 1.70	2.30 2.44	2.58 2.57	661	522	338
Experiment Desalination Rate [L/h]	1.88 ± 0.05 2.22 ± 0.06	3.00 ± 0.08 3.00 ± 0.08	2.15 ± 0.06 2.22 ± 0.06	650 ± 10	496 ± 7	375 ± 5

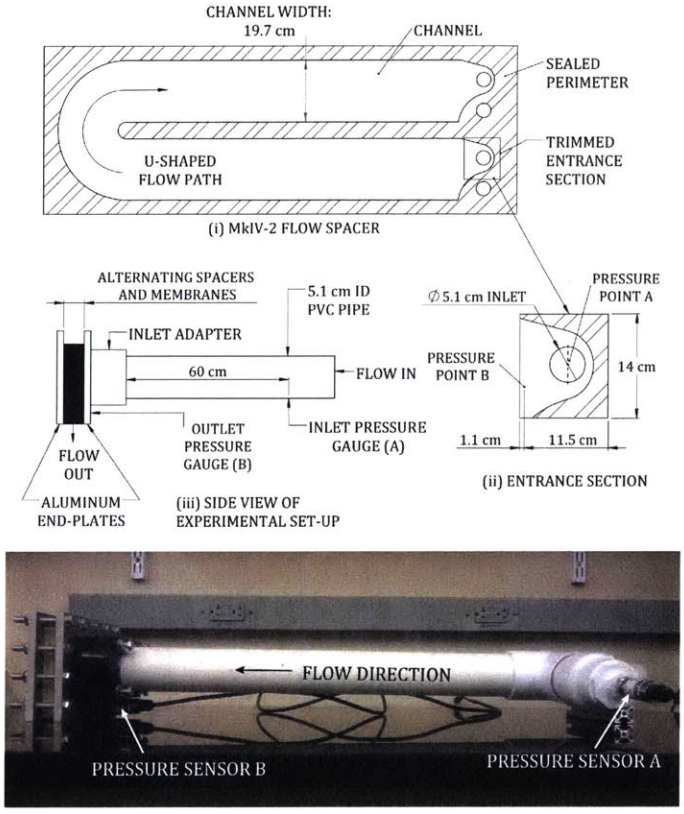

Figure 2-8: Entrance sections of several MKIV-2 flow spacers (i) were cut to isolate the inlet and initial expansion into the channel (ii). Pressure drop was measured for varying flow rates through a set of membranes and entry sections, sandwiched between two aluminum plates (iii), in the experimental apparatus photographed above (iv).

A Flotec FP5172 pump was used to provide between 0.35 and 1.15 L/min of water flow into the stack, controlled manually using a butterfly valve, with flow rate measured at a frequency of 1 Hz upstream of the experimental assembly using an Omega FP1402 sensor ($\pm$ 0.2 L/min). The pressure was also monitored at 1 Hz with Omega PX309 pressure gauges ($\pm$ 2%) at two positions: 60 cm before the stack entrance (Point A), and after the flow has passed through the contraction, at the exit (Point B). The difference between the two pressure measurements was attributed to entrance losses.

2.3.8 Error calculations

For desalination, limiting current density, and pressure drop experiments on the bench-scale stack (including tests A-C), error is reported as the sensor accuracy. Since the measurements were obtained manually, the error associated with sampling frequency is substantial, and therefore is also presented. For corresponding tests on the commercial-scale stack (including tests D-F), error is reported as the quadrature of the sensor accuracy and the 95% confidence interval over 30-60 measurements taken at 1 Hz. When calculated values are reported (specific energy, production rate, current density, linear velocity, and current efficiency), standard error propagation rules have been applied for both systems.

2.4 Results and model validation

In this section we compare model predictions and experimental results for limiting current density, desalination rate, and pressure drop on the bench-scale and commercial-scale stacks.

2.4.1 Limiting current density validation

Fig. 2-9 demonstrates the method of determining limiting current for a 250 mg/L NaCl feed solution at a flow rate of 30 L/h in the bench-scale ED stack. The intercept of the under-limiting curve with the horizontal (voltage) axis also provides an experimentally determined

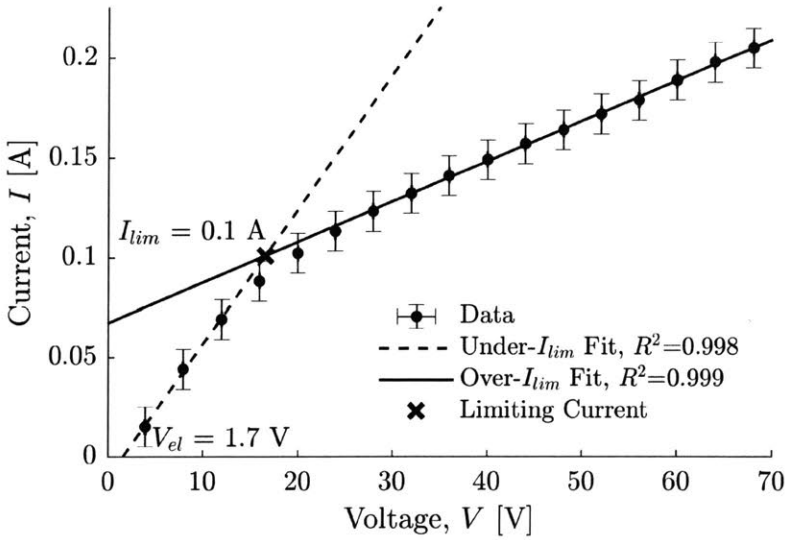

Figure 2-9: Example limiting current test. Measured current I plotted against applied voltage V for a 250 mg/L NaCl solution at a flow rate of 30 L/h in the bench-scale stack. The limiting current I_{lim} is estimated at the intersection of the two distinct linear regions: under-limiting current (dashed line) and over-limiting current (solid line).

electrode potential E_{el} of 1.7 V, which is close to the expected standard cell potential of 1.4 V (described in Section 2.2.2).

Results from the limiting current density tests for the bench-scale and commercial-scale stacks are shown in Figure 2-10. As expected, i_{lim} increases linearly with conductivity (which is proportional to NaCl concentration over the range evaluated) and increases with flow rate (Fig. 2-10). Measurements of i_{lim} matched closely with theoretical predictions for both the bench-scale and commercial-scale stacks, thereby validating the limiting current density model presented in Section 2.2.5 for both stack size scales.

For a given conductivity and flow rate, the measured i_{lim} is significantly lower for the commercial-scale stack (Fig. 2-10b) than the bench-scale stack (Fig. 2-10a). In an ED stack, the actual limiting current density is approached towards the very end of the flow path where diluate concentration is the lowest, while the measured current density is the

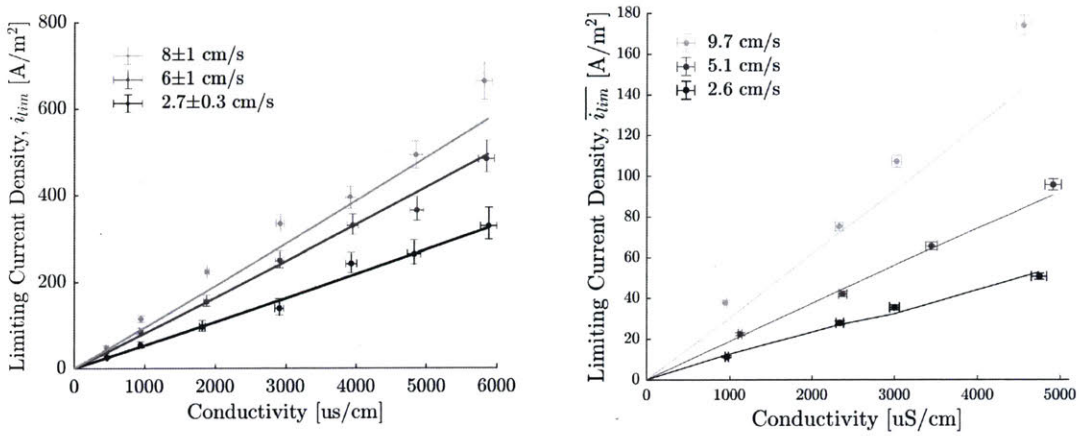

(a) Bench-Scale Stack

(b) Commercial-Scale Stack

Figure 2-10: The limiting current density i_{lim} plotted against the input solution conductivity for varying flow rates, measured using the bench-scale test stack (a) and the commercial-scale test stack (b). Solid lines are model predictions; points are experimental data.

average over the entire flow path. For the bench-scale stack, this difference between the measured (average) current density and actual limiting current density is small because of the short spacer channel length; for the commercial stack, the flow path is long enough for this difference to become measurable, thereby reducing the measured i_{lim} relative to the bench-scale stack.

2.4.2 Desalination rate validation

Figure 2-11 compares the predicted and measured conductivity trajectories across the array of test conditions listed in Table 2.4. Overall, there is good agreement between experimental results and model predictions for both the bench-scale and commercial-scale stack. The desalination rate was 1–23% higher than predicted for tests A and B, and 16–20% lower than predicted for test C using the bench-scale stack. The desalination rate was 2–4% lower than predicted for tests D and E, and 11% higher than predicted for test F using

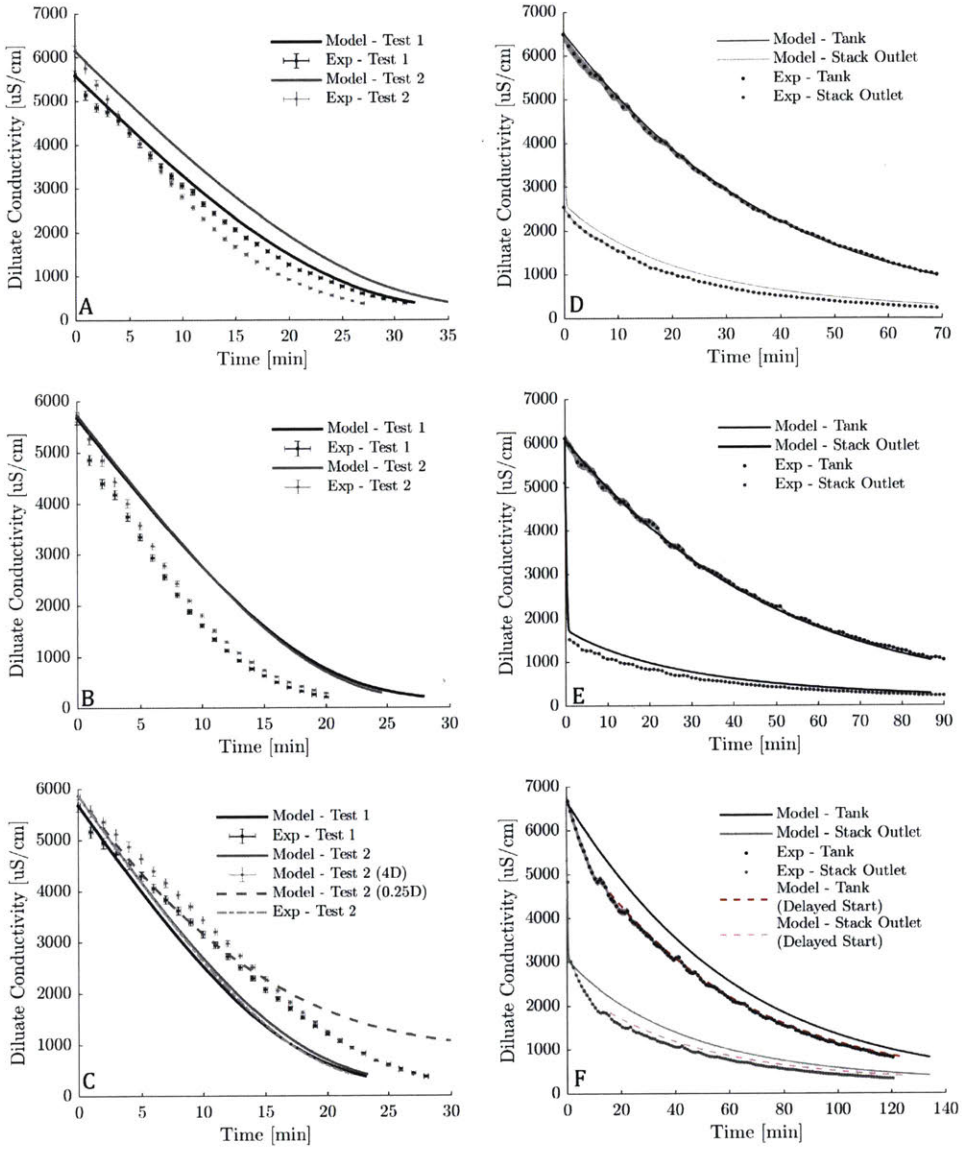

Figure 2-11: Measured and modeled diluate tank conductivity is plotted against time for bench-scale tests (A-C). For the commercial-scale stack (D-F), diluate conductivity within the tank and at the stack outlet are both plotted against time. When test C is modeled with a higher membrane diffusion constant of $4D$, diffusion balances ion migration, and the desired concentration is never achieved (D^{AEM}=D^{CEM}=D). The results for test F are shown with both a standard model start (both tanks at the feed water salinity) and with a delayed model start time shifted by 15 minutes to show how early errors in the model and/or sensing are propagated through the trial.

the commercial-scale stack. The desalination rate could be higher than expected because (1) the measured area porosity is lower than the actual area available for ion transport, as explored in Section 2.5.1; or (2) the modeled membrane resistance was too high, resulting in under-prediction of the current, as explored in Section 2.5.5. While prediction, particularly for the bench-scale test could be improved with further membrane characterization, in general, the model agrees well with the experiments.

2.4.3 Pressure drop validation

Figure 2-12 compares the experimentally measured pressure drop for both stacks to the four models presented in Section 2.2.7. These comparisons use the measured void fraction ϵ=0.83 for the commercial-scale spacer and ϵ=0.60 for the bench-scale spacer, except for the correlation based on Ponzio's data, which is valid only for a single void fraction of ϵ=0.80.

For the overlapped spacer in the commercial stack, all models under-predict the measured pressure drop. While Ponzio's model provides the best alignment in terms of trend and magnitude, it still under-predicts the experimental result by 37% at the manufacturer-recommended linear flow velocity of 7 cm/s.

The bench-scale stack contained a woven spacer. While Gurreri *et al.*'s woven spacer model predicts within an average of 9.4% of the measured pressure drop, ϵ=0.60 falls outside the domain investigated in their work ($0.76 < \epsilon < 0.88$). As described in Section 2.2.7, Eqs. 2.36 and 2.37 are power laws fitted to Gurreri *et. al.*'s data and extrapolation may result in invalid pressure drop predictions. For example, if a linear fit were implemented, then the resulting model would predict a pressure drop that is 36% of the model values plotted in Fig. 2-12.

We also investigated if entrance effects into the channel could account for the observed difference between the channel model predictions and measured pressure drops using the setup described in Section 2.3.7. The results of this test for 5 and 20 spacers is shown in Fig. 2-13. The test confirms that (1) the entrance losses act in parallel with one another,

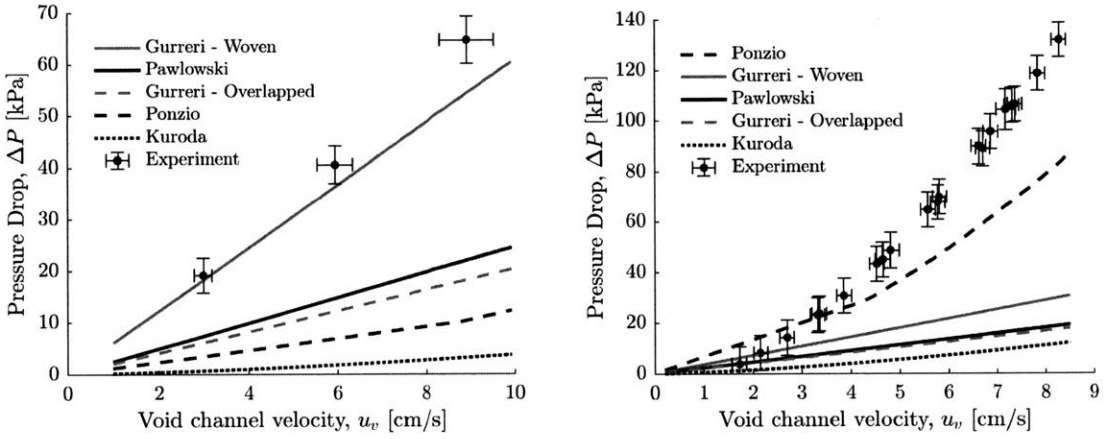

(a) Bench-Scale Stack (ϵ=0.60) (b) Commercial-Scale Stack (ϵ=0.83)

Figure 2-12: Modeled and experimental pressure drop for the bench-scale stack ($\epsilon = 0.60$, left) and for the commercial-scale stack ($\epsilon = 0.83$, right). All four models under predict the experimental values. Gurreri *et al.*'s woven model provides good alignment for the bench-scale test but under-predicts the pressure loss on the commercial-scale stack. Additionally, $\epsilon = 0.60$ is outside of the range over which the model was derived ($0.76 < \epsilon < 0.88$). Ponzio *et al.*'s model provided the closest alignment with the commercial-scale data, but still under-predicted measured values by 37% at the manufacturer recommended flow velocity of 7cm/s.

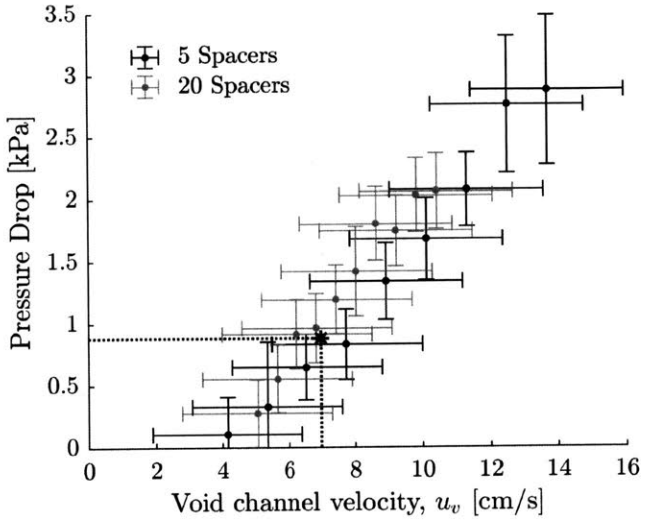

Figure 2-13: Experimental results showing the pressure drop over the inlet only for the spacer used in the commercial-scale tests. The pressure drop for 5 spacers and 20 spacers is approximately the same when the channel velocity is held constant. Dotted lines mark a typical channel velocity for this spacer of 7 cm/s; at this velocity the entrance effect contributes only 0.9 kPa to the total of ≈100 kPa seen for the full stack.

because the same volumetric flow rate per cell Q^{cell} produces the same pressure drop, and (2) the entrance effects account for $< 1\%$ of the total pressure drop for the commercial-scale stack. For example, at a typical channel velocity of 7 cm/s, the entrance effect contributes only 0.9 kPa to the total of ≈100 kPa seen for the full stack (Fig. 2-12b).

Although models were identified that could predict channel pressure drop relatively accurately for the two stacks used in this study (Gurreri *et al.* for the bench-scale stack, and Ponzio *et al.* for the commercial stack), a single model that could be applied for a variety of stack sizes and conditions was not identified. Furthermore, Gurreri *et al.*'s model is highly sensitive to how it is extrapolated for void fractions outside the authors' original work. We caution other researchers against choosing a specific model to predict channel pressure drop, and thus pumping power, for a given stack design; it may be necessary to conduct experiments to fully characterize a spacer's pressure drop behavior. We conclude

that the existing pressure drop models under-predict real channel losses, considering that entrance effects to the channels and other losses associated with inlet and outlet piping to the stack are negligible (2.6).

2.5 Discussion on model sensitivity

In this section we examine the sensitivity of the model predictions to the simplifying approximations presented in Section 4.2. Comparison is performed using the commercial-scale stack because it is more relevant for industrial electrodialysis processes. Model sensitivity was analyzed for test D because the operating void channel linear velocity (6.8 cm/s) most closely matches manufacturer recommendations [32].

2.5.1 Sensitivity to area porosity

Figure 2-14 demonstrates relatively good agreement between model predictions of total current to measured values for test D, with an under-prediction at all conductivities. This small systematic error is achieved without the use of any empirically derived parameters or prior system characterization requirements.

One possible explanation for the under-prediction of current in Fig. 2-14 is the uncertainty in the fractional membrane area available for ion transport, since it could be higher or lower than the open area of the spacer, resulting in a different effective value of ϕ_A. Here we investigate if the measured open-area porosity is a good measure of the actual fractional membrane area available for ion transport.

To test whether the measured porosity is a reasonable approximation, we examined the effect on current predictions if the actual fractional area were $\pm 10\%$ from the measured open-area porosity of the spacer of ϕ_A=0.7. The predicted current changes by very little (Fig. 2-14), thereby indicating that the accuracy is not significantly affected by this approximation. This result is significant because it implies that the open-area porosity of the

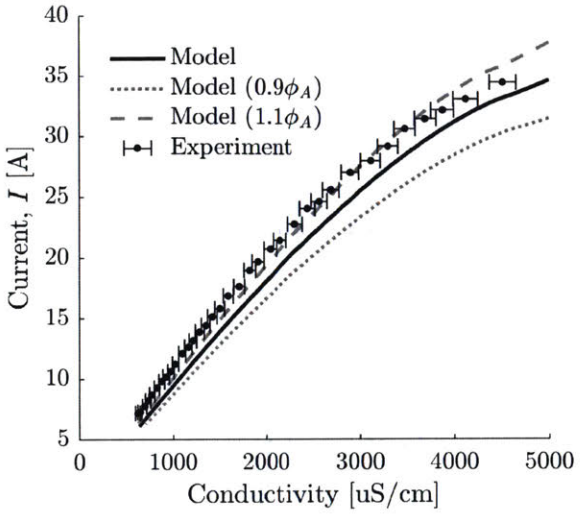

Figure 2-14: Model prediction and measured total current as a function of the average conductivity between the stack inlet and outlet for test D. The gray dashed and dotted lines represent a ±10% sensitivity band on the prescribed area porosity (ϕ_A=0.70). Error in conductivity measurements are shown as horizontal error bars, while error in current measurements is smaller than the plotted dot size.

flow-spacer can be used to estimate the fractional membrane area that will participate in desalination. Furthermore, the area porosity was measured in this study, but it is usually provided by mesh suppliers. Therefore, a designer can avoid additional measurements and use the vendor-specified values to perform initial sizing and current calculations.

2.5.2 Sensitivity to void fraction

While both the mass transfer rate and pressure drop depend on the void fraction, ϵ, the effect on the desalination energetics is not as significant as for pumping. The sensitivity of the pressure drop to void fraction is high, as shown via the friction factor correlations for all models (Fig. 2-6). As an example, consider the effect of the void fraction measurement error (± 0.04, Table 2.2) on the predicted pressure drop for the bench-scale stack, operating at 7 cm/s, and using the best-fit pressure drop model from Fig. 2-12a (Gurreri - Woven).

If ϵ=0.56, the modeled pressure drop would increase by 63%, from 42.6 to 69.3 kPa. If ϵ=0.64, the modeled pressure drop would decrease by 37% to 27.0 kPa. As small errors in void fraction can lead to substantial differences in predicted pressure drop, especially for thin spacers, it is recommended that researchers aim to reduce void fraction measurement error as much as possible and that designers consider realistic manufacturing tolerances. Additionally, the thickness of the sealing edge of the spacer relative to the thickness of the mesh itself, and the applied torque at the tie rods which act to compress the membranes and spacer together, could both affect the actual void fraction.

The void fraction also affects the limiting current density and the mass transfer rate because of the dependence of the mass transfer coefficient k on the spacer-filled channel velocity u_{ch} (Section 2.2.6). The sensitivity in this case is lower than for pressure drop, however, since k primarily affects the concentration at the surface of the membrane, which in turn affects the rate of back diffusion, the boundary layer resistances, and the membrane potential, which are not the dominant impedances in brackish water ED (Sections 2.2.2, 2.5.4, and 2.5.5).

2.5.3 Sensitivity to model discretization

The effect of discretizing the flow-path from 1 to 10 segments on current predictions is examined, and compared to measured values for test D (Fig. 2-15). Use of a single segment ($Y = 1$) under-predicts the initial current by 15.8%, while use of 10 segments ($Y = 10$) under-predicts by only 2.7%. Increasing from 1 segment to 2 segments results in approximately the same improvement, with 1.8x higher computational cost, as increasing from 2 segments to 10 segments, with a compounded 4x increase in computational time. Therefore, as Y increases, it is important to consider the trade-off between improved accuracy and longer computation time (Table 2.5).

Increasing the number of discretizations is important when modeling stacks with long flow paths, such as the commercial-scale stack. Here, the assumption that the entire channel

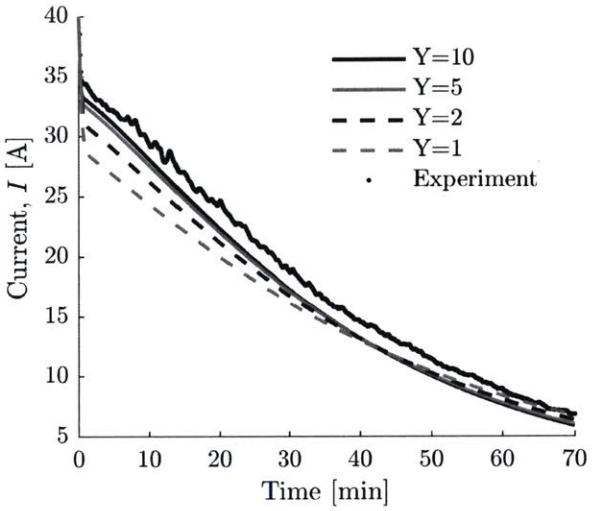

Figure 2-15: Model predictions and measured values of total current for test D. The effect of segmenting the stack into Y=1, 2, 5, and 10 segments is shown. With fewer segments, the model under-predicts the total current. Error on the current measurement is smaller than the dots shown.

is well mixed becomes less accurate. With shorter flow paths, such as the bench-scale stack, discretization is less important. For example, increasing from 1 to 20 segments in test A produced a difference of only 5% in predicted desalination rate.

Table 2.5: Computation time for Y = 2, 5 and 10 segments, relative to computation time if a single segment (Y=1) is used for test D for the commercial-scale stack.

Number of Segments, Y	**Relative Computation Time**
1	1.0
2	1.8
5	4.1
10	7.7

2.5.4 Sensitivity to membrane diffusion

Current efficiency is the ratio of the net rate of ion transfer to the expected rate, given a current.

$$\eta = \frac{(C_{d,0} - C_{d,Y})Q_d^{\text{cell}}F}{I_{\text{total}}} \tag{2.44}$$

Current efficiency may be less than 1.0 because of several factors. Back diffusion of ions from the concentrate to the diluate may be non-negligible (Eqs. 2.14 and 2.15), particularly when $C_c >> C_d$ such as at the end of a batch or near the stack outlet. Current leakage can also occur through a path parallel to the active channel area, if the membrane stack is not electrically insulated adequately.

A comparison of modeled and experimental current efficiency (Fig. 2-16) shows good agreement. At the start of the test, when back diffusion is negligible, current efficiency is approximately 1.0, making it reasonable to assume that current leakage is also negligible for the stack tested. Strong alignment towards the end of the batch also suggests that values assumed for the membrane diffusion coefficients (D^{AEM}=D^{CEM}=D) are reasonable.

Sensitivity to the membrane diffusion coefficient on current efficiency was modeled by increasing and decreasing the membrane diffusion coefficient by a factor of four: $4D$ and $0.25D$ (Fig. 2-16). In both cases, the predicted current efficiency deviated significantly from the measured values, particularly at the end of the batch where the difference between the diluate and concentrate concentrations is the largest. For example, a membrane coefficient of $4D$ under-predicts the current efficiency (and thus the quantity of salt removed) by 34% at this point. Note that $4D$ represents an extreme case where, for example in test C (Fig. 2-11), the model predicts that the desired concentration would never be achieved.

2.5.5 Sensitivity to membrane and boundary layer resistances

The total electrical resistance of the stack is made up of membrane, bulk, and boundary layer resistances as described in Eq. 2.4. The modeled contribution of each resistance in the first

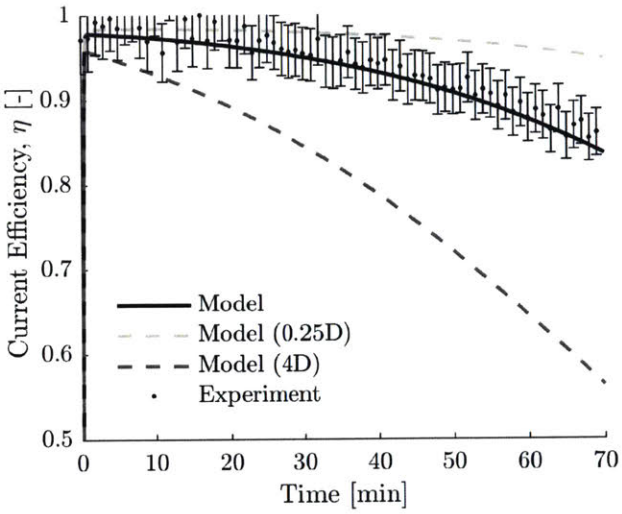

Figure 2-16: Model and experimental results for current efficiency vs. time for test D. The results are shown with the model sensitivity to the membrane diffusion coefficient, $D^{AEM} = D^{CEM} = D$.

and last segment of the stack during test D is shown in Fig. 2-17. The contribution of the resistance from the boundary layer in the concentrate channel was negligible and therefore omitted from the figure. While both the membranes and the bulk diluate resistance are important in the first segment, the bulk diluate resistance always provides the largest contribution in the last segment, accounting for more than 50% of the resistance after 10 minutes, and 89% at the conclusion of the batch. This relative importance would continue to increase if the batch were desalinated to even lower salinity.

As discussed in Section 2.2.2, the membrane resistance has been shown to change with the concentration on either side of the membrane. Specifically, Długołęcki *et al.* found that the resistance of the membrane varied inversely with the solution conductivity [20]. The resistance of the membranes used in the commercial-scale tests was characterized by the manufacturer using a 0.01 M solution. In Fig. 2-17 a diluate concentration of 0.01 M is achieved at approximately 50 minutes, at which point the membrane resistance is a small percentage of the total resistance. Using the relationship observed by Długołęcki *et al.*, a

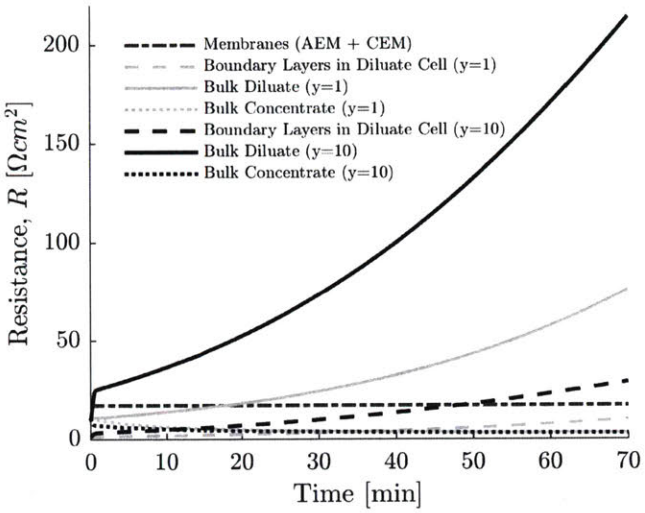

Figure 2-17: The modeled individual resistances for a single cell pair in first segment ($y = 1$) and final segment ($y = Y = 10$) during test D.

static resistance over-predicts the actual resistance at all times prior to this point and helps explain the discrepancy between experimental and modeled conductivity observed in all tests (Fig. 2-11). If the modeled static resistance is too high at the beginning of the trial, it results in lower applied current, and fewer ions are removed, resulting in lower initial desalination rates than measured. Because the experiment is operated in batch mode, that error propagates throughout the entire test.

2.5.6 Sensitivity to water transport

Water transport across the membranes due to osmosis and electro-osmosis was not included in the model validation results presented in this study. Experiments on the commercial-scale stack did reveal a volume increase in the brine tank and corresponding volume decrease in the diluate tank during all tests. The model was rerun including water transport for test D per Eqns. 2.20 and 2.21. The predicted increase in brine volume was 14 L while the experimentally observed increase was 19 $\pm$ 3 L. The difference in specific energy consump-

tion between the model results without water transport (1.03 kWh/m^3) and with water transport (1.04 kWh/m^3) is approximately 0.01% and thus negligible, consistent with the original assumption. It should be noted, however, that at high recoveries, water transport could constitute a non-negligible effect on the total brine volume (which needs to be disposed of properly and thus affects system cost). For example, the 19 L of additional brine due to water transport in test D constitutes an increase of 9% from the original volume and reduces the overall water recovery by 2%.

2.5.7 Validity for multi-ion solutions

The model presented in this work considers a single 1-1 electrolyte comprised only of NaCl, following the practice used in previously published ED models. This assumption is the basis for selecting the Onsager/Falkenhagen equation to translate conductivity to molar concentration and for selecting all diffusion coefficients and transport numbers. Real brackish groundwater contains multiple ions and exhibits a more complicated relationship between conductivity and molarity than for NaCl alone [18]. To explore the implications of this simplification, we conducted a test of the GE commercial-scale stack using real groundwater from a well in Chelluru, India.

Feed water composition was measured by a private laboratory in India with National Accreditation Board Laboratory (NABL) certification (Care Labs, Hyderabad, India), and is given in Table 2.6. Concentrations of Na^+, Mg^{2+}, Ca^{2+}, Cl^-, Alkalinity, TDS, and conductivity were measured following APHA procedures 3500-Na-B, 3500-Mg-B, 3500-Ca-B, 4500-Cl-B, 2320-B, 2540-C, and 2510-B, respectively [33], and SO_4^{2-} following IS:3025(Pt-24) [34]. Errors were estimated following [33],[35], and [36]. The laboratory measured total TDS and conductivity of the feed water was used to calculate a conversion factor of 0.6, used in all subsequent conversions.

A commercial ED stack of the same configuration as the commercial-scale stack used in tests D-F was tested in Chelluru, with all parameters held at the same values presented

Table 2.6: Concentration of major constituents in the raw water used for the test in Figs. 2-18 and 2-19. The final column shows the molar mass to charge ratio (M/z) for each constituent, where the ratio for CO_3^{2-} is shown in the alkalinity row.

Parameter	**Value**	**M/z**
Na^+ [mg/L]	142±25	23
Mg^{2+} [mg/L]	66.8±6.3	12
Ca^{2+} [mg/L]	230±22	20
Cl^- [mg/L]	382±37	35
SO_4^{2-} [mg/L]	72.4±6.6	48
Alkalinity (HCO_3^-) as $CaCO_3$ [mg/L]	648±56	30
TDS [mg/L]	1490±103	
Conductivity [uS/cm]	2480±55	

in Tables 2.2 and 2.3. A locally sourced power supply was used to apply 40 ± 1 V at the electrodes. Current was measured at 1 Hz using a CR Magnetics CR5210-30 DC current transducer (1% accuracy). Temperature was between 27 and 28^{0}C. For this test, the stack produced 500 liters of 300 mg/L TDS water, at recovery of 40%. The average flow rate through the stack was 27.6 L/min.

Figures 2-18 and 2-19 show the model and experimental results from a single trial, while Fig. 2-20 shows the averaged results for 11 trials completed over 2 days. The model specific energy and production rate results (0.31 kWh/m^3, 0.85 m^3/h) matched the experimental results (0.39 kWh/m^3, 0.71 m^3/h) well for the multi-ion feed. This is primarily because the molar mass to charge ratio for the divalent positive and negative ions is on the same order as for Na^+ and Cl^-, respectively (Table 2.6). Because of this, the movement of ions due to migration is also on the same order (Eq. 2.14 and 2.15).

Figure 2-20 shows that at any given diluate tank concentration, the predicted conductivity is higher than the measured conductivity. This results in a predicted resistance that is lower than the actual resistance, and predicted current that is higher than the measured current, explaining the higher production rate predicted by the model (Fig. 2-18). Should

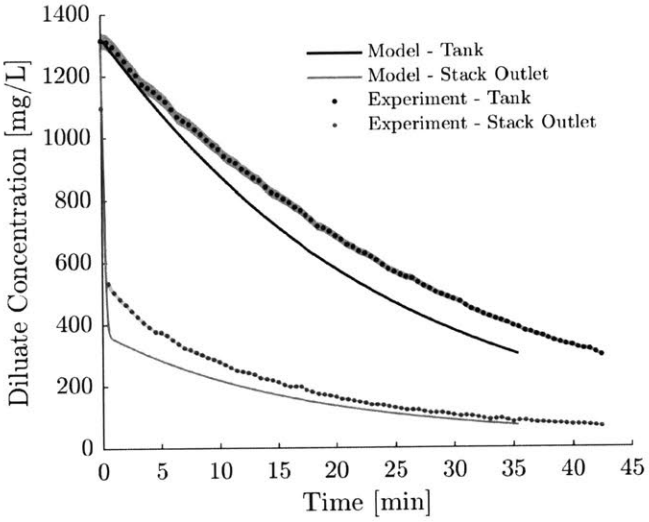

Figure 2-18: Modeled and experimental diluate tank concentration and stack outlet concentration vs. time for the test using real groundwater (Table 2.6). Model is given as concentration in mg/L of NaCl. Experiment as concentration in mg/L of the multi-ion solution, using a conversion 0.6 $\times$ Conductivity (uS/cm) = Concentration (mg/L). Experimental error is shown as a gray band around the data points.

a more accurate prediction of production rate and specific energy be required, conductivity and membrane transfer number models that account for the presence of multiple ions should be used.

2.6 Conclusions

This chapter presents a robust model of brackish water electrodialysis (ED) that predicts desalination rates, current, limiting current density, and energy consumption. The model was experimentally validated at two diverse stack size scales (0.18 vs. 37.1 m^2 total membrane area), spacer thicknesses (0.35 vs. 0.71 mm), spacer types (woven vs. overlapped), as well as in two diverse feed waters (NaCl vs. real brackish groundwater). The measured desalination rate was within 5-25% and 2-11%, and the measured energy consumption was

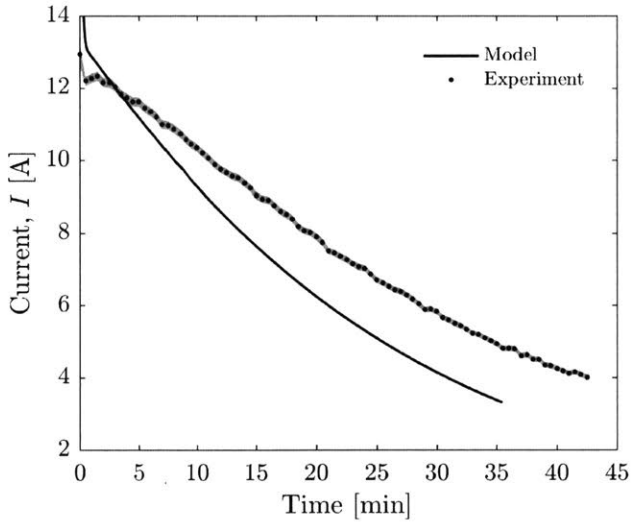

Figure 2-19: Modeled and experimental total applied current vs. time for the test using real groundwater. (Table 2.6). Experimental error is shown as a gray band around the data points.

within 1-23% and 1-9%, of predicted values for the lab-scale and commercial-scale stacks, respectively. This agreement indicates that the mass transport behavior of both stacks was captured with reasonable accuracy. To our knowledge, the theory presented herein is the first robust model of ED systems that does not require any experimental parameter estimation or system characterization.

An objective of this work was to create a full energy consumption model that accounts for both electrochemical and hydraulic contributions. Although power consumption from the ED process was accurately characterized, we were not able to present a single model that reliably predicted pressure drop in the flow channels for both stack sizes and spacer designs. Of the four models for pressure drop that were evaluated, Gurreri *et al.*'s was the most accurate for the lab-scale stack when extrapolated using a power law relationship (predicting within 9.4%), and Ponzio's was the most accurate for the commercial-scale stack (predicting within 37%). These models may be used to approximate required pumping power for the specific stack architectures tested in this study, but they may not be accurate

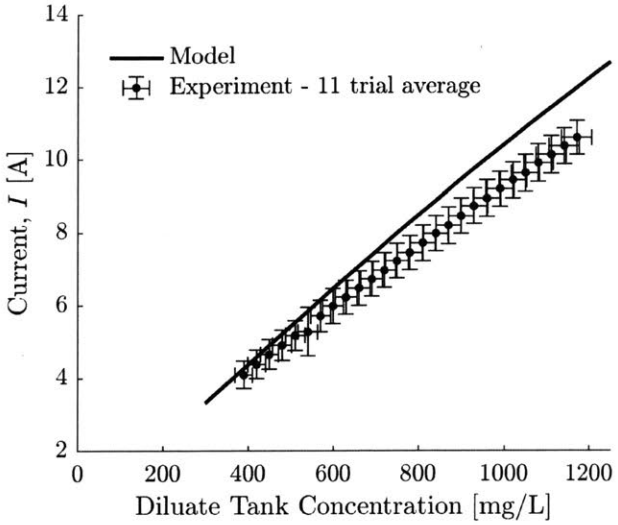

Figure 2-20: Modeled and experimental total applied current vs. concentration, averaged over 11 trials completed over two days. (Table 2.6).

for alternate stack designs and spacer configurations. Pressure drop and pumping power characterization for ED stacks should be an ongoing area of research. At present, we encourage researchers and ED stack designers to conduct experiments to measure channel spacer pressure drop to form an accurate prediction of required pumping power.

The accuracy of the presented ED model was found to be insensitive to several practical simplifications and assumptions capable of reducing computation time and making the model more amenable to design optimization. These included neglecting water transport, treating the membranes as perfectly ion-selective with static electrical resistances, neglecting the resistance contributions from the concentration boundary layers within the channels, and using the open-area porosity of the spacers to estimate the fractional area available for ion-transport. Experimental data collected from an active pilot ED water treatment plant in Chelluru, India demonstrated the robustness of modeling actual brackish groundwater with multiple charged ions as a pure NaCl solution with an equivalent concentration; predictions of desalination rate and specific energy consumption for real groundwater were

found to be accurate within 20 and 22%, respectively.

The theory presented in this work constitutes a powerful tool for electrodialysis researchers and system designers. Its novelty is in providing a fully parametric description of system behavior, enabling desalination rate and power consumption to be quantitatively predicted before an ED system is built. The theory is agnostic to specific size scales and designs, facilitating the exploration of new ED stack architectures and their optimization.

Notation

Roman Symbols

a	Onsager/Falkenhagen constant
B	Onsager/Falkenhagen constant
B_1	Onsager/Falkenhagen constant
B_2	Onsager/Falkenhagen constant
C	molar concentration (mol/m^3)
C^b	bulk concentration (mol/m^3)
C_d	diluate concentration (mol/m^3)
C_c	concentrate concentration (mol/m^3)
C^{AEM}	concentration at surface of AEM (mol/m^3)
C^{CEM}	concentration at surface of CEM (mol/m^3)
d_f	filament diameter (m)
d_h	hydraulic diameter (m)
D^{AEM}	diffusion coefficient of NaCl in AEM (m^2/s)
D^{CEM}	diffusion coefficient of NaCl in CEM (m^2/s)
D_{aq}	diffusion coefficient of aqueous solution (m^2/s)
E_{total}	total applied voltage (V)
E_{el}	electrode potential (V)
E^{mem}	membrane potential (V)
E^{AEM}	membrane potential, across AEM (V)
E^{CEM}	membrane potential, across CEM (V)
f	Darcy friction factor (-)
F	Faraday constant (C/mol)
g	gap between mesh spacer and membrane (m)
h	channel gap (m)
h_{sp}	channel thickness (m)
i_y	current density in segment y (A/m^2)
i_{lim}	limiting current density (A/m^2)
I_{total}	total instantaneous current (A)
k	mass transfer coefficient (m/s)
l_f	filament pitch (m)

l^{AEM}	AEM membrane thickness (m)
l^{CEM}	CEM membrane thickness (m)
L_w	cell pair membrane water permeability (mol/bar-m^2-s)
L	flow path length (m)
M	molar mass (kg/mol)
N	number of cell pairs (-)
P	pressure (Pa)
Q	flow rate (m^3/s)
R	gas constant (J/mol-K)
R_d^b	area resistance, bulk diluate (Ωm^2)
R_c^b	area resistance, bulk concentrate (Ωm^2)
R^{AEM}	area resistance, AEM (Ωm^2)
R^{CEM}	area resistance, CEM (Ωm^2)
R^{BL}	area resistance, boundary layers (Ωm^2)
t	time (s)
t^{AEM}	transport number, anions in AEM (-)
t^{CEM}	transport number, cations in CEM (-)
t_+	transport number, cations in solution (-)
t_-	transport number, anions in solution (-)
t_w	cell pair water transport number (-)
T	temperature (K)
u_{ch}	spacer-filler channel velocity (m/s)
u_v	void channel velocity (m/s)
V^{cell}	volume in single stack cell/channel
V^{tank}	volume of batch recirculation tank
W	flow path width (m)
y	segment (-)
Y	total number of segments (-)
z	ion charge number (-)

Greek Symbols

γ	activity coefficient (-)
Γ_{total}	total specific energy (J/m^3)
Γ_{desal}	specific energy of desalination (J/m^3)
Γ_{pump}	specific energy of pumping (J/m^3)
δ	boundary layer thickness (m)
ϵ	void fraction (-)
η	current efficiency (-)
η_{pump}	pump efficiency (-)
λ_C	equivalent conductance at concentration C (Scm^2/mol)
λ_0	equivalent conductance at infinite dilution (Scm^2/mol)
μ	viscosity of aqueous solution (Pa-s)
π	osmotic pressure (bar)
ρ_{aq}	density of aqueous solution (kg/m^3)
ϕ_A	area porosity (-)

ϕ current leakage factor (-)

Appendix: Pipe loss calculation

Table 2.7: Major and minor losses in the pipe components between the pressure gauges and the stack spacers.

Major Losses	**Length**	**Friction Factor, f**	**Pressure Drop [kPa]**
5.08 cm diameter pipe	2 m	0.031	0.04
Minor Losses	**Quantity**	**Loss Coefficient, k_L**	**Pressure Drop [kPa]**
Expansion from 2.54 cm diameter pipe to 5.08 cm diameter pipe	1	0.55	0.32
45° bend in 5.08 cm diameter pipe	2	0.4	0.03
90° bend in 5.08 cm diameter pipe	2	1.5	0.11
Contraction from 5.08 cm diameter pipe to 2.54 cm diameter pipe	1	0.4	0.24

In Section 2.4.3 it is stated that the pressure drop over the components between the pressure gauges and the entrance/exit to the stack contributes negligibly to the total loss. These effects were approximated using the Darcy-Weisbach equation for fully developed, steady, incompressible flow in the straight pipe sections (major losses),

$$\Delta P = f \frac{l}{D_{pipe}} \rho \frac{V^2}{2}, \tag{2.45}$$

and standard loss coefficients for the minor losses,

$$\Delta P = \rho k_L \frac{V^2}{2} \tag{2.46}$$

where f is the friction factor, obtained from a Moody chart, l is the pipe length, D_{pipe} is the diameter of the pipe, ρ is the fluid density, V is the relevant fluid velocity, and k_L is the minor loss coefficient associated with the various components.

The pressure drop was calculated over all components in the commercial-scale stack at a

volumetric flow rate of 33 L/min, set to match a stack void channel velocity of 7 cm/s. The resulting major and minor losses are shown in Table 2.7. The total of 0.74 kPa represents less than 1% of the total stack pressure drop.

Bibliography

[1] Mohtada Sadrzadeh, Anita Kaviani, and Toraj Mohammadi. Mathematical Modeling of Desalination By Electrodialysis. In *Tenth International Water Technology Conference*, pages 221–233, Alexandria, Egypt, 2006.

[2] J. M. Ortiz, J. A. Sotoca, E. Expósito, F. Gallud, V. García-García, V. Montiel, and A. Aldaz. Brackish water desalination by electrodialysis: Batch recirculation operation modeling. *Journal of Membrane Science*, 252(1-2):65–75, 2005.

[3] Marcello Fidaleo and Mauro Moresi. Optimal strategy to model the electrodialytic recovery of a strong electrolyte. *Journal of Membrane Science*, 260(1-2):90–111, 2005.

[4] Zahra Zourmand, Farzaneh Faridirad, Norollah Kasiri, and Toraj Mohammadi. Mass transfer modeling of desalination through an electrodialysis cell. *Desalination*, 359:41–51, 2015.

[5] Sylwin Pawlowski, Philippe Sistat, Joäo G. Crespo, and Svetlozar Velizarov. Mass transfer in reverse electrodialysis: Flow entrance effects and diffusion boundary layer thickness. *Journal of Membrane Science*, 471:72–83, 2014.

[6] Hong-Joo Lee, F. Sarfert, H. Strathmann, and Seung-Hyeon Moon. Designing of an electrodialysis desalination plant. *Desalination*, 142:267–286, 2002.

[7] M. S. Isaacson and Ain A. Sonin. Sherwood Number and Friction Factor Correlations for Electrodialysis Systems, with Application to Process Optimization. *Industrial & Engineering Chemistry Process Design and Development*, 15:313–321, 1976.

[8] Sreekumaran Thampy, Girish R. Desale, Vinod K. Shahi, Babubhai S. Makwana, and Pushpito K. Ghosh. Development of hybrid electrodialysis-reverse osmosis domestic desalination unit for high recovery of product water. *Desalination*, 282(1418):104–108, 2011.

[9] B. Van den Bosch P. Lens L. Pinoy E. Brauns, W. De Wilde and M. Empsten. On the experimental verification of an electrodialysis simulation model for optimal stack configuration design through solver software. *Desalination*, 249:1030–1038, 2009.

[10] Sylwin Pawlowski, Joäo G. Crespo, and Svetlozar Velizarov. Pressure drop in reverse electrodialysis: Experimental and modeling studies for stacks with variable number of cell pairs. *Journal of Membrane Science*, 462:96–111, 2014.

[11] Matthias Johannink, Kannan Masilamani, Adel Mhamdi, Sabine Roller, and Wolfgang Marquardt. Predictive pressure drop models for membrane channels with non-woven and woven spacers. *Desalination*, 376:41–54, 2015.

[12] F.N. Ponzio, A. Tamburini, A. Cipollina, G. Micale, and M. Ciofalo. Experimental and computational investigation of heat transfer in channels filled by woven spacers. *International Journal of Heat and Mass Transfer*, 104:163–177, 2017.

[13] L. Gurreri, A. Tamburini, A. Cipollina, G. Micale, and M. Ciofalo. Flow and mass transfer in spacer-filled channels for reverse electrodialysis: a CFD parametrical study. *Journal of Membrane Science*, 497:300–317, 2016.

[14] O. Kuroda, S. Takahashi, and M. Nomura. Characteristics of flow and mass transfer rate in an electrodialyzer compartment including spacer. *Desalination*, 46:225–232, 1983.

[15] Ronan K. McGovern, Syed M. Zubair, and John H. Lienhard V. The cost effectiveness of electrodialysis for diverse salinity applications. *Desalination*, 348:57–65, 2014.

[16] Karim M. Chehayeb, Daniel M. Farhat, Kishor G. Nayar, and John H. Lienhard V. Optimal design and operation of electrodialysis for brackish-water desalination and for high-salinity brine concentration. *Desalination*, 420:167–182, 2017.

[17] G. Kortum. *Treatise on Electrochemistry.* Elsevier Publishing Company, 1965.

[18] A. De Diego, A. Usobiaga, and J. M. Madariaga. Critical comparison among equations derived from the Falkenhagen model to fit conductimetric data of concentrated electrolyte solutions. 446:177–187, 1998.

[19] M. Postler. Conductance of concentrated aqueous solutions of electrolytes. I: Strong uni-univalent electrolytes. *Collection of Czechoslovak Chemical Communications*, 35:535–544, 1970.

[20] Piotr Długołęcki, Piotr Ogonowski, Sybrand J. Metz, Michel Saakes, Kitty Nijmeijer, and Matthias Wessling. On the resistances of membrane, diffusion boundary layer and double layer in ion exchange membrane transport. *Journal of Membrane Science*, 349(1):369 – 379, 2010.

[21] Ronan K. McGovern, Adam M. Weiner, Lige Sun, Chester G. Chambers, Syed M. Zubair, and John H. Lienhard V. On the cost of electrodialysis for the desalination of high salinity feeds. *Applied Energy*, 136:649–661, December 2014.

[22] R.A. Robinson and R.H. Stokes. *Electrolyte Solutions.* Butterworth & Co., 1970.

[23] R.W. Allgood and A.R. Gordon. The Variation of the Transference Numbers of Sodium Chloride in Aqueous Solution with Temperature. *Journal of Chemical Physics*, 10:124–126, 1942.

[24] R.H. Stokes. The Diffusion Coefficients of Eight Uni-univalent Electrolytes in Aqueous Solution at 25C. *Journal of the American Chemical Society*, 72(5):2243–2247, 1950.

[25] Vitor Geraldes and Maria Diná Afonso. Limiting current density in the electrodialysis of multi-ionic solutions. *Journal of Membrane Science*, 360(1):499 – 508, 2010.

[26] A. R. Da Costa, A. G. Fane, and D. E. Wiley. Spacer characterization and pressure drop modelling in spacer-filled channels for ultrafiltration. *Journal of Membrane Science*, 87:79–98, 1994.

[27] Karim M Chehayeb and John H Lienhard. Entropy generation analysis of electrodialysis Entropy generation analysis of electrodialysis. *Desalination*, 413:184–198, 2017.

[28] PCA GmbH. *PC Cell ED 64 0 02 Technical Description*, 2016.

[29] PCA GmbH. *PCA Ion Exchange Membranes: Technical Data Sheet*, 2016.

[30] GE Power & Water. *Specification for Electrodialysis Ion Exchange Membranes*, 2010.

[31] D. Nwal Amang, S. Alexandrova, and P. Schaetzel. The determination of diffusion coefficients of counter ion in an ion exchange membrane using electrical conductivity measurement. *Electrochimica Acta*, 48(18):2563–2569, 2003.

[32] GE Power & Water. *GE Aquamite EDR Systems, FS1360EN.*

[33] Water Environment Federation American Water Works Association, American Public Health Association. *Standard Methods for the Examination of Water and Wastewater.* Washington DC, 1999.

[34] Bureau of Indian Standards. *IS:3025 Indian Standard Methods of Sampling and Test for Water and Wastewater, Part 24.* New Delhi, 1986.

[35] Central Pollution Control Board. *Guide Manual: Waster and Wastewater Analysis.* Delhi.

[36] Daniel F. Bender. *Comparison of Methods for the Determination of Total Residual Chlorine in Various Sample Matrices, EPA-600/4-78-019.* Cincinnati, Ohio, 1978.

Chapter 3

Cost-Optimal Design and Operation

This study presents the Pareto-optimal design of ED systems running in five different operating modes and targeting a production rate of 1000 L/h, feed concentration of 2000 mg/L and product concentration of 200 mg/L. The five modes cover three flow configurations (batch, continuous, and hybrid) and two methods of applying voltage (constant voltage (CV) and voltage regulated (VR)). Optimal geometries, flow-rates, and applied voltages were explored as to minimize the 10-year total cost and capital cost of the system. The VR hybrid configuration was found to dominate all other operating modes. The baseline VR hybrid design that placed equal importance on total and capital cost had an active membrane width W of 20.9 cm, length L of 19.0 cm, channel gap of 0.30 mm, 386 cell pairs, 10.8 cm/s linear flow velocity, and 0.91 applied volts per cell pair maximum. Transitioning from the optimal CV to optimal VR operation resulted in a TC and CC reduction of 5% and 20%, respectively, while a move from the optimal batch to optimal hybrid resulted in a TC and CC reduction of 10% and 11%, respectively. A reduction of 37% in TC and 47% in CC was achieved when the length, width, and channel gap were allowed to vary, compared to the case when these variables were held constant to match the commercially available Suez ED stack. Sensitivity analysis was performed to explore the change in the optimal

stack design when feed and product water concentrations, production rate, electrode cost, energy cost, and interest rate were changed by ±50% from the baseline case.

3.1 Introduction

This study presents the Pareto-optimal design of ED systems targeting a production rate of 1000 L/h, feed concentration of 2000 mg/L and product concentration of 200 mg/L, which are representative design requirements for small-scale, community-level desalination systems, especially as needed in rural areas of developing countries [1]. The multi-objective study was designed to find the Pareto front defining the trade-off between capital (CC) and 10-year total cost (TC). The total cost (which can be translated to a specific cost given as $\$/m^3$) is often perceived as most critical for industrial scale plants. However, the difficulty in securing loans in rural India, for example, means that TC may have to be sacrificed in order to obtain lower CC.

A number of studies have been published that analyze the optimal design and/or operation of ED systems, each considering a subset of the variables evaluated here. Existing optimization studies focus on either batch operation [2, 3] or continuous operation [4, 5, 6, 7]. Here we compare the Pareto-optimal solution set for the traditional batch and continuous operating modes alongside new modes including (1) voltage regulated (VR) systems in which the maximum voltage that can be applied without exceed limiting current is prescribed and (2) hybrid systems in which the system starts running in batch mode and then transitions to continuous mode. In our study, we also allow the membrane and electrode geometry, linear flow velocity, number of cell pairs, and applied voltage to vary. Some of these variables are held constant in other studies. For example, Lee *et al.*, Tsiakis *et al.*, and Hattenbach *et al.* held the applied current density at a fixed fraction of the limiting current density and did not treat the individual membrane geometry as a variable [8, 4, 9].

With the exception of the work by Shah *et al.*, which focused on home-scale ED sys-

tems producing 9-15 L/h, the optimization studies in the previous paragraph have been performed assuming a large-scale system and a set capital equipment cost, typically scaled as a function of the membrane area. The focus here is on a small system (relative to most municipal plants) producing 1000 L/h. Smaller production rates may allow new design freedoms. For example, because it may be feasible to implement q large number of cell pairs relative to the production rate, we will find that we are able to have significantly smaller individual membrane and electrode dimensions. We also separate cell pair, electrode, and pump capital equipment costs. Through exploration of new operation modes and conditions, along side the stack geometry, we aim to reduce both the CC and TC from current standards.

3.2 Operating Modes Considered

Optimization was completed for five different operating modes which will be further defined in the following subsections:

1. Constant-Voltage (CV) Batch
2. Voltage-Regulated (VR) Batch
3. Constant-Voltage (CV) Hybrid
4. Voltage-Regular (VR) Hybrid
5. Multi-stage Continuous

These five modes cover three different flow configurations (batch, continuous, and hybrid) and two different methods of applying voltage (CV and VR). In all operating modes there are two primary flow circuits, one for the diluate, and the other for the brine. An additional circuit may be required in all operation modes for the electrode rinse stream; however, it is not considered here as it is not expected to significantly affect the optimal operation mode

nor the design of the membranes and spacers. Additionally, new ED carbon electrodes do not require a dedicated rinse circuit [10].

In the descriptions of the operating modes that follow, the ED stack is considered a "black box," meaning that it could contain various numbers of cell pairs, of different membrane lengths and widths, channel gap sizes, etc. We determine the best configuration of the stack for each operating mode in Section 3.6.

3.2.1 Batch Operation

In the beginning of a batch desalination process, two tanks (one diluate recirculation tank and one brine recirculation tank) are filled with feed water at the same concentration (Fig. 3-1). The relative volume of water in the diluate versus the concentrate tanks governs the recovery ratio of the process. A constant voltage is applied at the electrodes of the ED stack and both streams recirculate at the same flow rate (to avoid trans-membrane pressure differentials) until the diluate recirculation tank reaches the desired product water concentration C_p. Both tanks are then emptied, signaling the completion of a single batch. The production rate Q_p is given by the quotient of the volume of water in the diluate tank and the total batch time (fill, desalinate, empty).

3.2.2 Continuous Operation

In a continuous operation scheme, the flow path is designed to achieve the desired concentration reduction in a single pass (Fig. 3-2). As a result, the production rate of the system matches the flow rate in the stack. The brine stream could operate in the same fashion, making a single pass; however this would result in 50% recovery. Instead, the brine stream is recirculated. Unlike in a batch desalination process, however, the brine operates in a feed-and-bleed mode, where water is moved from the feed tank to the brine recirculation tank, and from the outlet of the concentrate side of the stack to waste, at the same rate. In

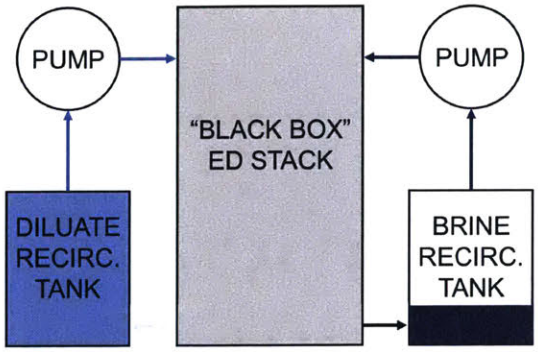

Figure 3-1: In a batch operation scheme, flow is recirculated until the diluate tank concentration reaches the desired product water concentration. The volume of water in the two tanks sets the recovery ratio of the process. The concentration of the diluate stream leaving the stack is always lower than that in the tank. A batch operation could be performed with either constant voltage (CV) or voltage regulation (VR).

doing so, the brine tank maintains a constant concentration. The rate at which this water is moved and the concentration of the tank is determined by the recovery ratio.

3.2.3 Hybrid Operation

The final flow configuration is a hybrid batch-continuous process in which the system operates in batch mode (Fig. 3-1), but only until the concentration of the diluate stream at the stack outlet reaches the target product water concentration. Once this happens, the systems transitions to continuous mode such that the diluate recirculation tank empties by passing through the stack one final time with the voltage still applied. This is distinct from a standard batch operation where the diluate tank itself must achieve the target concentration. Hybrid operation is expected to perform better than standard batch operation because (1) the stack never needs to produce water at a concentration lower than the desired target, and (2) the tank is emptied while desalinating; both conditions stand to increase the desalination rate, given the same stack geometry and operating parameters.

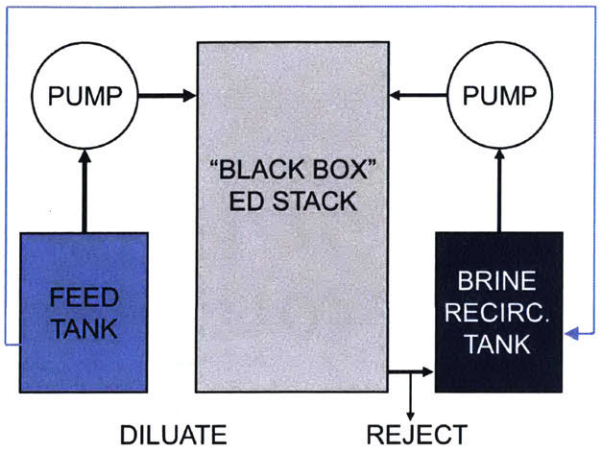

Figure 3-2: In continuous operation scheme, the flow path is designed to achieve the desired concentration reduction in a single pass. The production rate of the system equals the flow rate in the stack. The brine recirculation tank is held at a constant concentration (set by the recovery ratio) by continuously adding feed water and removing concentrate water at the same rate.

3.2.4 Constant-Voltage vs. Voltage-Regulated

Batch and hybrid flow configurations can either be operated with constant voltage (CV) or voltage regulation (VR) at the electrodes. In the constant voltage case, the maximum voltage that can be applied is set by the limiting current at the end of the batch or hybrid run. Previous work in optimizing batch desalination [2] has shown that operating at this maximum voltage is ideal.

Alternatively, we can run the system using voltage-regulation (VR), where a sensor put in the diluate tank controls the maximum voltage that can be applied at any given time without exceeding the instantaneous limiting current density. This idea was described by Shah [11] but not compared to the other operating modes explored here.

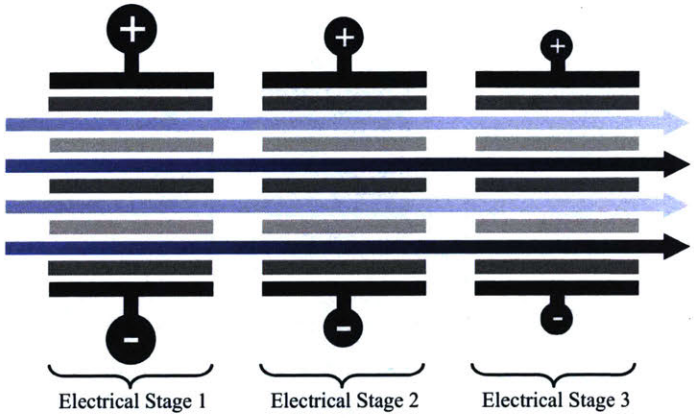

Figure 3-3: An ED system containing three ED stacks in series, each with one hydraulic stage. The applied voltage decreases for each successive stage such that the local applied current density more closely aligns with the local limiting current density.

3.3 Description of Staging Options in Continuous Operation

An individual ED stack or system may contain multiple electrical and hydraulic stages. The number of electrical stages refers to the number of electrode pairs implemented in series in an ED system. Including more than one electrical stage in an ED system allows for independent control of the voltage (and therefore the applied current) at each stage (Fig. 3-3). The voltage applied to each subsequent stage is lower than the one before, allowing the applied current density to better match the local limiting current density, which decreases as the diluate concentration decreases. Implementing electrical staging in this manner decreases the amount of membrane area required to remove a certain amount of salt, in comparison to a system with a single electrical stage.

The number of hydraulic stages refers to the number of passes the water makes along the membranes within a single electrical stage. The goal is to remove more salt with a

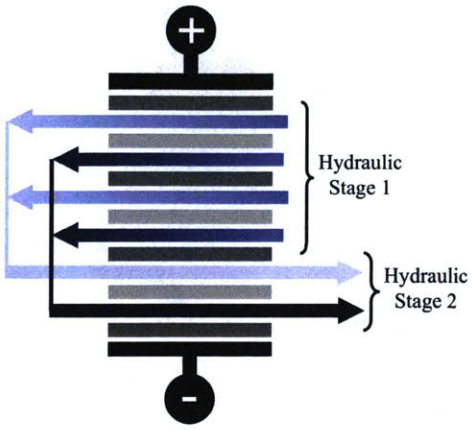

Figure 3-4: An ED system containing one ED stack with two hydraulic stages. Decreasing the number of cell pairs from hydraulic stage 1 to hydraulic stage 2 increases the linear flow velocity, which, for a given concentration, increases the limiting current density and thus the voltage that can be applied at the electrodes.

single pair of electrodes than is feasible with one pass. Figure 3-4 shows a single electrical stage ED stack with two hydraulic stages. Note that the number of cell pairs typically decreases in each subsequent hydraulic stage, which results in a progressively increasing linear flow velocity. Recall from Section 2.2.5, Eq. 2.22, that the limiting current density is a function of the instantaneous and local concentration of the aqueous solution, as well as the linear flow velocity. Incorporating hydraulic stages with decreasing cell pairs (and thus increasing flow velocity) increases the limiting current density at the outlet of the ED stack, as compared to if the number of cell pairs remained constant.

A single ED stack could contain any number of electrical and hydraulic stages. Figure 3-5 shows the Suez Aquamite 3 electrodialysis stack which has two electrical stages in series, and four total hydraulic stages (two per electrical stage). The first and third hydraulic stages contain 50 cell pairs while the second and fourth hydraulic stages contain 35 cell pairs. Note that this stack has the same membrane and electrode area as would an equivalent system with two ED stacks in series, each having one electrical stage and two hydraulic stages. Combining them into one stack as shown here reduces the material required for the frame

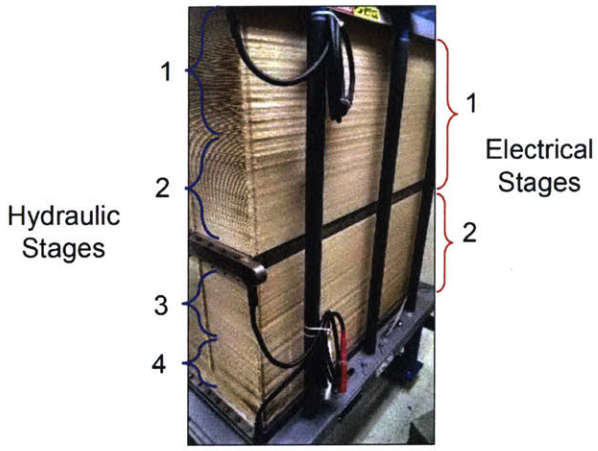

Figure 3-5: The Suez Aquamite 3 ED Stack contains two electrical stages, each with two hydraulic stages.

and piping.

While multiple hydraulic and electrical stage systems will be optimized in Chapter 3, a standard industry design rule states that a single hydraulic stages typically provides 50-67% salt removal [12]. Thus for a feed water concentration of 2000 mg/L, with a desired product water quality of less than 300 mg/L, a first order analysis would suggest that three hydraulic stages would be required (Stage 1: 2000 $\rightarrow$ 1000 mg/L, Stage 2: 1000 $\rightarrow$ 500 mg/L, Stage 3: 500 $\rightarrow$ 250 mg/L).

3.4 Cost Model

This section outlines the cost analysis used to estimate the capital and total 10-year cost of the ED system. Note that the primary goal of this work is to determine the overall trends and trade-offs between different operating modes and geometries. Component costs that are expected to be relatively constant between the different operating modes and geometries are not included. Some examples of such components include: the plant shelter, storage tanks, power connections and wiring, bore well, excavation work, installation charges, reversal

valves and piping, sensors and instrumentation, controls, DC rectifier, operator salary, chemicals, and pre-filters.

3.4.1 Capital Cost

In this analysis the capital cost includes the cost of the ED stacks' membranes, spacers, and electrodes and the cost of the first set of pumps (brine and diluate). Following the industry-standard operating procedure, we assume equal flow-rates (Q) in the diluate and concentrate channels so that the effects of trans-membrane pressure differences could be neglected. With equal flow rates, channel dimensions,and spacer geometry in the diluate and concentrate fluid circuits, the pressure drop over the stack is also equal and the same size pump could be used for both. Capital cost CC is calculated as

$$CC = 2\Upsilon_{\text{pump}} + \sum_{\text{e}=1}^{E} 2LW(N_{\text{e}}\Upsilon_{\text{mem}} + N_{\text{e}}\Upsilon_{\text{sp}} + \Upsilon_{\text{el}}), \tag{3.1}$$

where Υ_{pump} is cost of a single pump (\$), E is the number of electrical stages, N_{e} is the number of cell pairs in the e-th electrical stage, and Υ_{mem}, Υ_{sp}, and Υ_{el} are the membrane, spacer, and electrode costs, respectively (\$/m^2). The component costs are summarized in Table 3.1 and were estimated based on wholesale supplier costs, previous literature, and conversation with an industrial ED stack manufacturer. Note that while this component cost breakdown results in an effective cost of \$100/m^2 cell pair, it is distinct from other optimization papers [13, 4, 8] in which all capital equipment costs are approximated by a lumped cost of \$300/m^2 cell pair. This was done intentionally as we hypothesized that, for the low production rate stacks investigated in this work, separating electrode cost would push the design toward smaller individual membrane sizes in order to minimize electrode area, a trend that would be consistent with previous work on domestic-scale systems [2], and would not be captured in a lumped model. Additionally, separating component costs allowed us to capture the capital cost of the pumps.

Table 3.1: Unit Cost of Stack Components

Component	**Cost**	**Reference**
Electrodes	$\$1200/m^2$	[14, 15, 16]
Membranes	$\$40/m^2$	[17, 15, 16]
Spacers	$\$10/m^2$	[18, 15, 16]

Lubi Pumps is an Indian pump manufacturer and the pump supplier for Tata Project's rural desalination plants. Data sheets and quotes for Lubi Pumps' LCRN vertical multistage centrifugal 316SS pump line were used to develop a pump cost model. Equation 3.2 is the result of linear regression of the pump cost Υ_{pump} as a function of pressure P (kPa) and flow rate Q (m^3/h) at the pump's maximum efficiency point. The data for two pump lines (LCRN10 and LCRN1S) are shown in Fig. 3-6 along with the example model lines at 1, 4, and 7 m^3/h. Note that the cost of the pump is more heavily dependent on the pressure than the flow rate.

$$\Upsilon_{\text{pump}} = 198.10 + 6.06Q + 0.35P \tag{3.2}$$

Similarly, linear regression was used to estimate the peak efficiency of the pump (η_{pump}) as a function of the flow rate Q (m^3/h) using the same pump data base;[1] the result is given as,

$$\eta_{\text{pump}} = 2.24Q + 27.63. \tag{3.3}$$

[1]Note that the peak pump efficiency given on the data sheet was scaled by 0.7 before completing the regression to account for the motor efficiency and the under performance of the pumps noted in field trials.

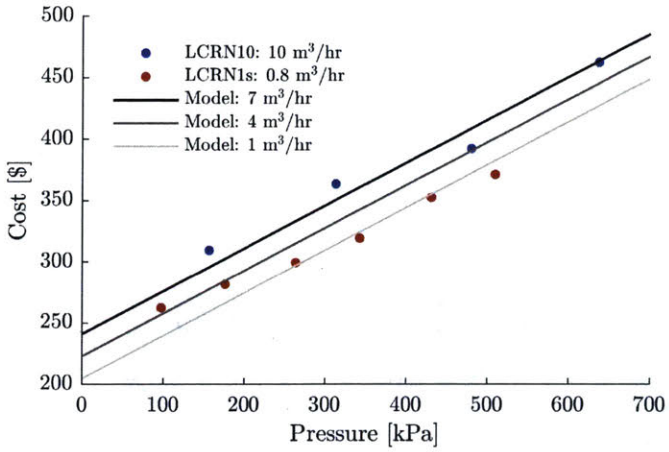

Figure 3-6: Dots are quoted prices for different pumps from Lubi Pumps LCRN1s and LCRN10 pump lines. Specifically, each point represents one of the following pumps: 10-2, 10-4, 10-6, 10-8, 1s-2, 1s-4, 1s-6, 1s-8, 1s-10, and 1s-12. The solid lines are results from the linear regression at three different flow rates. Pump pricing is more heavily dependent on the pressure than the flow rate.

3.4.2 10-Year Total Cost

The 10-year total cost of the system TC is calculated as the sum of the CC, interest $\Upsilon_{\text{interest}}$, replacements pumps, and energy Υ_{energy} as,

$$TC = CC + \Upsilon_{\text{interest}} + 2\Upsilon_{\text{pump}} + \Upsilon_{\text{energy}}, \tag{3.4}$$

where it is assumed one pump replacement is required at year five and the interest is calculated as,

$$\Upsilon_{\text{interest}} = \tau \frac{(CC)\iota(1+\iota)^{\tau}}{(1+\iota)^{\tau} - 1} \tag{3.5}$$

where ι is the interest rate and τ is the loan term in years. Based on the typical loan that is available to entrepreneurs for small-scale desalination in rural India, the interest rate is set to 10% and the loan term 5 years [19]. The total cost of energy over 10 years is

calculated as

$$\Upsilon_{\text{energy}} = V_{\text{total}} \Gamma_{\text{total}} r_E, \tag{3.6}$$

where V_{total} is the total volume of water produced over the assumed product lifetime of 10 years (m^3), Γ_{total} is the is the total specific energy consumption (desalination plus pumping, kWh/m^3), and r_E is the energy rate, approximated as \$0.10/kWh.

3.5 Optimization

The goal of the optimization is to determine the lowest cost ED system operation mode, geometry, and operating conditions given a target of desalination 2000 mg/L feed water to 200 mg/L at a rate of 1000 L/h. As an understanding of the trade-off between capital cost (CC) and 10-year total cost (TC) is desired, the optimization is solved as a multi-objective problem.

3.5.1 Problem Formulation

The problem is formulated using standard optimization notation as

$$\begin{aligned} \underset{x}{\text{minimize}} \quad & \boldsymbol{J}(\boldsymbol{x}, \boldsymbol{p}) \\ \text{subject to} \quad & \boldsymbol{g}(\boldsymbol{x}, \boldsymbol{p}) \leq 0 \\ & \boldsymbol{x_{lb}} \leq \boldsymbol{x} \leq \boldsymbol{x_{ub}}, \end{aligned} \tag{3.7}$$

where $\boldsymbol{x}$ is the design vector to be optimized, $\boldsymbol{p}$ is the vector of constant model parameters, $\boldsymbol{J}(\boldsymbol{x})$ is the vector of objective functions, and $\boldsymbol{g}(\boldsymbol{x})$ contains the inequality constraints. In this study, the design vector is bounded from below and above by $\boldsymbol{x_{lb}}$ and $\boldsymbol{x_{ub}}$, respectively. No equality constraints were imposed in this formulation.

3.5.2 Objective Function

The two objectives that are considered as part of this multi-objective design optimization were to minimize the total 10-year cost (TC) and capital cost (CC), therefore J_1 and J_2 are given by

$$\begin{aligned} J_1 &= TC \\ J_2 &= CC \end{aligned} \tag{3.8}$$

where the calculation of both values is included in Section 3.4.

3.5.3 Variables and Bounds

The design vector $\boldsymbol{x}$ for the batch and hybrid operation modes (both CV and VR) consists of six variables listed in Table 3.2. The maximum bounds for L and W were selected to allow the maximum current commercial flow channel dimensions to be included in the design space. For example the standard Suez Mach IV spacer provides flow channel of dimensions L=168 cm and W=19.7 cm, while Hangzhou Iontech provides L=138 cm and W=34.3 cm. Similarly the bounds for the channel gap, h, were selected to include values of ED stacks designed by PC-Cell (0.3 mm), Suez (0.71 mm), and Hangzhou Iontech (1.0 mm). The maximum number of cell pairs was set to 900 based on the maximum number, at the smallest channel thickness (0.3 mm) that would fulfill constraint g_3 (See Section 3.5.5). Better convergence times were found when the sixth variable, volts per cell pair (V/N) was used instead of voltage directly.

All variables were treated as continuous due to the limitations of the algorithm implementation (See Section 3.5.6). In practice the number of cell-pairs would be rounded up to the closest integer from the value recommended by the optimizer, while increasing the voltage slightly to maintain the same ratio of V/N. The flow rate Q would also likely be adjusted to match the closest nominal flow rate in the available pump line by the manufac-

Table 3.2: Design Variables and Bounds for the Batch and Hybrid Operation Modes

Variable	Symbol	Bounds
Length of Active Area	L	10 - 200 cm
Width of Active Area	W	10 - 100 cm
Channel Gap	h	0.3 - 1.0 mm
Number of Cell Pairs	N	10 - 900
Flow Rate	Q	1,000 - 10,000 L/h
Volts per Cell Pair	V/N	0.2 - 3.0 V

turer. Discrete pumps were not included in the model. Instead, the cost and efficiency of the pump was calculated per Eqs. 3.2 and 3.3.

When moving to a continuous operation mode, the flow rate can be removed as a variable, as Q=1000 L/h in all cases. Optimization for the continuous case was completed with two, three, and four electrical stages having one hydraulic stage each (denoted as 2E-1H, 3E-1H, and 4E-1H, respectively), as well as for two electrical stages having two hydraulic stages in the first electrical stage and either one of two hydraulic stages in the second electrical stage (denoted as 2E-2H-1H and 2E-2H-2H, respectively).

3.5.4 Parameters

Parameters required for the ED simulation model were the same as those for the commercial-scale stack provided in Chapter 2. This includes spacer and membrane properties. The volume porosity was held constant at 0.8, even when the channel gap / spacer thickness changed in order to use Ponzio's pressure drop model for prediction of pressure losses in the flow channels. Parameters required for the cost and energy model were provided in Section 3.4. The remaining parameters are provided in Table 3.3.

The parameters in Table 3.3 and mentioned previously are considered the baseline case in this analysis. In Section 3.7, the optimal operation mode (VR-Hybrid) for the baseline case is analyzed further by testing this operation mode's sensitivity to feed water concentration, product water concentration, interest rate, energy rate, and electrode cost.

Table 3.3: Simulation Parameters for the Baseline Case

Parameter	Value
Feed Concentration	2000 mg/L
Product Concentration	200 mg/L
Recovery Ratio	80%
Production Rate	1000 L/h
Volume Produced	10 m^3/day
System Life	10 years

3.5.5 Constraints

The first two constraints g_1 and g_2 of $\boldsymbol{g}(\boldsymbol{x}, \boldsymbol{p}) = [g_1, g_2, g_3, g_4, g_5] \leq 0$ (Eq. 3.7) apply to all operating modes. The rest of the constraints are defined differently for the batch and hybrid operation modes than for the continuous mode. The first constraint pertaining to all operating modes sets the minimum flow velocity to 6 cm/s, consistent with industry standards [10] as

$$g_1 = 6\,\text{cm/s} - u_{\text{ch}}. \tag{3.9}$$

The second constraint sets the maximum pressure at the inlet of the ED stack to be less than 690 kPa ($\approx 100psi$) :

$$g_2 = P - 690\,\text{kPa} \tag{3.10}$$

The pressure limit of an ED stack is primarily dependent on the gasket material that seals outer perimeter of the spacer. Suez, for example, sets a maximum recommended operating pressure of 50 psi with the current Mach IV spacer [10]. We have doubled that value here to see how a seal redesign that allowed for higher pressures would affect stack design.

Batch and Hybrid Mode Constraints

The first constraint g_3 that pertains only to batch and hybrid operating modes is on the production rate of the system. We are targeting a production rate of 1000 L/h and so set the third constraint to

$$g_3 = 1000\,\text{L/h} - Q_p, \tag{3.11}$$

where Q_p is the production rate of the system, distinct from Q, the flow rate of the diluate and concentrate streams. We found that setting a fourth constraint,

$$g_4 = Q_p - 4000\,\text{L/h}, \tag{3.12}$$

was an effective way to push the solution toward the desired production rate without limiting the feasible design space so much as to affect the rate of convergence. Note that while g_3 and g_4 together do allow the optimizer to produce feasible designs with a production rate anywhere between 1000 and 4000 L/h, lower production rates are always less expensive. All Pareto optimal points were found to lie within 1% of the target production rate (1000 L/h), as desired.

For the CV batch and hybrid operation modes, the final inequality constraint ensures that the design operated over a safety factor-adjusted limiting current density for no more than 5% of the batch period. The duration t_{lim} over which the applied current density exceeded 70% (safety factor) of the instantaneous limiting current density was tracked and the constraint is given by:

$$g_5 = \frac{t_{lim}}{t_{batch}} - 0.05 \tag{3.13}$$

Note that this constraint is not required for the VR batch or hybrid operation modes where the voltage at any time is set such that the system is running at the safety factor-

adjusted limiting current density.

Continuous Mode Constraints

In the batch and hybrid operation modes, we set constraints around the production rate, while the ED simulator model itself was setup to end when the correct dilute concentration was achieved. For the continuous systems, the opposite implementation is used. The production rate is set for all designs by specifying Q=Q_p=1000 L/h and constraints are placed around the product water concentration as:

$$g_3 = 20\,\text{mg/L} - C_p, \tag{3.14}$$

and,

$$g_4 = C_p - 200\,\text{mg/L}, \tag{3.15}$$

where C_p is the product water concentration (final diluate concentration). Note that while g_3 and g_4 together allow the optimizer to produce feasible designs with $20 < C_p < 200$ mg/L, higher product water concentrations are always less expensive, and all Pareto optimal points were found to lie within 2% of the target production rate.

3.5.6 Simulation and Optimizer

The problem described above was solved using a multi-objective genetic algorithm, specifically the modified NSGA-II algorithm [20] implementation in MATLAB [21]. The solution is a set of non-dominated Pareto optimal solutions with respect to the problem objective functions. The difference between the original NSGA-II and the modified version is that the modified version adds an extra tuning parameter, Pareto Fraction (PF $\in$ (0,1)), to control the number of elite members in each population that progress to the next generation. As each run of the NSGA-II will produce a different solution set, since every generation con-

sists of new, randomly generated individuals, it is important to run the simulation multiple times, and to vary the PF over those runs. Each Pareto front presented in this work is the non-dominated solution set following six NSGA-II optimization runs. Three runs were completed using the full bounds in Section 3.5.3, using three different PFs ($0.3 < \text{PF} < 0.6$). These were followed by three additional runs in which the bounds on the design variables were tightened around the optimal design vectors from the first three runs.

Attempts to use traditional gradient based solvers including MATLAB's *fmincon* (SQP and Active-Set) were unsuccessful when implemented over the full bounds of the design variables due to the small portion of the design space that is feasible and the possibility for complex constraint and objective function values when the limiting current density is exceeded, an issue that was particularly problematic for the continuous configurations. It thus became computationally intensive to run a multi-start, multi-objective gradient based optimization, which requires successive changes to the weight placed on each of the two objectives.

3.6 Results and Discussion

In this section, we discuss the cost-optimal designs obtained for the baseline case of desalinating from 2000 mg/L to 200 mg/L using the cost parameters described in Section 3.3. Sensitivity analysis follows in Section 3.7. The Pareto front for each of the five operation modes optimized over all design variables are shown in Fig. 3-7 by the red points. They are plotted together with the Pareto fronts for an optimization in which the active area length, width, and channel gap are held constant at the values of the Suez commercial stack (L=168 cm, W=19.7 cm, h=0.71 mm), marked via the blue points. These Suez Pareto fronts are included as they effectively represent the best case scenario if existing, commercially available membranes, spacers, and electrodes had to be used. They also provide a direct point of comparison for the gains that can be made by selecting a new geometry.

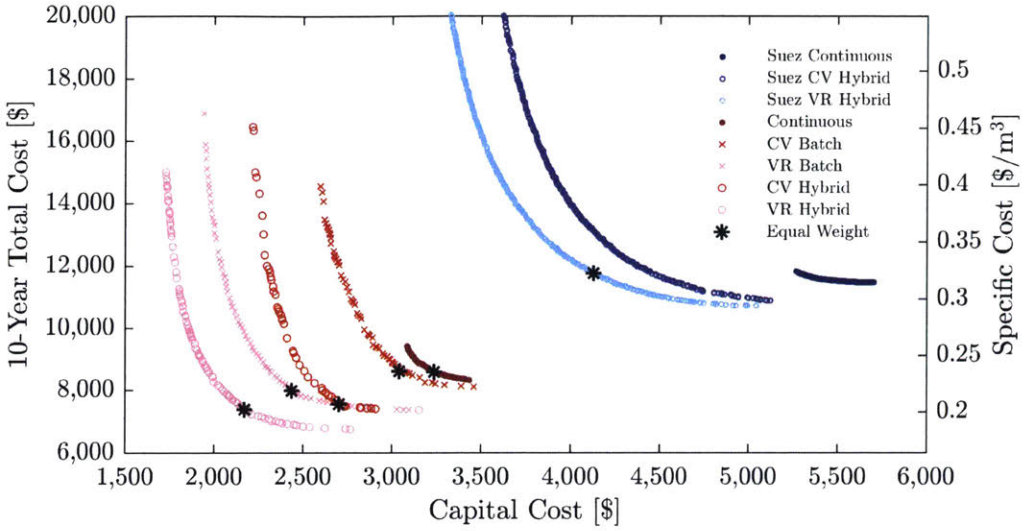

Figure 3-7: The Pareto fronts for all five operating modes, optimized for both operating conditions (flow rate, applied voltage) and geometry (membrane length and width, channel gap, and number of cell pairs) are shown in red. Blue points display parallel results for optimization assuming commercially available Suez components. Black stars indicate the the equal weight designs, the designs that should be selected if equal importance is placed on CC and TC.

The optimal continuous system for the fully optimized case (dark red points) had three electrical stages, whereas the optimal continuous system utilizing Suez components (dark blue points) had two electrical stages, each with two hydraulic stages.

These results show that the VR hybrid operating mode outperforms all other configurations in terms of both CC and TC. The black stars mark the designs that should be used if equal importance is placed on CC and TC; we will call those points the equal weight designs. Table 3.4 reports the gains that are made when switching between the equal weight designs associated with each of the five operating modes and Table 3.5 reports the associated design vectors.

For batch and hybrid operation modes the channel gap approaches the lower bound of 0.3 mm and the volumetric flow velocity approaches the upper bound of 10,000 L/h. Linear

Table 3.4: Cost gains made by switching between the five operating modes

From	To	Decrease in TC	Decrease in CC
Continuous	CV Batch	0%	6%
Continuous	VR Hybrid	14%	33%
CV Batch	CV Hybrid	12%	11%
CV Batch	VR Batch	7%	20%
VR Batch	VR Hybrid	8%	11%
CV Hybrid	VR Hybrid	2%	20%
Suez VR Hybrid	VR Hybrid	37%	47%

Table 3.5: Design vector of the equal weight point for the five operating modes and the baseline parameters. Note that all N have been rounded up to the nearest integer and that the optimal continuous system was a three electrical stage system with one hydraulic stage per electrical stage. The number of cell pairs and V/N ratio has been reported for each stage.

Operating Mode	W [cm]	L [cm]	h [mm]	N [-]	Q_d [L/h]	V/N [V]
CV Batch	33.2	28.5	3.2	240	9694	0.54
VR Batch	22.7	21.2	3.0	370	9825	0.88
CV Hybrid	32.7	24.3	3.1	248	9067	0.53
VR Hybrid	**20.9**	**19.0**	**3.0**	**386**	**9516**	**0.91**
Continuous (3E-1H)	13.3	85.9	4.3	62,51,49	1000	0.64,0.60,0.59

flow velocities range from 10.0 to 10.8 cm/s for batch and hybrid cases, while a velocity of 7.9 cm/s, increasing to 9.6 and 10.0 cm/s in the subsequent stages is optimal for the continuous case. The design vector that produces the optimal equal weight point for the VR hybrid operating mode (bolded row in Table 3.5) will be termed the "baseline case" moving forward.

Holding the flow configuration (batch or hybrid) constant, we see an average TC reduction of 5% and an average CC reduction of 20% when switching from CV to VR mode (Table 3.4). The choice to implement VR operation depends on the added cost of adding a variable voltage rectifier and VR control. The maximum applied voltage is also higher for VR than CV (351 V versus 131 V, respectively to for the hybrid cases) which may also increase the cost of the rectifier.

To understand why VR reduces the system CC (thereby reducing the TC as well) we

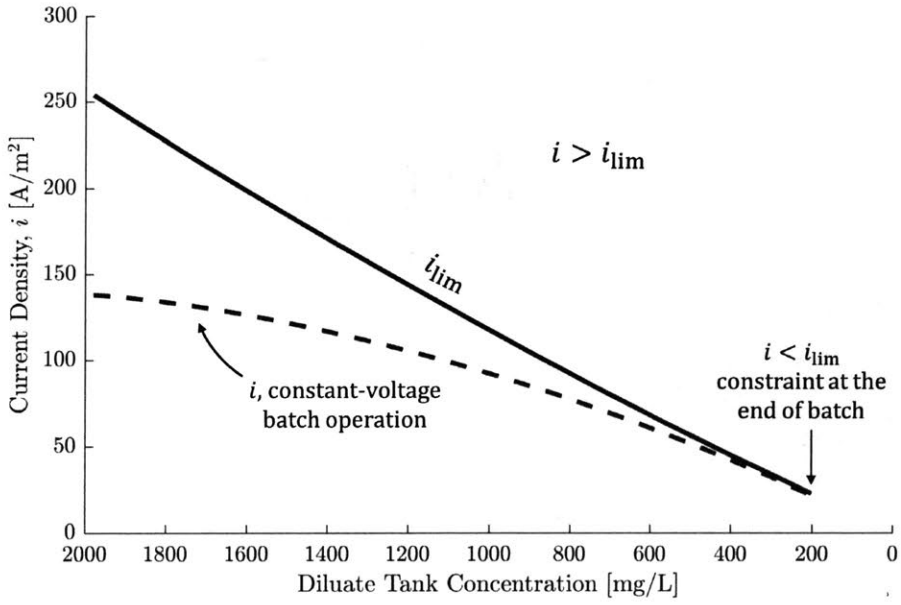

Figure 3-8: Applied current density i (dashed line) versus limiting current density i_{lim} (solid line) for the equal weight CV batch optimal design. Gap between the two lines indicates operation time when the available membrane capacity is not being used to its fullest potential.

look at a visual representation of the limiting current density versus the applied current density throughout the desalination process. Figure 3-8 shows this trend for the CV batch equal weight design. Notice that the applied (dashed line) and limiting (solid line) current densities match only at the very end of the batch, such that any increase in applied voltage would cause $i > i_{lim}$ and a constraint to be violated. As a result of the gap between the two lines for most of the batch, the available membrane capacity is not being used to its fullest. Similarly, Fig. 3-9 shows the relationship between i and i_{lim} for the three electrical stage continuous system. While the curves now come together at three locations (instead of one in the CV batch case), there is still a gap between them, leaving room for enhanced use of the available membrane capacity. When operating a system in VR mode, this gap is closed because the applied voltage is constantly being set such that $i = i_{lim}$.

Next, holding the voltage application constant (CV or VR), we see an average TC

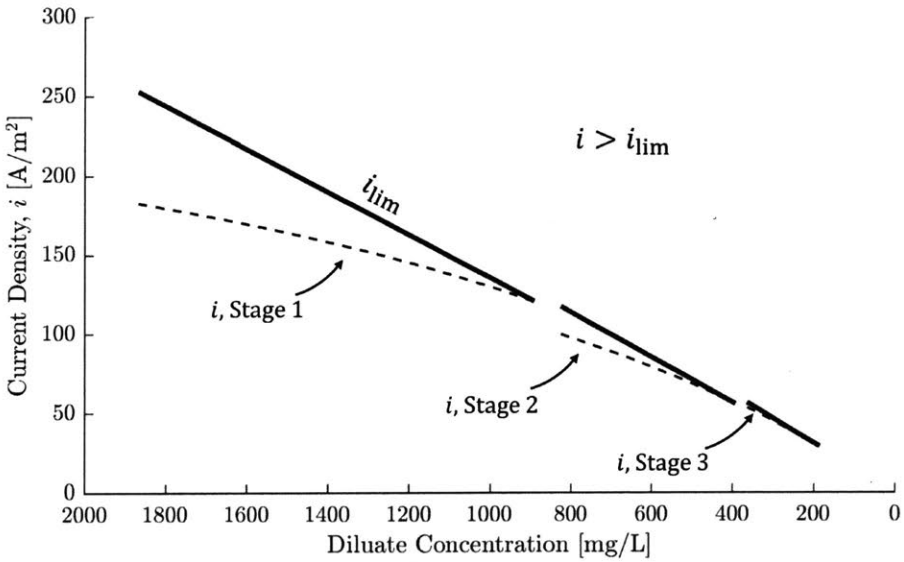

Figure 3-9: Applied current density i (dashed line) versus limiting current density i_{lim} (solid line) for the equal weight continuous optimal design. Gap between the two lines indicates operation time when the available membrane capacity is not being used to its fullest potential.

reduction of 10% and CC reduction of 11% when switching from batch to hybrid mode (Table 3.4). Assuming that there is already a conductivity probe at the diluate stack outlet and level indicators in both the diluate and brine tanks (likely a safe assumption for a batch system operating in batch mode), the upgrade to hybrid mode should not involve added capital and thus this flow configuration should be strongly considered.

The gains made by allowing the membrane, spacer, and electrode geometry to vary from the standard Suez configuration, while maintaining the same operation mode (VR Hybrid) allows a TC reduction of 37% and a CC reduction of 47%. As these gains dominate all others, it is recommended that the cost and manufacturing ramifications of adding new membrane, spacer, and electrode geometries to what is currently available be explored.

Looking at the component cost breakdown for the five equal weight designs (Fig. 3-10), the stack constitutes 22-31% of the TC, the pumps 13-15%, desalination energy 22-32% and pumping energy 21-25%. The contribution of pumping from a capital cost standpoint

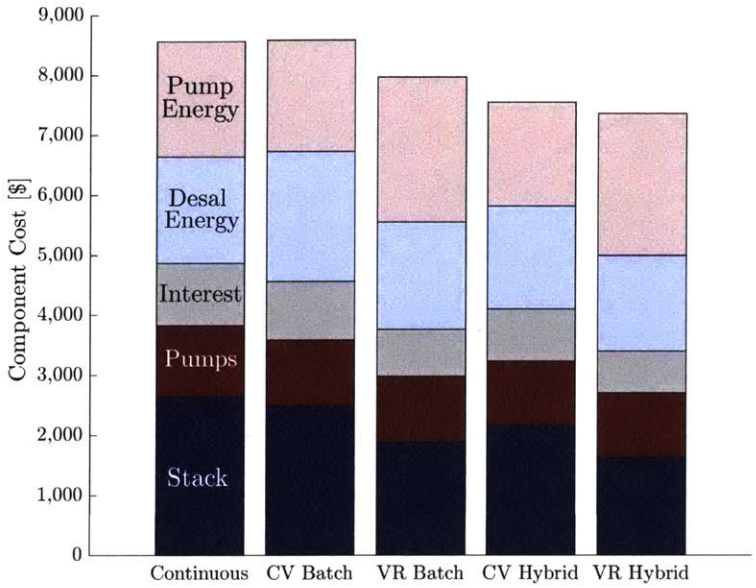

Figure 3-10: The contribution to TC of the stack, pumps, interest, desalination energy, and pump energy at the equal weight point for all five operation modes; all points were optimized over the six design variables (flow channel width and length, channel gap, number of cell pairs, flow rate, and voltage).

highlights the importance of analyzing this cost separately from the ED stack.

The contribution of each component, however, changes dramatically depending on which Pareto optimal design is chosen. Figure 3-11a analyzes the trend in component cost for the best operating mode (VR hybrid), noting that for the lowest CC design, the energetic cost dominates at ≈80% of the total cost. The cost trends can be explained by looking the system design trends for the same operating mode and over the same CC range (Fig. 3-11b through 3-11d). As TC decreases and CC increases moving from left to right along the Pareto front, the linear flow velocity decreases to lower the pressure drop over the stack and reduce the current that needs to be applied to match limiting current density. Lowering the applied current however means that more membrane area is needed in order to remove the same amount of salt (increases the membrane and electrode costs). Additionally, the aspect ratio L/W decreases from approximately 2.3 to 0.7, again reducing the pressure drop.

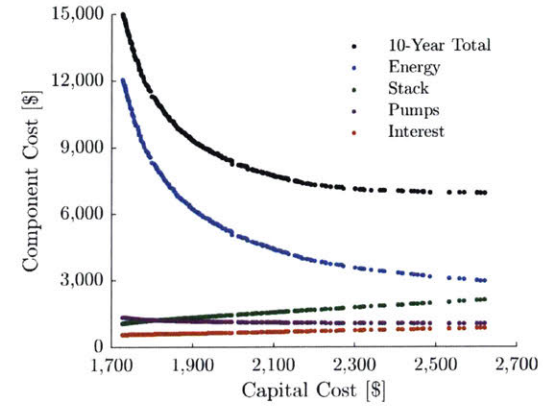

(a) Component Cost

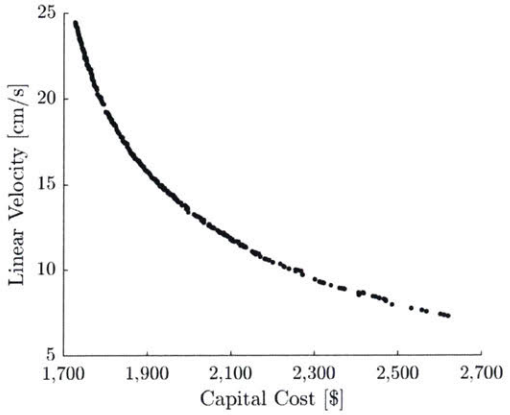

(b) Linear Flow Velocity

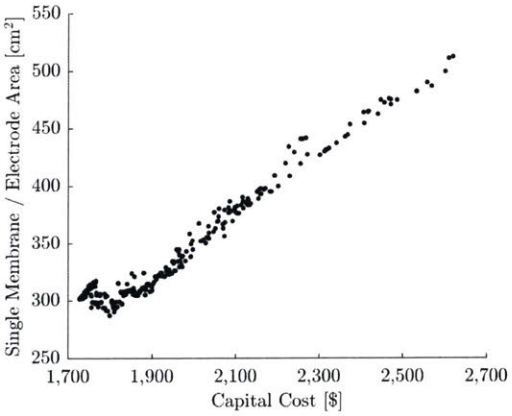

(c) Single Membrane Area

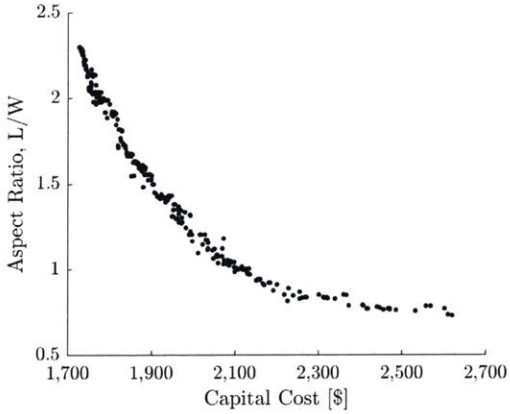

(d) Volts per Cell Pair

Figure 3-11: Trends in the system design and cost along the Pareto front for the VR hybrid operating mode (pink open circles in Fig. 3-7), where the capital cost CC includes the ED stack and the initial set of diluate and concentrate pumps.

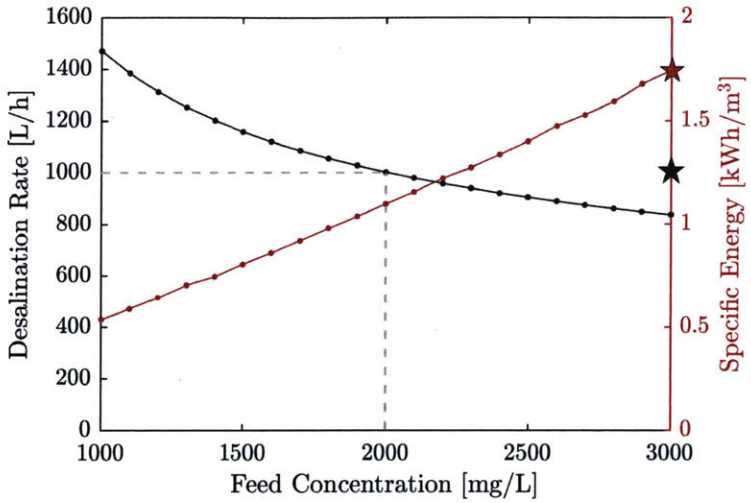

Figure 3-12: Variation of desalination rate Q_p (black line) and specific energy Γ_{total} (red line) with feed concentration C_{feed} assuming the baseline VR hybrid equal weight optimal design for C_{feed}=2000 mg/L is used, regardless of the actual value of C_{feed} at the installed location. The red and black stars indicate the values of Γ_{total} and Q_p, respectively, for the VR hybrid equal weight design that was optimized for a feed concentration of 3000 mg/L, holding all other parameters constant.

3.7 Sensitivity Analysis

We can think about the sensitivity of the results presented in Section 3.6 in a few different ways. First, take the case where the Pareto optimal operation mode (VR hybrid) equal weight point (the baseline case) is selected as the system to manufacture and install across India. Because it is easier to have a single system configuration, we consider what would happen if we installed this baseline system in a location where the groundwater is more or less saline than the baseline case (C_{feed} = 2000 mg/L). Or, when in the years after the system is installed, the local groundwater conditions change, for example due to continued groundwater depletion ($\uparrow C_{\text{feed}}$) or seasonal variation due to times of heavy rains ($\downarrow C_{\text{feed}}$) followed by times of drought. Figure 3-12 shows the variation in desalination rate and energy consumption from the baseline 1000 L/h and 1.09 kWh/m^3.

The specific energy consumption increases as feed concentration increases (which is to be expected); with a feedwater of 3000 mg/L the baseline optimal design requires 1.74 kWh/m^3, an increase of 37% over that required with a 2000 mg/L feed. However, rerunning the optimization algorithm with a 3000 mg/L feed concentration, and finding the new VR hybrid equal weight design results in a system that requires 1.75 kWh/m^3 (red star), a difference of less than 1%. As a result, we can comfortably state that the primary concern with using the baseline optimal design is the reduced desalination rate (down to 836 from 1000 L/h), not an increase in energetic operating costs.

The second area of sensitivity that we explored is that of the VR hybrid equal weight design to the prescribed parameters in Section 3.3. Specifically, we looked at how the optimal design would change if the feed water concentration (2000 mg/L), product water concentration (200 mg/L), energy rate ($0.10/kWh), or electrode cost (1200 $/m^3) varied by $\pm$50% of the baseline value. Varying each parameter independently, we found that the feed and product water concentrations and energy rate had the largest affects on the optimal design and operation (Fig. 3-13). However, none of the conditions (linear flow velocity, total membrane area, or voltage per cell pair) varied by more than 50% from the baseline case. While the total membrane area created the biggest variation, particularly for the 100 mg/L product water case, total membrane area can be increased by increasing the number of cell pairs, suggesting that a single membrane size (L, W) and channel gap (h) could be selected, allowing the exact pump model and number of cell pairs to change to meet the specific need.

3.8 Conclusions

Pareto-optimal designs of ED systems targeting a production rate of 1000 L/h, feed concentration of 2000 mg/L and product concentration of 200 mg/L were explored for five different operating modes. The five modes cover three flow configurations (batch, continuous, and

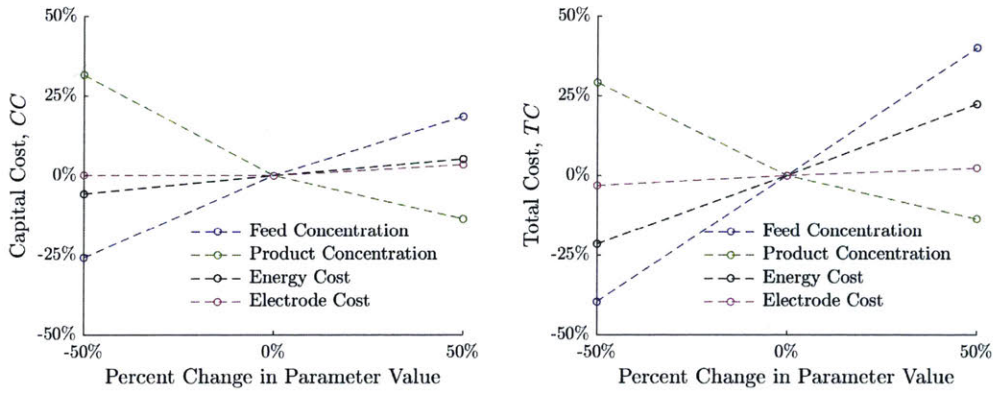

(a) Capital Cost

(b) Total Cost

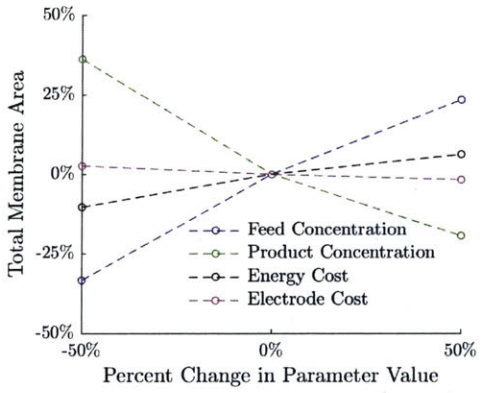

(c) Total Membrane Area

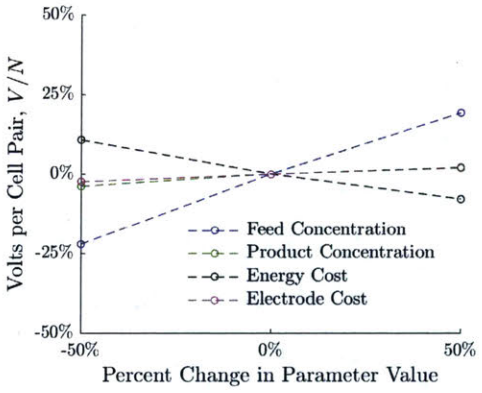

(d) Volts per Cell Pair

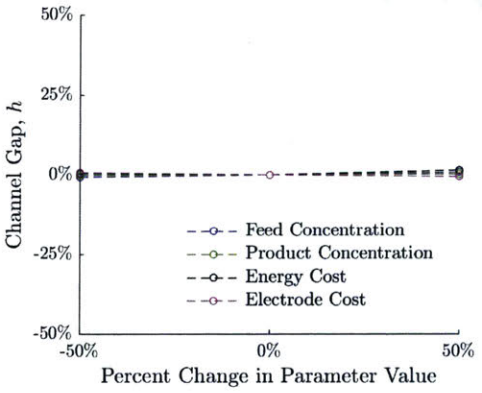

(e) Channel Gap

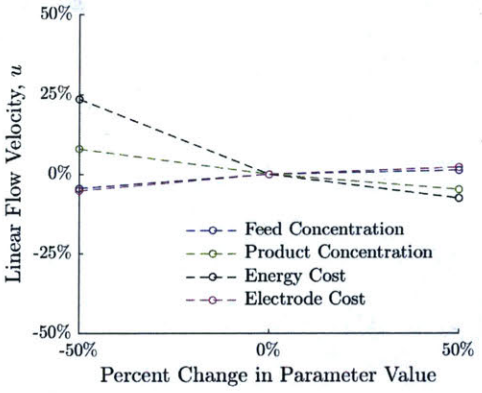

(f) Linear Flow Velocity

Figure 3-13: Sensitivity of the optimal design to ±50% variation in the prescribed optimization parameters of feed concentration (2000 mg/L), product concentration (200 mg/L), energy cost ($0.10/kWh), and electrode price ($1200/m^2).

hybrid) and two methods of applying voltage (constant voltage (CV) and voltage regulated (VR)). Commonly used modes including multi-stage continuous and constant voltage (CV) batch were explored alongside new configurations.

The VR hybrid configuration was found to dominate all other operating modes. The baseline VR hybrid design that placed equal importance on total and capital cost had an active membrane width W of 20.9 cm, length L of 19.0 cm, channel gap of 0.30 mm, 386 cell pairs, 10.8 cm/s linear flow velocity, and 0.91 applied volts per cell pair maximum. The equal weight design for all five operating modes approached the lower bound of the channel gap (0.30 mm). Batch and hybrid configuration produced individual membranes sizes of 0.08-0.19 m^2, with length to width ratios of 0.74-0.93.

We found that transitioning from CV to VR operation resulted in a TC and CC reduction of 5% and 20%, respectively, while a move from batch to hybrid resulted in a TC and CC reduction of 10% and 11%, respectively. Optimizing a system using existing Suez membrane, spacer, and electrode geometries, but allowing operation parameters to change showed that a 37% reduction in TC and 47% reduction in CC could be obtained if these geometries were allowed to change. As a result, it is recommended that hybrid operation modes be considered, that the cost of adding VR be analyzed, and that strong consideration is placed on updating the membrane, spacer, and electrode geometries for the specific production rates required in village-scale systems.

Sensitivity analysis showed that the baseline VR hybrid design that placed equal importance on total and capital cost represented a system that could provide 836 L/h of product water (instead of 1000 L/h) for a nearly identical energetic cost ($\pm$ 1%) when switched to a feed water concentration of 3000 mg/L, demonstrating the robustness of the design to seasonally varying feed water concentration and installation in locations with different levels of groundwater salinity. Additionally, when prescribed cost parameters and desalination targets (feed concentration and production concentration) were varied by $\pm$50% in the optimization, less than 45% variation was found on key system design parameters; this

was the result of prescribing 100 mg/L product water on the optimal total membrane area, a variable that could readily be changed by changing the number of cell pairs without changing the membrane, spacer, or electrode geometry.

This work presents the optimization of a 1000 L/h brackish water ED system. While small-scale systems are investigated here, the work includes operating modes that have not previously been optimized for any size scale such as active voltage regulation and hybrid batch-continuous systems.

Appendix: Modeling Multiple Hydraulic Stages

This appendix presents an extension to the analytical model presented in Chapter 2 that allows the model to be used to describe the behavior of an electrodialysis stack having multiple electrical and/or hydraulic stages. The additions ensure that the treatment of current distribution through the stack is adequately addressed, which is validated experimentally.

The importance of discretizing the flow channel into multiple segments such that, within each segment, the solution is well mixed, has already been discussed in Section 2.5.3. Recall that as the diluate concentration decreases as the solution moves from one segment to the next, the resistance increases and thus the current flow decreases. The distinction that must be made here, however, is how the flow making a second pass through the electrodes in the second hydraulic stage affects the applied current.

Current distribution

The importance of discretizing the flow channel into multiple segments such that, within each segment, the solution is well mixed, has already been discussed in Section 2.5.3. Recall that as the diluate concentration decreases as the solution moves from one segment to the next, the resistance increases and thus the current decreases. The distinction that must be made here, however, is how the flow making a second pass through the electrodes affects

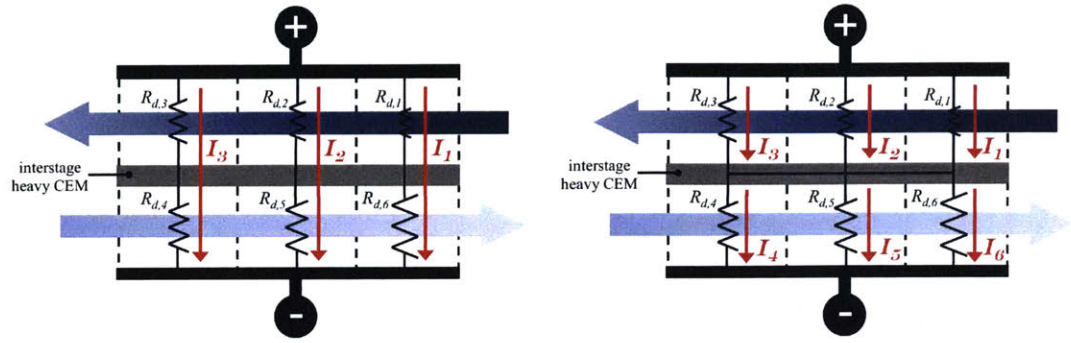

(a) (b)

Figure 3-14: Options for how the current flow could be represented when multiple hydraulic stages are present within a single ED stack. Only the diluate stream is shown since it represents the greatest resistance. The electrical resistance in the diluate stream will increase as the solution moves from segment 1 to segment 6. In current flow option (b) the current redistributes laterally at the interstage membrane, allowing the local applied current to decrease in each cell (e.g. $I_1 > I_2 > I_3 > I_4 > I_5 > I_6$). In option (a), the current does not redistribute at the interstage membrane, resulting in nearly constant current throughout the stack (e.g. $I_1 \approx I_2 \approx I_3$).

the current applied.

Two potential representations of the current flow are shown in Fig. 3-14. In (a) it is assumed that the potential over the membranes is constant along the electrodes, but no where else in the stack. Current does not redistribute at the interstage membrane, thus the current through channel segment 1 and channel segment 6 is the same. In (b) it is assumed that the current is able to redistribute at the interstage membrane, and thus that the current through channel segment 1 and channel segment 6 are different. While intuitively it may be obvious that option (a) more accurately represents true behavior, the distinction is critical because in option (a), I_1 is limited by the concentration is channel segment 6, whereas in (b), I_1 is limited by the concentration in channel segment 1. As a result, option (a) provides a smaller total current that can be applied before exceed limiting current at some point in the stack as compared to option (b), and thus less salt removal for the same

membrane area.

The ED stack is modeled as an analogous DC circuit whereby the voltage applied at the electrodes (E_{total}), and the resulting current for a single hydraulic stage by Eq. 3.16 and for a multiple hydraulic stage stage by

$$E_{\text{total}} = E_{\text{el}} + \sum_{j=1}^{J}[N_j E_{y,j}^{\text{mem}} + N_j i_y (R_{d,y,j}^{b} + R_{c,y,j}^{b} + R_{y,j}^{BL} + R^{AEM} + R^{CEM})], \quad (3.16)$$

where the subscript y remains the stack segmentation as described in Section 2.5.3, x is the segment of the flow path, j is the hydraulic stage, and J is the total number of hydraulic stages. Note that the total number of segments in the flow path X is the product of the number of segments the stack and the total number of hydraulic stages ($X = YJ$). For example in Fig. 3-14a, $Y = 3$, $J = 2$, and $X = 6$. Because the channel resistances ($R_{d,y,j}^{b}$, $R_{c,y,j}^{b}$, $R_{y,j}^{BL}$) and the potential across the membranes ($E_{y,j}^{\text{mem}}$) now depends on both the hydraulic stage and the stack segment, the additional subscript j has been added.

The total instantaneous current (I_{total}), assuming uniform segmentation, is the sum of all current densities (i_y), multiplied by the area of the segment ($\frac{WL}{Y}$), and the open-area porosity of the turbulence-promoting channel spacer (ϕ_A) as given previously in Eq. 2.2 and repeated here for clarity.

$$I_{\text{total}} = \phi_A (\frac{WL}{Y}) \sum_{y=1}^{Y} i_y \quad (2.2)$$

Updating the mass balance equation for an individual diluate channel segment from that given in Section 2.2.3 to account for multiple hydraulic stages leads to Eq. 3.17.

$$\frac{dC^b_{d,x}}{dt} = \frac{1}{N_j V^{\text{cell}}_x}[Q_d(C^b_{d,x-1} - C^b_{d,x}) - \frac{N_j \phi I_y}{zF} + \frac{N_j A_x D^{AEM}(C^{AEM}_{c,x} - C^{AEM}_{d,x})}{l^{AEM}} + \frac{N_j A_x D^{CEM}(C^{CEM}_{c,x} - C^{CEM}_{d,x})}{l^{CEM}}], \tag{3.17}$$

where subscripts x and j have been added to distinguish between channel segments and current segments as was necessary in the circuit analogy equations.

Bibliography

[1] Natasha C. Wright and Amos G. Winter V. Justification for community-scale photovoltaic-powered electrodialysis desalination systems for inland rural villages in India. *Desalination*, 352:82–91, 2014.

[2] Sahil Shah, Natasha Wright, Patrick Nepsky, and Amos G. Winter V. Cost-optimal design of a batch electrodialysis system for domestic desalination of brackish groundwater. *Desalination (Accepted for Publication).*

[3] Eun-Young Choi, Jae-Hwan Choi, and Seung-Hyeon Moon. An electrodialysis model for determination of the optimal current density. *Desalination*, 153:399–404, 2002.

[4] Panagiotis Tsiakis and Lazaros Papageorgiou. Optimal design of an electrodialysis brackish water desalination plant. *Desalination*, 173:173–186, 2005.

[5] Karim M. Chehayeb, Daniel M. Farhat, Kishor G. Nayar, and John H. Lienhard V. Optimal design and operation of electrodialysis for brackish-water desalination and for high-salinity brine concentration. *Desalination*, 420:167–182, 2017.

[6] C. P. Koutsou, S. G. Yiantsios, and A. J. Karabelas. A numerical and experimental study of mass transfer in spacer-filled channels: Effects of spacer geometrical characteristics and Schmidt number. *Journal of Membrane Science*, 326:234–251, 2009.

[7] Chiedza Nezungai and Thokozani Majozi. Optimum synthesis of an electrodialysis framework with a Background Process II: Optimization and synthesis of a water network. *Chemical Engineering Science*, 147:189–199, 2016.

[8] Hong-Joo Lee, F. Sarfert, H. Strathmann, and Seung-Hyeon Moon. Designing of an electrodialysis desalination plant. *Desalination*, 142:267–286, 2002.

[9] K. Hattenbach and K. Kneifel. The effect of cell thickness and flow velocity on water cost in desalination by electrodialysis. *Desalination*, 58:33–41, 1986.

[10] GE Power & Water. *GE Aquamite EDR Systems, FS1360EN.*

[11] Sahil Shah, Natasha Wright, and Amos G. Winter V. Voltage-Regulation as a Means of Reducing Electrodialysis Stack Size. *In Review.*

[12] American Water Works Association. *Electrodialysis and Electrodialysis Reversal: Manual of Water Supply Practices*, 1995.

[13] Ronan K. McGovern, Syed M. Zubair, and John H. Lienhard V. The cost effectiveness of electrodialysis for diverse salinity applications. *Desalination*, 348:57–65, 2014.

[14] Baoji Changli Special Metal Co. Ltd., Shaanxi, China. *Platinized Titanium Anode*, 2014.

[15] Kishor G. Nayar, P. Sundararaman, J. D. Schacherl, C. L. O'Connor, Michael L. Heath, Mario O. Gabriel, Sahil R. Shah, Natasha C. Wright, and Amos G Winter V. Feasibility Study of an Electrodialysis System for In-Home Water Desalination in Urban India. *Development Engineering*, 2:38–46, 2016.

[16] Jamie Vinsant. Personal Conversation with Mr. Jamie Vinsant, Suez Water Technologies & Solutions. February 2017.

[17] Hangzhou Iontech Environmental Co. Ltd., Zhejiang, China. *IONSEP Membranes*, 2014.

[18] Weihai Cortec International Trade Co. Ltd., Shandong, China. *Plastic Spacer for RO Membrane Rolling*, 2015.

[19] Anand Kumar. Personal Conversation with Mr. Anand Kumar, Tata Projects Water Purification Plant Development Center, Secunderabad, India. January 2014.

[20] K. Deb and T. Goel. Controlled Elitist Non-dominated Sorting Genetic Algorithms for Better Convergence. In *Lecture Notes in Computer Science*, pages 67–81. Springer Berlin Heidelberg.

[21] MATLAB. *version 8.6.0 (R2015b)*. Natick, Massachusetts, 2010.

THIS PAGE INTENTIONALLY LEFT BLANK

Chapter 4

Design of Spiral-Wound Electrodialysis Modules

Spiral-wound electrodialysis (ED) modules are of interest because, in a parallel flow configuration where both the diluate and concentrate streams flow from the inner electrode to the outer electrode along a spiral path, the applied current density decreases as the concentration in the diluate stream and associated limiting current density (LCD) decreases. By matching the applied current density as closely as possible to the LCD at any given location in a stack, the required amount of membrane area is minimized, reducing capital cost. This work presents an analytical model for a spiral-wound ED module and experimental validation of that model using a prototype stack with two cell pairs and four turns. A constant voltage was applied and the total current, and mid-stack and final water stream concentrations were recorded. Experimental results agreed with the model for all parameters to within 15%. The model has then been used to explore the most cost-effective spiral stack designs of both a standard Archimedean spiral (as is common for spiral RO modules), and a

novel ideal spiral. The ideal spiral shape was found to reduce total cost by 21% and capital cost by 39% with respect to an Archimedean spiral.

4.1 Introduction

While improvements have been made to individual components, the basic architecture of commercial electrodialysis (ED) stacks has not changed since the concept of a multi-compartment ED cell having alternating cation and anion exchange membranes was first proposed by Meyer and Strauss in 1940 [1]. Commercial ED stacks manufactured for example by Suez Water Technologies & Solutions and Hangzhou Iontech have a similar architecture in which flat, rectangular membranes are sandwiched between two or more electrodes.

Spiral-wound ED modules are of interest because, in a parallel flow configuration where both the diluate and concentrate streams flow from the inner electrode to the outer electrode along a spiral path (Fig. 4-1), or a cross flow configuration in which only the diluate stream flows from inner to outer electrode, the applied current density decreases as the concentration in the diluate stream and associated limiting current density (LCD) decreases. By matching the applied current density as closely as possible to the LCD at any given location in a stack, the required amount of membrane area is minimized. Figure 4-1 shows how the feed water enters alternating cation and anion exchange membranes (CEM, AEM) and the separation into diluate and concentrate streams.

Wen et. al. modeled spiral-wound ED [2, 3] with a number of limitations that the present model incorporates, namely the effect of channel properties (such as spacer geometry), concentration potential, resistance due in the boundary layer, and limiting current density. This final point is critical, as the proposed benefit of a

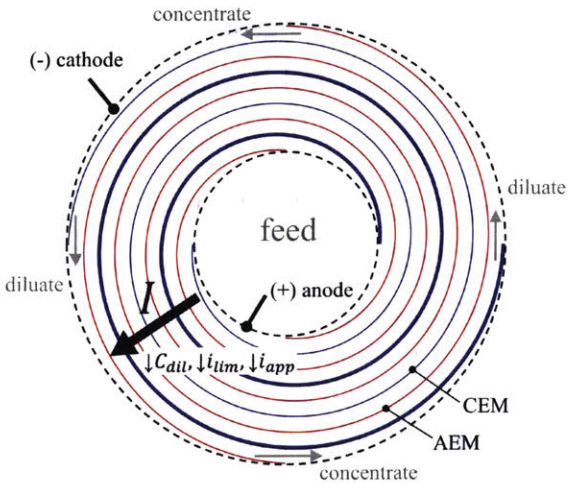

Figure 4-1: A spiral-wound ED module in which feed water entering through a perforated center electrode flows through alternating anion and cation exchange membranes, which have been wound in a spiral fashion around the center electrode. A voltage applied across the anode and cathode drives a current, I, which separates the feed into diluate and concentrate streams. A spiral configuration is of interest because both the limiting and applied current densities (i_{lim} and i_{app}, respectively) decreases as the diluate flow moves from the inside to outside electrode.

spiral stack is to maintain current density near limiting at all points along the spiral. Additionally, the model presented here solves for the spiral shape and associated desalination parameters in polar coordinates, which proves critical to obtaining the optimized design. Wen et. al. also tested a spiral-wound ED stack experimentally [4], however the performance was not compared to their analytical model in [2]. There is thus a need for an experimentally validated analytical model for spiral ED modules as well as a discussion on the effect that geometric and operating parameters have on performance. This work aims to address both of these issues. Additionally, this work both optimizes a traditional Archimedean spiral and proposes a novel spiral shape in which the local radius is set to ensure that the applied current density and LCD match along the entire length of the spiral, a condition that is not possible to achieve with a standard Archimedean spiral.

4.2 Analytical Model

The analytical model presented in this work is based on the model for standard flat stack configurations developed and experimentally validated in Chapter 2. Only the modifications to that model that are required to represent the spiral architecture are presented here. In this section, we assume that there is a spiral design with a known inner electrode radius (r_0), number of cell pairs (N), and total turns (S), and calculate the desalination rate, membrane and electrode area used, and energy consumption. This model is then compared to experimental results. In Section 4.4.2 we discuss the inverse problem of determining the optimal number of cell pairs, number of turns, inner electrode radius, and applied voltage such that matching between LCD and applied current density occurs at the beginning and end of the spiral (using an Archimedean spiral shape), and then along the length of the entire

spiral (using a novel ideal spiral shape).

4.2.1 Defining the Archimedean spiral

An Archimedean spiral (also called an arithmetic spiral) is a spiral in which the radius increases by a constant value with each successive turn of the spiral. The Archimedean spiral thus defines the shape that would be achieved if standard ED cell pairs were wrapped around a center electrode since the thickness of the cell pairs remains constant. This shape is also that employed by spiral-wound RO modules. The local radius of an ED stack wrapped as an Archimedean spiral is defined in polar coordinates as

$$r(\beta) = r_0 + \frac{N t_{cp}}{2\pi}\beta \tag{4.1}$$

where r_0 is the radius of the center electrode, β is the angle around the spiral, and t_{cp} is the thickness of a single cell pair, given as the sum of channel gaps h and the AEM/CEM membranes thicknesses (l_a and l_c, respectively) such that $t_{cp} = 2h+l_a+l_c$. Figure 4-2 shows a two cell pair (N=2), two turn (S=2) Archimedean spiral. The length of a single membrane is found using the equation for the arc length of any curve in polar coordinates,

$$L = \int_0^{\beta_f} \sqrt{r(\beta) + \frac{dr}{d\beta}} \quad d\beta, \tag{4.2}$$

where the integral is evaluated from 0 to $\beta_f = 2\pi S$, the angle at the end of the spiral. The width W of a single membrane is

$$W = \frac{Q_d}{N h u_{ch} \epsilon}, \tag{4.3}$$

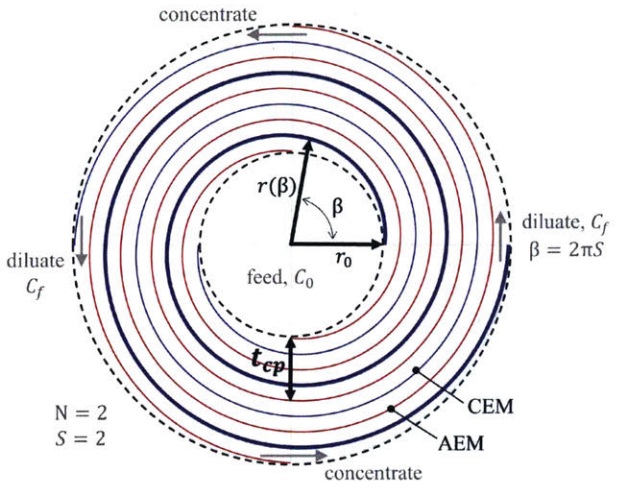

Figure 4-2: The radius of a standard Archimedean spiral increases at a constant rate of *tcp* with each successive turn. This Archimedean spiral stack has four membranes, two cell pairs, and two turns.

where Q_d is the total volumetric flow rate of the diluate (m^3/s), h is the channel gap (m), u_{ch} is the spacer-filled channel velocity (m/s), and ϵ is the void fraction. The total membrane area in the spiral is then given by

$$A_{\text{total}} = 2NLW, \tag{4.4}$$

while the projected area for any given membrane segment covering less than 2π radians can be approximated by

$$A_j = (\frac{\beta_2 - \beta_1}{2\pi})(2\pi r(\beta_1)W), \tag{4.5}$$

where the first term on the right-hand side is the fraction of one full turn being considered. As this term approaches zero, the stack is segmented into smaller paths for the current to flow and the discrete analysis approaches the continuous solution.

4.2.2 Mass Transfer

We begin by neglecting the contribution of back-diffusion due to the ionic concentration gradient between the concentrate and diluate channels. Doing so allows us to solve the set of equations in this section without the use of an iterative solver. The effect that this assumption has on predicted salt removal rates is discussed in Section 4.3.3. The quantity of salt removed in a single pass through the spiral is then a result of migration due to the applied current I alone and is calculated by

$$(C^b_{d,0} - C^b_{d,S}) = \frac{I\phi SN}{zFQ_d}, \tag{4.6}$$

where $C_{d,0}$ is the feed water salinity (mol/m^3) at the center electrode, $C_{d,S}$ is the final diluate salinity (mol/m^3) as it leaves the stack at the final turn S, ϕ is the current leakage factor, z is the ion charge number, F is Faraday's constant (C/mol).

Because the same amount of current must pass through each successive turn of the spiral, the change in concentration must also be the same ($C_{d,0} - C_{d,1} = C_{d,1} - C_{d,2}$). Equation 4.6 thus leads to the equation for the concentration in any given turn of the spiral,

$$C^b_{d,s} = C^b_{d,0} - \frac{I\phi sN}{zFQ_d}, \tag{4.7}$$

where s is the turn number, counting outwards from the inner electrode.

4.2.3 Limiting Current

The maximum current that can be applied to the spiral is calculated as:

$$i_{lim} = \frac{I_{lim}}{\phi_A A} = \frac{C^b_d zFk}{t^{mem} - t_{+,-}} = \frac{C^b_d zFD_{aq}0.29Re_d^{0.5}Sc^{0.33}}{d_h(t^{mem} - t_{+,-})}, \tag{4.8}$$

where definitions of the Reynold's number Re, Schmidt number Sc, hydraulic diameter d_h, and the transport numbers t^{mem} and $t_{+,-}$ are found in Chapter 2. Setting the limiting current I_{lim} in Eq. 4.8 equal to the applied current I in Eq. 4.6, we can solve for the inner electrode radius that would allow the currents to match at the beginning of the flow path, when $C_d^b = C_{d,0}^b$,

$$r_0 = \frac{(1 - CR^{-1})u_{ch}^{1/2}}{S}\xi, \tag{4.9}$$

where

$$\xi = \frac{h^{3/2}\epsilon^{3/2}\mu^{1/6}(t^{mem} - t_{+,-})}{0.29\pi\phi(SF)(2 + 8(1-\epsilon))^{1/2}\rho^{1/6}D_{aq}^{2/3}\phi_A},$$

where $CR = C_{d,0}^b / C_{d,S}^b$, the ratio of feed to product water concentration. Note that if a certain membrane and spacer type is assumed (properties of which are used to calculate ξ), the full spiral shape (Eq. 4.1) can be defined through CR, the channel velocity u_{ch}, the number of turns S, and the number of cell pairs N. In Sections 4.4.2 and 4.4.3 we discuss spiral designs in which we enforce that the limiting and applied current densities match at both the beginning and end of the spiral (for the Archimedean shape), and along the length of the entire spiral (for the ideal shape).

4.2.4 Voltage potential

Just as with standard flat-stack ED architectures, the spiral ED stack is modeled as an analogous DC circuit. The voltage at the electrodes E_{total} is related to the current through Eq. 4.10. However, unlike a single hydraulic stage flat-stack architecture, the current passes through the same solution S times and the area of each successive

flow channel/membrane increases as you move from the inner to outer electrode.

$$E_{\text{total}} = E_{\text{el}} + \frac{I}{\phi_A} \sum_{j=1}^{J} \left(\frac{R^b_{d,j} + R^{BL}_{d,j} + R^{\text{mem}}}{A_{d,j}} + \frac{R^b_{c,j} + R^{BL}_{c,j} + R^{\text{mem}}}{A_{c,j}} \right) + \sum_{j=1}^{J} E_{\text{mem},j} \quad (4.10)$$

Here j indicates the channel location such that $j = 1$ is the diluate and concentrate channel closest to the inner electrode and that a total of $J = NS$ diluate channels, and $J = NS$ concentrate channels exist between the inner and outer electrode. The area resistances $R^b_{d,j}$, $R^{BL}_{d,j}$, $R^b_{c,j}$, and $R^{BL}_{c,j}$ are associated with the bulk and boundary layer fluid in the diluate and concentrate streams, respectively (Ω m^2). The average area resistance of the AEM and CEM exchange membrane is given by R^{mem} (Ω m^2). $A_{d,j}$ and $A_{c,j}$ are the projected areas of the diluate and concentrate channel (m^2) such that both increase as j increases, in accordance with Eq. 4.5. E_{mem} is the potential across each membrane pair; it is a function of the concentration at the membrane wall and thus also changes based on channel location, j. Finally, E_{el} is electrode potential difference. Given a known bulk concentration and effective area for each channel location, each of the terms in Eq. 4.10 can be calculated using equations provided in Chapter 2, Section 2.2.2.

4.2.5 Specific energy

The total specific energy Γ_{total} (J/m^3) is given by the sum of the energy required for desalination and for pumping as,

$$\Gamma_{\text{total}} = \frac{IV_{\text{total}}}{Q_d} + \frac{2P}{\eta_{\text{pump}}}, \quad (4.11)$$

where P is the drop drop in (Pa), η_{pump} is the efficiency of the pump, and it is assumed

that the volumetric flow rate and pressure drop is the same in the concentrate and diluate streams. The pressure drop in the spiral is modeled using the correlation developed by Ponzio et. al. [5] which was found to be the best match to an existing commercial ED system in Section 2.2.7.

4.3 Experimental validation of spiral model

A prototype spiral wound ED stack was assembled and instrumented to validate the analytical model presented in Section 4.2. The experimental setup and results are described here.

4.3.1 Prototype stack design

A photo of the prototype stack at three stages in the assembly process is shown in Fig. 4-3. The inner electrode was made from a Grade 2 titanium tube with 50.8 mm outer diameter and 0.89 mm wall thickness; 6.35 mm diameter holes were added to allow water to enter the flow channels. Two cell pairs (20.5 cm membrane width, 91.4 cm individual membrane length) allowed four full turns before reaching the outer electrode, which was made from 0.13 mm thick 316SS foil. Suez Water Technologies & Solutions AR204SZRA anion exchange membranes and CR67HMR cation exchange membranes, both homogeneous, were used. The mesh spacer was made from Conwed Plastics' 31 mil RO spacer material. Clear PVC pipe (inner diameter 15.8 mm) cut in half lengthwise was used to collect water as it exited the stack. 316SS tubing was inserted into the spiral one-third and two-thirds of the way along the membrane length and used to collect mid-stack water conductivity. Clamps were designed out of HDPE sheet to compress the half-tubes and their gaskets to the

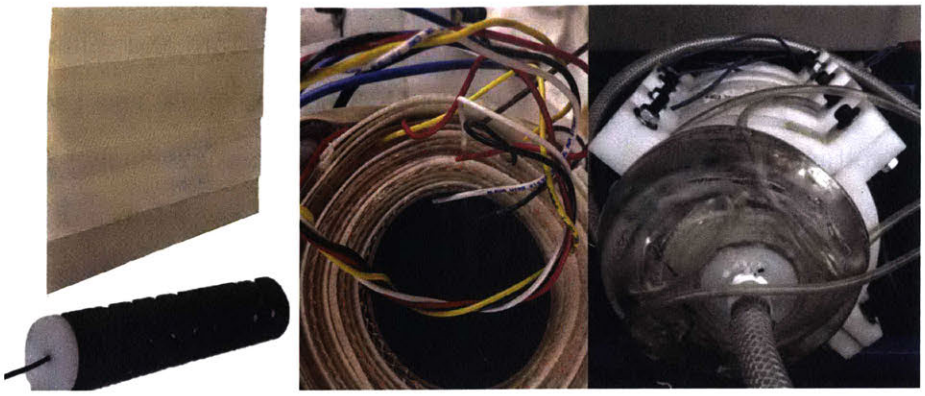

Figure 4-3: The prototype used for model validation was constructed by rolling two membrane/spacer cell pairs around a titanium inner electrode (left) to produce a spiral shape (center). The spiral was sealed by compressing the outer electrodes against the membrane surface using clamps made out of HDPE and using epoxy resin to seal and cap the ends.

membranes. Finally, West System 105 and 207 epoxy resin and hardener was used to seal the ends of the stack. This serves as a replacement for the gasket material that lines the perimeter of traditional flat-stack spacer designs, and ensures that the solution flows from the inner electrode to the outer, without coming out the ends of the spiral. Prior testing showed that the epoxy rose 1.5 cm into the flow channels. As a result, the effective membrane width decreased to 17.5 cm.

4.3.2 Experimental setup

The diluate and concentrate streams were run in continuous mode, flowing in a parallel configuration from the inner electrode tube to the outer collection tubes. The feed solution was prepared using deionized water and the appropriate amount of reagent grade NaCl. A Shurflo 4008-101-E65 pump was used to provide feed solution to the stack; flow rate was controlled manually using a butterfly valve and measured using a Blue-White Industries F-1000-RB paddle wheel flowmeter ($\pm$ 0.2 L/min). It is

assumed that the flow divides equally between the concentrate and diluate channels providing 50% recovery. A Dr. Meter HY3005F-3 power supply was used to apply a constant voltage (± 0.1 V) across the electrodes and measure current (± 0.01 A). The mid-stack and final water stream conductivities were recorded manually over a period of 10 minutes for each test. Conductivity (± 1% of reading) and temperature (± 0.1^{o}C) measurements were taken using a Myron 4PII meter. Experimental error bars in the tables and figures to follow are reported as the quadrature of the sensor accuracy (given in this paragraph) and the 95% confidence interval over 5 measurements taken over the course of each experiment.

4.3.3 Results and Discussion

Table 4.1 lists the prototype stack parameters required for comparison with the analytical model. Note that while a spacer thickness of 0.76 mm was measured prior to rolling the spacer, we were not able to roll the spiral tightly enough to ensure that the channel gap was equal to the spacer thickness. This was confirmed when measurements taken of the outside diameter of the spiral revealed its diameter to be 94.8 mm, whereas the calculated diameter with a spacer thickness of 0.76 mm should be 92.7 mm. Instead, we back-calculated the channel gap (h=0.82 mm), and updated the void fraction calculation to that in Eq. 4.12, resulting in a calculated ϵ=0.83.

$$\epsilon = 1 - \frac{\pi d_f^2 (2l_f - d_f)}{4l_f^2} \tag{4.12}$$

Additionally, the outer electrode sheets covered only 79% of the outer diameter, in order to leave space for the water collection half-tubes. It is assumed that this coverage affects the fractional membrane available for ion transport, similar to the

Table 4.1: Stack Parameters

Membrane Properties	
Supplier	Suez
AEM Model	AR204SZRA
CEM Model	CR67HMR
AEM Resistance (Ω cm^2)	7
CEM Resistance (Ω cm^2)	10
AEM Thickness (mm)	0.5
CEM Thickness (mm)	0.6
Spacer Properties	
Supplier	Conwed Plastics
Model	X0B354
Filament pitch (mm)	2.9 ± 0.1
Filament diameter (mm)	0.53 ± 0.03
Spacer Thickness (mm)	0.76 ± 0.01
Calculated Area Porosity	0.67 ± 0.02
Spiral Properties	
Flow Path Width (cm)	17.5
Flow Path Length (cm)	91.4
Number of Cell Pairs	2
Number of turns	4
Inner electrode radius (cm)	2.54
Channel Gap (mm)	0.82 ± 0.02
Calculated Void Fraction	0.83 ± 0.03
Electrode Coverage	0.79
Combined View-Factor	0.53

way the spacer area porosity (ϕ_A=0.67) does. A net "view-factor" is applied instead of the area porosity, where $VF = (0.79)(0.67) = 0.53$.

Table 4.2 presents the time averaged results from the experiment alongside the model prediction of the same parameters for all five tests. Note that the experimentally measure applied current, feed water conductivity, and flow rate served as inputs to the model; voltage potential, specific energy, and product, brine and mid-stack conductivities were model outputs. Measurements matched the model within 1-15% (average 7%) for the voltage potential and specific energy and within 1-11% (average 5%) for the conductivities.

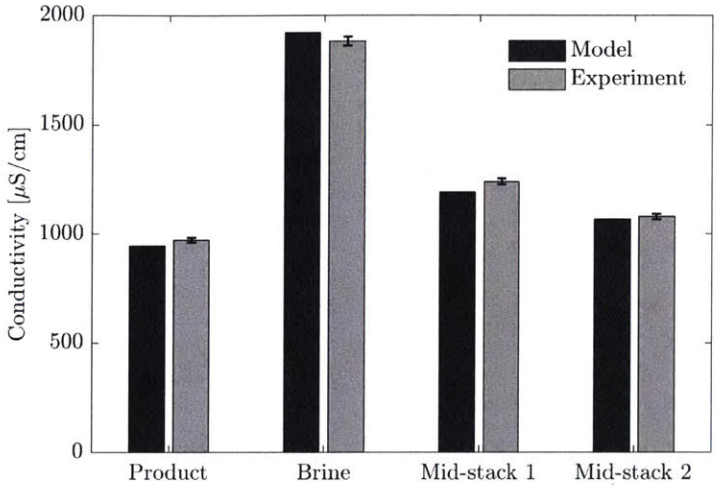

Figure 4-4: Conductivity measurements for Test 1 shown in relationship to the model prediction.

The conductivity results for Test 1 are shown as a bar graph in Fig. 4-4 in order to better visualize the trend in data. We note, for example, that the model slightly under predicts the experimental values in the diluate stream, while over predicting the experimental values in the brine stream. This trend was present for all tests except Test 4. This difference is expected given the decision to neglect back diffusion in the model, allowing the full problem to be solved directly without iteration.

There are a number of changes that could be incorporated to help determine the source of any error between model and experiments, as well as improve the overall performance and life of the experimental spiral stack. First, the small tubes inserted in two locations in the stack to probe for concentration should be added to every turn, and in both the diluate and concentrate stream, allowing for better accounting of propagated error. Currently, the first membrane layer does not lay perfectly flat on the inner electrode, resulting in a fluid layer between the two surfaces and increased electrical resistance. A better method of assembling the spiral that would allow for

a flush fit along the center electrode is needed. The stainless steel outer electrode and titanium inner electrode should be should be replaced with coated titanium to avoid development of pitting and rust. While these improvements are in progress, the current stack proved sufficient for initial validation of the analytical model and for recording the overall feasibility of desalinating using a spiral-wound ED module.

Table 4.2: Experimental measurements and modeled results for five tests on the prototype Archimedean spiral ED stack, each of which had different feed water concentration and applied voltages. Measurements matched model values within 1-15% (average 7%) for voltage potential and within 1-11% (average 5%) for the conductivities.

	Test 1		Test 2		Test 3		Test 4		Test 5	
Parameter	**Exp**	**Model**	**Exp**	**Model**	**Exp**	**Model**	**Exp**	**Model**	**Exp**	**Model**
Voltage [V]	7.5 ± 0.1	7.6	8.0 ± 0.1	8.0	10.0 ± 0.1	11.0	14.0 ± 0.1	12.8	10.0 ± 0.1	8.5
Current [A]	0.95 ± 0.30	0.95	1.44 ± 0.02	1.44	2.53 ± 0.03	2.53	2.30 ± 0.05	2.30	2.94 ± 0.06	2.94
Flow Rate [L/min]	2.07 ± 0.22	2.07	2.03 ± 0.20	2.03	1.98 ± 0.20	1.98	2.46 ± 0.22	2.46	2.65 ± 0.36	2.65
Feed Conductivity [μS/cm]	1436 ± 16	1436	2149 ± 23	2149	3022 ± 31	3022	1983 ± 42	1983	4503 ± 46	4503
Product Conductivity [μS/cm]	971 ± 11	943	1495 ± 24	1402	1903 ± 22	1697	940 ± 45	988	3471 ± 112	3389
Brine Conductivity [μS/cm]	1882 ± 21	1921	2882 ± 35	2883	4231 ± 50	4312	2881 ± 67	2950	5380 ± 78	5597
Mid-Stack Diluate 1 Conductivity [μS/cm]	1240 ± 14	1191	1880 ± 29	1778	2567 ± 28	2365	1524 ± 34	1490	4077 ± 42	3948
Mid-Stack Diluate 2 Conductivity [μS/cm]	1079 ± 12	1067	1638 ± 40	1591	2191 ± 38	2033	1246 ± 33	1240	3774 ± 44	3669
Specific Energy [kWh/m^3]	0.06 ± 0.02	0.06	0.09 ± 0.01	0.09	0.21 ± 0.02	0.23	0.22 ± 0.02	0.20	0.18 ± 0.03	0.16

4.4 Optimization of Spiral Design

With confidence that the spiral ED stack model adequately predicts behavior, we can move forward with a multi-objective design optimization problem in which we identify the Archimedean and ideal spiral geometries and operating parameters that provide the lowest 10-year total cost and capital cost.

4.4.1 Optimization of the Archimedean Design

For all Archimedean spiral designs in this section, we ensure that the applied current density is equal to the LCD at the beginning and end of the spiral through Eq. 4.13. For consistency with the work completed in Chapter 3, the same baseline parameters are used. Specifically, we consider desalination of 2000 mg/L NaCl feed water to product water of 200 mg/L at a rate of 1000 L/h, using cost parameters of \$1200/m^2 electrode area, \$40/m^2 membrane area, \$10/m^2 spacer area, \$0.10/kWh of energy, and the pump cost and efficiency model described in Eqs. 3.2 and 3.3. The design variables and associated bounds are the channel gap (0.3 mm $< h <$ 1.0 mm), the spacer-filled channel velocity (6 cm/s $< u_{ch} <$ 20 cm/s), and number of cell pairs ($1 < N < 300$).

The 10-year total cost and capital cost are solved for directly using the following steps:

1. Calculate the total number of turns required to achieve the desired concentration change, given the design variables h, u_{ch}, and N:

$$S = \left[\left(\frac{u_{ch}^{1/2} \xi}{t_{cp} N} \right) \left(\frac{C_{d,0}^2 - C_{d,J}^2}{C_{d,0} C_{d,J}} - 2 \right) \right]^{1/2} \tag{4.13}$$

2. Calculate the radius of the inner electrode, r_0 (Eq. 4.2.3).

3. Calculate the maximum number of cell pairs that can start from the inner electrode. If $N < N_{\max}$, continue with calculation.

$$N_{\max} = \frac{2\pi r_0}{t_{cp}} \tag{4.14}$$

4. Calculate the length, L, and width, W, of a single membrane (Eqs. 4.2 and 4.3).

5. Calculate the area of membrane segments (Eq. 4.5).

6. Calculate the current I that is required to achieve the desired concentration change (Eq. 4.6).

7. Calculate the concentration reduction in each turn (Eq. 4.7)

8. Calculate the membrane potential and area resistances at each segment (Chapter 2, Section 2.2.2).

9. Calculate the voltage potential across the whole stack (Eq. 4.10)

10. Calculate the specific energy for desalination and pumping (Eq. 4.11)

11. Calculate the capital and 10-year total cost for the system (Chapter 3, Section 3.4).

An initial DOE over the bounds of the design variables reveals that all points on the Pareto front utilize the smallest channel thickness (0.3 mm) and maximum number of cell pairs ($N = N_{\max}$). As a result, a full optimization algorithm is not required, and the Pareto front (Fig. 4-5) is calculated by varying u_{ch} alone.

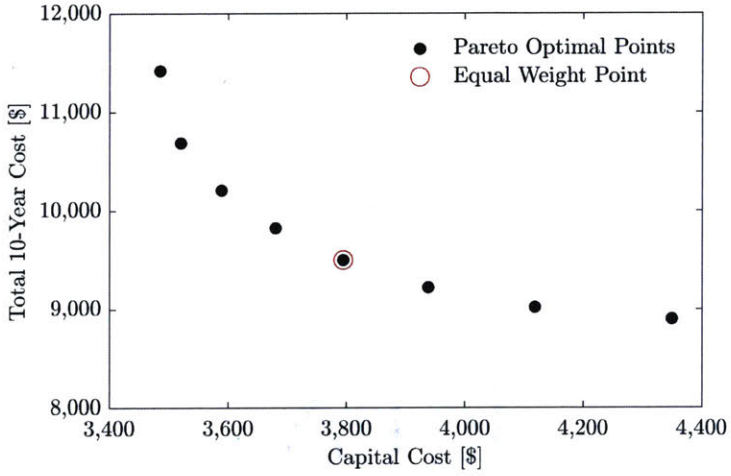

Figure 4-5: The capital cost vs. total cost Pareto front governing the Archimedean spiral. The red open circle denotes the design that places equal important (weight) on the total and capital cost.

The design parameters that govern the lowest capital cost, lowest total cost, and weighted results are shown in Table 4.3.

4.4.2 Limitations of the Archimedean Spiral

Plotting i_{lim} and i as a function of the local concentration in the spiral, reveals that although an Archimedean spiral allows for matching at the inlet and outlet of the stack, there remains a significant amount of wasted membrane capacity in the middle turns.

This spiral shape provides for a linearly decreasing diluate concentration with each successive turn, resulting in a linearly decreasing LCD (Eq. 4.8). However, the radius, and thus the effective area, increases linearly with each turn of the spiral and as a result the applied current density (which scales as I/A) will not decrease linearly as desired.

Table 4.3: Pareto front geometries and operation conditions for the Archimedean spiral.

Parameter	**Lowest Capital Cost**	**Lowest Total Cost**	**Equal Weight**
S [-]	1.4	1.4	1.4
N [-]	222	156	187
h [mm]	0.3	0.3	0.3
W [cm]	3.7	10.5	6.2
r_0 [cm]	6.0	4.3	5.1
r_S [cm]	59.1	41.6	49.8
A_{total} [m^2]	48.3	68.4	57.2
u_{ch} [cm/s]	14	7	10
$i_{j=1}$ [A/m^2]	330	232	278
P [kPa]	682.6	227.8	389.0
Γ_{desal} [kWh/m^3]	0.36	0.29	0.32
Γ_{pump} [kWh/m^3]	1.27	0.42	0.72
Stack Cost [$]	2,599	3,782	3,115
Capital Cost [$]	3,485	4,350	3,795
Total Cost [$]	11,417	8,898	9,497

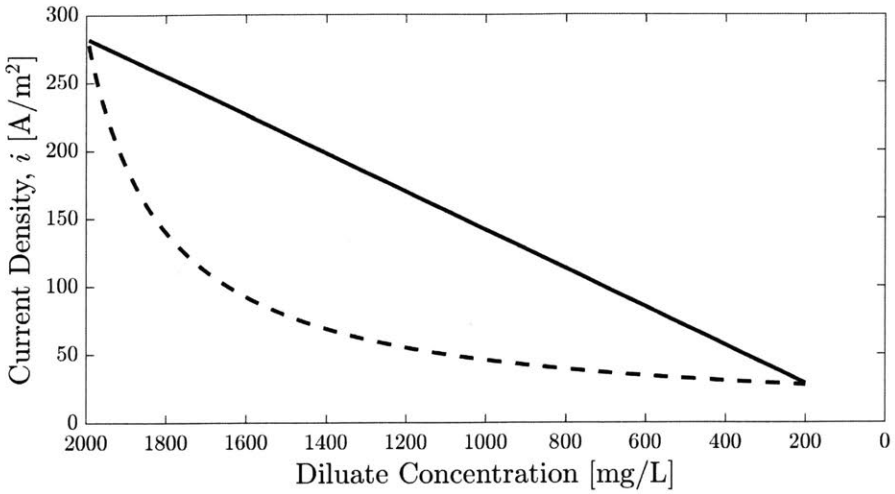

Figure 4-6: In an Archimedean spiral, the stack can be designed such that the applied (dashed line) and limiting (solid line) current densities match at the beginning and end of the stack. However, it is not possible to design an Archimedean spiral with a match at all locations.

4.4.3 Description and Optimization of the Ideal Spiral

Setting the equation for I_{lim} equal to I for all C_d, we can solve for the equation of a spiral that would allow the local applied and limiting current densities to match along the entire length of the spiral. This spiral is described is polar coordinates as:

$$r(\beta) = \frac{r_0}{1 - \beta(\frac{1-CR}{\beta_f})}, \tag{4.15}$$

where CR is the desired concentration ratio $C_{d,0}/C_{d,S}$. As for the Archimedean spiral, we can proceed to examine the best geometry and operating parameters for this ideal spiral shape. The calculation process is the same as in Section 4.4.2 except that there are now two constraints on the number of cell pairs.

$$(1) \quad N \leq N_{\max,1} = \frac{2\pi r_0}{t_{cp}} \tag{4.16}$$

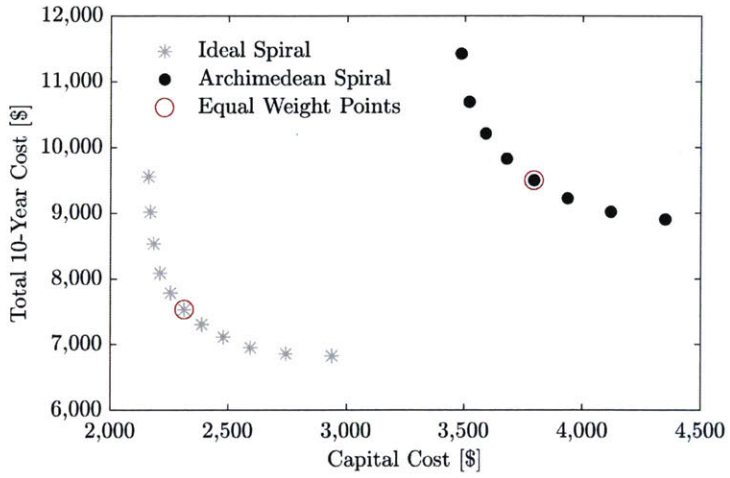

Figure 4-7: A comparison of the capital cost vs. total cost Pareto fronts governing the Archimedean spiral and ideal spirals. The red open circles denote the designs that places equal important (weight) on the total and capital cost.

and,

$$(2) \quad N \leq N_{\max,2} = \frac{r(2\pi) - r_0}{t_{cp}}, \tag{4.17}$$

where the first represents the maximum number of cell pairs that could start from the center electrode and the second represents the maximum number of cell pairs that can fit between the radius at $\beta = 0$ and $\beta = 2\pi$.

Again, the initial DOE over the bounds of the design variables revealed that all points on the Pareto front utilize the smallest channel thickness (0.3 mm) and maximum number of cell pairs (N set to the lower of $N_{\max,1}$ and $N_{\max,2}$). As a result, a full optimization algorithm is not required, and the Pareto front is calculated by varying u_{ch} alone (Fig. 4-7).

Table 4.4: Pareto front geometries and operation conditions for the ideal spiral.

Parameter	**Lowest Capital Cost**	**Lowest Total Cost**	**Equal Weight**
S [-]	1.0	1.0	1.0
N [-]	335	205	277
h [mm]	0.3	0.3	0.3
W [cm]	2.1	9.4	3.8
r_0 [cm]	9.1	5.6	7.5
r_S [cm]	90.7	55.5	75.2
A_{total} [m^2]	24.9	40.6	30.0
u_{ch} [cm/s]	16	6	11
$i_{j=1}$ [A/m^2]	357	219	296
P [kPa]	498.7	99.4	246.7
Γ_{desal} [kWh/m^3]	0.70	0.49	0.61
Γ_{pump} [kWh/m^3]	0.93	0.18	0.46
Stack Cost [$]	1,405	2,461	1,735
Capital Cost [$]	2,162	2,939	2,316
Total Cost [$]	9,551	6,818	7,527

4.4.4 Discussion

The ideal spiral is able to achieve 21% lower total cost and 39% lower capital cost than the Archimedean spiral for the design where both costs are equally weighted, denoted by the red equal weight points in Fig. 4-7. The shape of the spiral for both the Archimedean and ideal designs at these points are shown in Fig. 4-8. While the Archimedean spiral requires 1.4 turns to achieve the desired concentration change, the ideal spiral shape requires 1.0 turns, resulting in less total membrane (30.0 vs 57.2 m^2), lower pressure drop (246.7 vs 389.0 kPa), and a resulting lower capital cost. Note that the outer electrode radius is quite large for this CR, at 79 cm for the ideal spiral, and the stack is thin at only 3.8 cm for the ideal spiral. The stack would resemble discs, rather than long tubes. The width of the membrane however is set by the desired volumetric flow rate, thus higher production capacity would be achieved by increasing the width of the membrane (thickness of the disc).

To understand the sensitivity of the spiral stack designs to changing feed and product water concentrations, Pareto fronts for five scenarios are shown in Fig. 4-9. Focusing first on the star markers, we see that the capital cost is nearly independent of the feed water concentration, so long as the concentration ratio is the same (here CR=10). Higher feed water concentration requires more energy for desalination however, and thus the total 10-year cost increases as expected. Increasing the product water concentration from 200 mg/L to 300 mg/L, while maintaining a feed water concentration of 2000 mg/L, reduces both the capital and total costs by more than 20% at equivalent points on the Pareto front. It is thus important to evaluate opportunities to relax the product water concentration requirement when considering an ideal spiral architecture.

Knowing that stacks designed for the same CR have the same capital cost, and

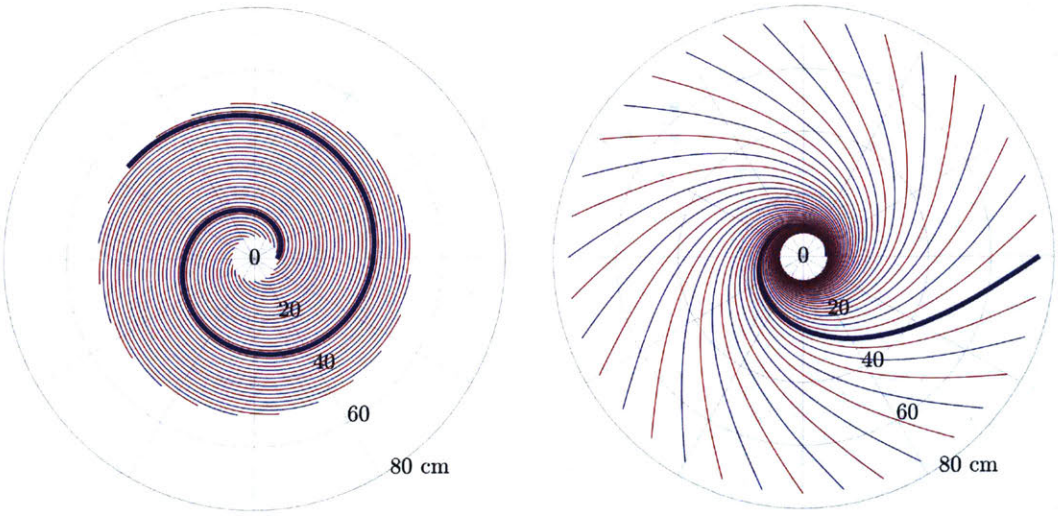

(a) Achimedean Spiral (b) Ideal Spiral

Figure 4-8: Representation of the spiral pattern in the optimized Archimedean and ideal spiral. In both cases the design in which equal importance is placed on total cost and capital cost is presented and 1/15th of the total cell pairs are shown for visual clarity.

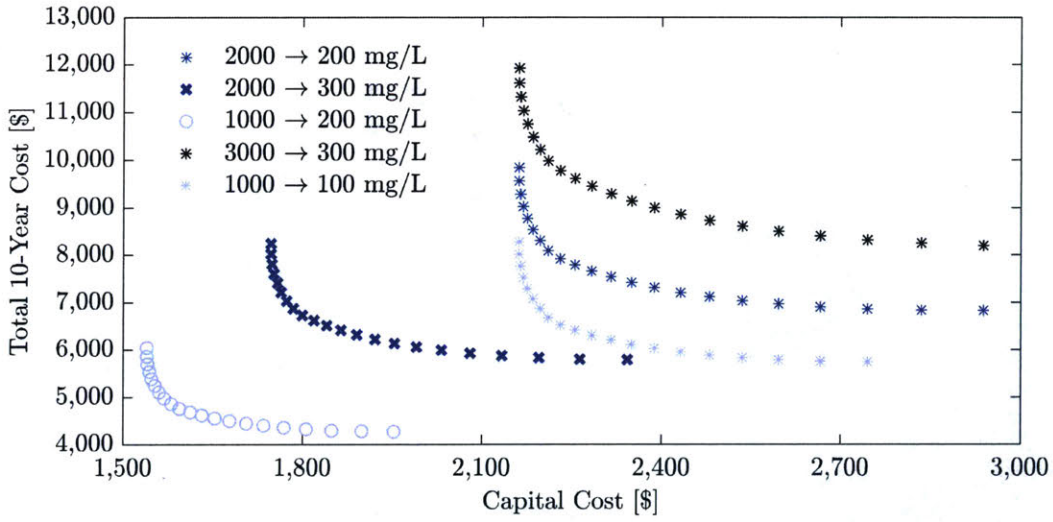

Figure 4-9: Capital cost vs. total cost Pareto front governing the ideal spiral having different feed and product water concentrations. Note that stacks designed for the same concentration ratio $CR = 10$ represented by the star markers obtain similar capital costs, regardless of the feed water salinity. Significant savings can obtained by increases the target water salinity.

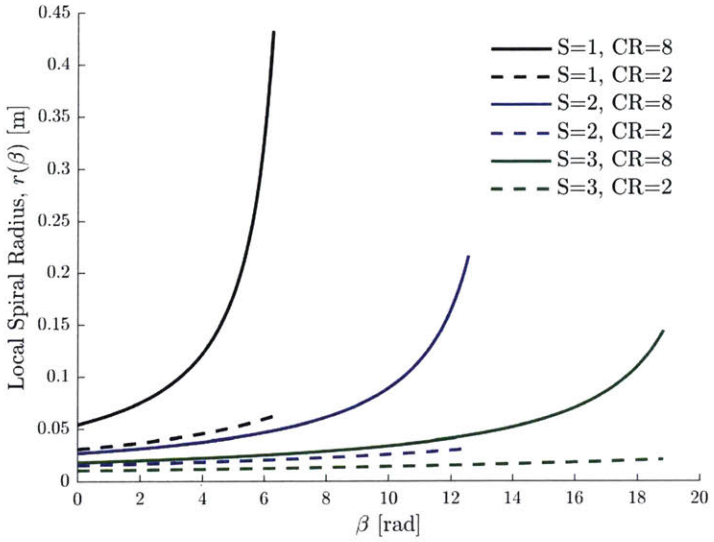

Figure 4-10: The local radius of the ideal spiral as a function of angle β for different numbers of total turns and concentration ratios.

that lower CR stacks have smaller inner and outer electrode radii (Fig. 4-10), it is prudent to look at the effect of staging ideal spiral stacks in series. For example, a single stack with a CR=8 would have the same concentration reduction as three stacks in series, each with CR=2, as long as all stacks had the same number of turns. The reduced electrode area in a staged system could make the stack easier to manufacture.

Optimization was completed for a three-stage ideal spiral system in which each stack has CR=2.15, for a total of CR=10, and compared to the previous results. When total and capital cost are equally weighted, the three stacks each have an inner radius of 5 cm, outer radius of 10.8 cm, membrane width of 24.2 cm, 34 cell pairs, and operate at 14 cm/s. A component cost comparison between this system and the previous design for a single stage ideal spiral is shown in Fig. 4-11. The total and capital cost of the system increases over the single stage system. In order

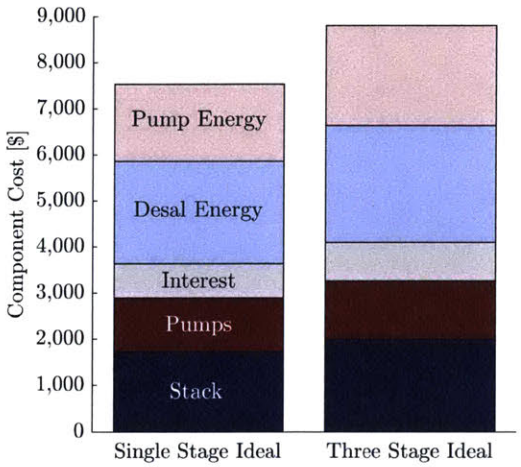

Figure 4-11: Breakdown of the total 10-year cost for a system achieving the full concentration reduction in a single ideal spiral stack (CR=10) vs over three ideal spiral stacks in series (CR=2.15 for each).

to select the lowest cost system staging, more information is needed on the cost and feasibility of manufacturing cylindrical electrodes of various sizes.

4.5 Conclusions

This chapter presents an analytical model for a spiral-wound electrodialysis (ED) module. The model improves upon existing work by accounting for channel properties (such as spacer geometry), concentration potential, and LCD. A prototype stack was built and tested experimentally. The experimental results were within 15% of modeled values for all measured parameters.

By incorporating LCD calculations along the length of the spiral, we presented a cost-optimal design for an Archimedean spiral, matching applied and limiting current densities at inner and outer electrode alone. Because the effective membrane area increases linearly with each successive turn, this standard spiral shape is unable to

maintain matching limiting and applied current densities. Another ideal spiral shape is thus described whose radius grows at the rate required for exact matching at all locations. By analyzing the Pareto optimal point that places equal weight on the importance of capital and 10-year total cost, we found that the ideal spiral reduces the total cost by 21% and capital cost by 39% with respect to an Archimedean spiral. Both designs had large outer electrode radii (49.8 cm and 75.2 cm for the Archimedean and ideal spirals, respectively), thus an initial discussion on the benefits and drawback of staging multiple smaller radii in series is presented. Both spiral shapes showed preference for minimizing the number of turns of the spiral (1.4 and 1.0, respectively).

Further work on this topic is ongoing and includes: performance comparisons between all constant voltage architectures (constant voltage batch and continuous flat stack architectures); and the design of spiral stacks that allow for re-circulation of the brine stream while running in a parallel configuration. While more information on the cost and feasibility of manufacturing spiral ED stacks is required, this analysis suggests that there is potential for a cost-effective, constant voltage, continuous process, in which the limiting and applied current densities match at all locations by the design of the stack geometry alone.

Bibliography

[1] K.H. Meyer and W. Straus. La permÃľabilitÃľ des membranes VI. Sur le passage du courant Ãľlectrique Ãă travers des membranes sÃľlectives. *HCA*, 23:795–800, 1940.

[2] T. Wen and G. S. Solt. Modeling the spirally wound electrodialysis process:

Single start, parallel flow. *Institution of Chemical Engineers Symposium Series*, 127:11–22, 1992.

[3] T. Wen, G. S. Solt, and Y.F. Sun. Modeling the cross flow spirally wound electrodialysis SpED process. *Desalination*, 103:165–176, 1995.

[4] T. Wen, G. S. Solt, and Y.F. Sun. Spirally wound electrodialysis SpED modules. *Desalination*, 101:79–91, 1995.

[5] F.N. Ponzio, A. Tamburini, A. Cipollina, G. Micale, and M. Ciofalo. Experimental and computational investigation of heat transfer in channels filled by woven spacers. *International Journal of Heat and Mass Transfer*, 104:163–177, 2017.

Chapter 5

Conclusions

In this thesis, I have proposed methods of reducing the capital and 10-year total cost of small-scale electrodialysis brackish water desalination systems, using a baseline target production rate of 1000 L/h and desalination from 2000 mg/L feed to 200 mg/L product, as motivated by the needs present in rural India. Five operating modes and stack architectures had an estimated capital cost (pumps plus ED stack) of less than $3000 (Fig. 5-1), which is approximately 50% of the capital cost limit ($5900) discussed in Chapter 1. This price point leaves room for the additional cost of other necessary components such as the rectifier, valves, piping, sensors, and control modules and is predicted to be commercially feasible.

In Chapter 2, develop a robust parametric model is developed to predict the desalination rate, limiting current density, and total energy use in an ED system, synthesizing the contributions of other authors in the field, and adding discussion on the sensitivity of changes in model parameters that are typically found experimentally. This allowed the model to be implemented and compared to experimental results at two diverse stack size scales (0.18 vs. 37.1 m^2 total membrane area), spacer

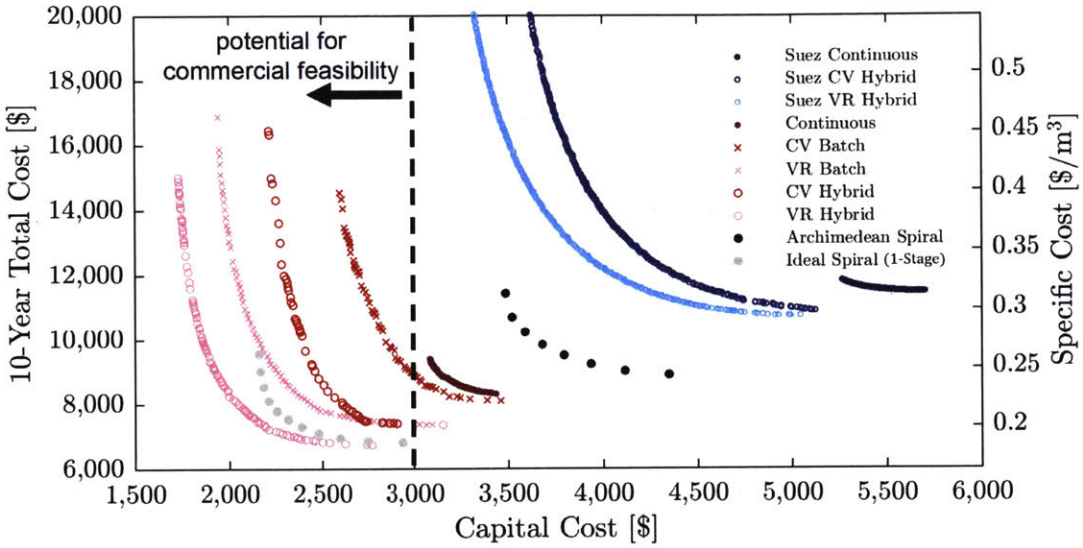

Figure 5-1: ED stacks have a flat architecture and operating under constant voltage (CV), voltage regulated (VR), batch, continuous, and hybrid modes are compared to a continuously operating Archimedean and ideal spiral design.

thicknesses (0.35 vs. 0.71 mm), spacer types (woven vs. overlapped), as well as in two diverse feed waters (NaCl vs. real brackish groundwater). To our knowledge, the theory presented in this chapter is the first robust model of ED stack behavior that does not require any new experimental parameter estimation or system characterization and that is shown to achieve reasonable accuracy when compared to experimental results. While five existing models for pressure drop in spacer filled channels were implemented, and one model for each stack was found to reasonably approximate experimental pressure drop, no one model adequately predicted the pressure drop for both spacer designs. As a result, improved pressure drop characterization is recommended as an area of future work, especially since pumping power is shown to contribute to the overall specific energy in an important way in the following chapters.

In Chapter 3, ED model is used within optimization routines to gain insight into

cost-optimal ED stack geometries and operating modes. I explore typical operating modes such as constant-voltage (CV) batch and multi-stage continuous systems as points of comparison to new operation modes including voltage-regulation (VR) and hybrid batch-continuous systems. For the production and desalination rates required for a village-scale application, a voltage-regulated hybrid system that is fully optimized for membrane width, length, and channel thickness reduces the 10-year total cost and capital cost of the system by 37% and 47%, respectively, in comparison to a commercially available stack optimized under the same operation modes. It is thus recommended that hybrid operation be considered in place of batch operation, that the cost of adding VR be analyzed and the cost model updated, and that cost and manufacturing ramifications of updating the membrane, spacer, and electrode geometries for the specific production rates required in village-scale systems be explored. In all operating modes, the optimization result tended toward the minimum allowable channel gaps and movement along the Pareto front was governed by changes in the linear flow velocity. As the channel gap and fluid velocity both affect the pressure drop over the stack and the efficiency of membrane use, the optimization results furthered the argument for future work on characterizing spacer designs.

In Chapter 4, I use what was learned from Chapter 3 about the cost-benefit of applying an instantaneous current density that matches the limiting current density at all points in the system through voltage-regulation, and attempt to gain the same benefit in a constant voltage, continuous system; I do so by suggesting a spiral membrane geometry with concentric cylindrical electrodes. I update the model developed in Chapter 2 to be applicable for this design and validate the updated model using a prototype Archimedean spiral stack. Optimization of the spiral shape, however, reveals that the ideal spiral radius would increase exponentially, not linearly (as is the case for the Archimedean spiral). Implementing such a spiral could reduce the

10-year total cost and capital cost by 21% and 39%, respectively, in comparison to the Archimedean spiral that is commonly used in RO systems and has been explored in ED. This novel spiral has the potential to be cost-competitive with a voltage-regulated flat-stack design if the same cost structure can be assumed. Therefore, a critical next step in this work is to understand the cost and manufacturing ramifications of the spiral shape in comparison to a traditional flat-stack design. While further analysis is needed, the work here suggests that there is potential for a cost-effective, constant voltage, continuous process, in which the limiting and applied current densities match at all locations.

In addition to the future work discussed in Chapters 2-4, it is also recommended that the hybridization of ED with other technologies such as NF and RO be explored for this size-scale and context. This comes as a result of the high sensitivity of both capital and operational cost to the product water concentration and increasing demand by our field partners for product water of very low salinities (less than 200 mg/L). Finally, this work revealed significant cost (capital and operational) associated with pumping for both the traditional flat-stack and spiral architectures. This is largely due to the low pump efficiency of multi-stage centrifugal pumps that operate in the investigated flow rate range. It is therefore recommended that efforts be put into the design of low-cost, high efficiency pumps that could better meet the demands of both village-scale RO and ED systems.